CHARGE INJECTION CONTACTS IN ORGANIC SEMICONDUCTOR DEVICES

DAGMAWI BELAINEH

(M.Sc., Jacobs University)

A THESIS SUBMITTED FOR THE DEGREE OF

DOCTOR OF PHILOSOPHY

DEPARTMENT OF PHYSICS

NATIONAL UNIVERSITY OF SINGAPORE

2015

For Tati and Abaye

For GHU Team, Dèng Yūn, Dīng Dúo

DECLARATION

I hereby declare that this thesis is my original work and it has been written by me in its entirety. I have duly acknowledged all the sources of information which have been used in the thesis.

This thesis has also not been submitted for any degree in any university previously.

_____

Dagmawi Belaineh
10 June 2015

Acknowledgements

The work described in this thesis was carried out in the Organic Nano Device Lab (ONDL), National University of Singapore (NUS) from August 2010 to December 2014. It was made possible by the generous research scholarship from the Government of Singapore through the Singapore International Graduate Student Award (SINGA) and research grant from ONDL.

My deepest gratitude goes to my supervisors Dr. Peter Ho, Dr. Chua Lay-Lay and my dear mentor Dr. Png Rui Qi (Rachael) for the scientific inspiration, continuous support, and extraordinary patience. It is a blessing to have had, in such close company, leaders whom I look up to, personally and professionally. May the seeds you have planted thrive, bringing forth constant rich harvest.

Many thanks to Dr. Jeremy Burroughes, Dr. Natasha Conway, Yamada san from Cambridge Display Technology Ltd./Sumitomo, Christine McGuiness and Floryan Decampo from Solvay OLED/Plextronics for the deep privilege to work on company projects of immediate industrial relevance.

I would like to thank former and current ONDL seniors Li-Hong, Loke Yuen, Jing-Mei, Zhili, Guan Hui, Guo Han, Song Jie, Hu Chen and Kendra for the smooth induction into the lab, their assistance, fruitful discussions and encouragement. My thanks also goes to Wei Ling, Kim Kian, Jun-Kai, Jin-Guo, Edwin, Meng How and all junior members for a productive and enjoyable working environment.

I would like to acknowledge the considerable input of Pei Fang and Yi Min from NUS High School in the PFI experiments (Chapter 3), Jin-Guo for SEM images and Kendra for AFM taken in the copper project (Chapter 4), Jun Kai for his Python wizardry, Venu for the synthesis of methyl peroxide in the copper project (Chapter 4), and Edwin for support in a synthesis project not discussed in this thesis.

Abstract

Organic electronics has grown tremendously over the last four decades as witnessed by the number of journals, symposiums, research groups and companies in the field. Organic semiconductor devices comprise one or more organic semiconductor layers adjacent to charge-injection and extraction contacts. It is of great importance that these contacts operate with high efficiency and stability. This thesis focuses on developing new understanding to achieve better charge injection contacts, primarily for holes, which are relevant to organic semiconductor devices such as diodes and field-effect transistors. The two main types of charge-injection contacts are: (i) between a *p*-doped conducting polymer-based hole-injection layer (HIL) and the semiconductor, and (ii) between a metal or a doped inorganic semiconducting oxide and the semiconductor. In Chapters 2 and 3, I studied the properties of a new highly-stable *p*-doped conducting polymer blend, poly(3-methoxyethoxyethoxythiophene): poly(4-hydroxystyrene) (S-P3MEET:PHOST) and new p-doped conducting polymer blends formulated with Nafion® oligomers, also known as perfluorinated ionomers (PFIs), and their use as HILs. Using ultraviolet photoelectron spectroscopy (UPS), X-ray photoelectron spectroscopy (XPS), Raman spectroscopy, and device studies, I demonstrated and explained the unusual resilience of S-P3MEET:PHOST to the injection-induced dedoping which leads to conductivity fading in poly(3,4-ethylenedioxythiophene): poly(styrenesulfonic acid) (PEDT:PSSH). I also demonstrated that while surface-segregation of PFI can increase workfunction in the blends, using PEDT: PSSH: PFI as model, this does not always benefit hole injection because of the resistance associated with the molecularly-thin PFI

overlayer. In Chapter 4, I studied the systematic "tuning" of the workfunction of air stable Cu metal and its influence on hole/ electron injection into suitable organic semiconductors. Using XPS, UPS, and atomic force microscopy and scanning electron microscopy as primary characterization tools, new solution-processing methods were developed to obtain extreme workfunctions on this surface while limiting its surface roughness. Greatly improved electron and hole injections were obtained into the appropriate semiconductors compared to "clean" copper electrodes.

In Chapter 1, we provide a general introduction to organic semiconductors and organic semiconductor devices relevant to this thesis.

In Chapter 2, we demonstrate the superior electrical stability of S-P3MEET:PHOST (XA3551, Plextronics®) compared to PEDT:PSSH and identify the cause of this improved stability. We show that this arises from (i) improved electrochemical stability, and (ii) ultralow ionic conductivity of the PHOST matrix, which inhibits the solid-state electrochemical reaction needed to generate doping level shift in devices. Further, a solid-state esterification reaction between the PHOST and the S-P3MEET which further depletes excess mobile protons, was identified.

In Chapter 3, we demonstrate using PEDT: PSSH: PFI blends that high workfunction alone is not a sufficient criterion for ohmic contacts to organic semiconductors - the contact must also not be resistive. A joint XPS and UPS study reveals that these blends achieve high workfunctions (up to 5.6 eV) due to surface segregation of a molecularly-thin polar PFI overlayer. However despite the highly favourable workfunction, this HIL is not capable of injecting holes into organic semiconductors with deep ionization potentials much better than HILs without the PFI modification. The absence of modulation of the δ-hole charge carrier density at the semiconductor interface measured by electroabsorption spectroscopy reveals that hole injection is inherently slow at these contacts.

In Chapter 4, we describe the development of a solution process to generate high-workfunction Cu surfaces (5.4 eV) by oxidation of the surface to the Cu(II) states without causing surface roughening by hydrous Cu(II) oxides, and low-workfunction Cu surfaces (3.7 eV) by treating the native Cu(I) oxide surface with a thiocarbamate. Greatly improved hole (electron) injection into model organic semiconductors from the high (low)-workfunction Cu surface compared to native Cu surface was observed.

Table of Contents

List of Figures

Chapter 1. Introduction

Since the discovery of conductivity in organic materials in 1977,[1] the field of organic electronics has undergone remarkable progress. Shirakawa, McDarmid, and Heeger in their pioneering investigation, doped polyacetylene with iodine to make the first known conducting organic polymer.[1,2] This discovery, boosted by the introduction of organic semiconductors, spurred the first demonstration of heterojunction organic photovoltaic devices by CW Tang in 1986,[3] the first organic field-effect transistors by Tsumura et al in 1986,[4] and of organic light emitting diodes by Tang et al in 1987.[5] The major impulse to organic polymer electronics was given with the discovery of the light-emitting properties of poly-phenylene-vinylene at the Cavendish Laboratory by Burroughes et al.[6] Currently, the field of organic electronics is making fast advances at all fronts and state-of-the-art devices have already reached the market with notable success.[7] Attributes such as flexibility, light-weight, roll-to-roll production, cheap fabrication, which are not accessible to the inorganic semiconductor industry, are what make organic electronics highly attractive.[8]

1.1 Organic Semiconductors

The field of organic electronics is tied to the design, study and use of organic conductors and semiconductors. Their electrical properties stem from their π-conjugated, loosely bound electrons. The carbon atoms in conjugated molecules are found in the sp^2 hybridized state (see Fig 1.1). In such states the s orbital and the two p-orbitals (p_x and p_y) form three hybridized orbitals while the p_z orbital remains unaffected. The sp^2 orbitals are found in a single plane and the p_z is in a space perpendicular to the plane formed by the sp^2 orbitals. Two sp^2 hybridized carbon atoms form one sigma bond with one other through the sp^2 orbitals and one π bond through the p_z orbital. The

bonding and antibonding (π and π*) levels of the π-bond have small energy difference which makes conjugated polymers a semiconductor. With increasing number of bonded sp^2 hybridized carbon atoms with alternating single and double carbon-carbon the bonding π orbitals form the highest occupied molecular orbital (HOMO) and the antibonding π* orbitals form the lowest unoccupied molecular orbital (LUMO). The energy difference between the HOMO and the LUMO, known as the energy gap E_g is typically 1.5 eV > E_g > 5.0 eV. Hence conjugated organic materials are semiconductors. Figure 1.1 describes how the bonding and anti-bonding orbitals of a molecule develop into the HOMO and LUMO in a polymer or crystal, through an overlap of the p_z-orbitals. The level of overlap depends on the structure of the molecule and it determines its bandgap. Subsequently, the optoelectronic properties of the molecule are strongly linked to its structural order, which is true for conjugated polymers as well.

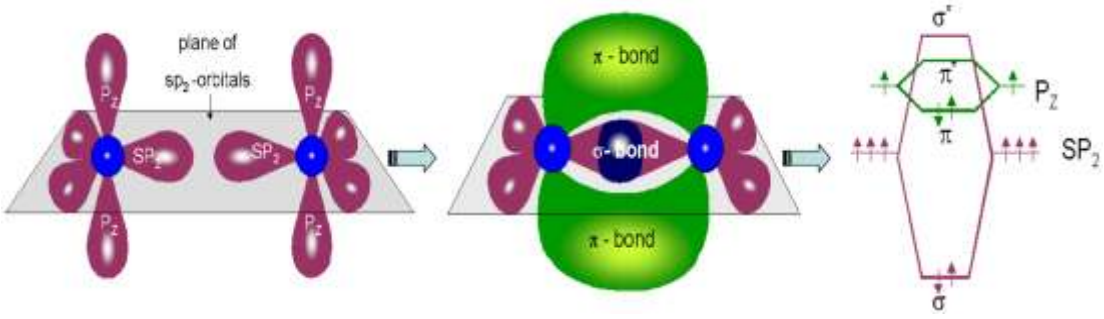

Figure 1.1. sp^2 hybridization leading to π-conjugation in ethane.[9]

Organic semiconductors are divided into small molecule and polymeric organic semiconductors. Figure 1.2 shows a few of the commonly used organic semiconductors. Apart from their molecular size, processing conditions and their film properties make these two groups of materials different. Small-molecule organic semiconductors generally require high-vacuum processing conditions and are often sublimated requiring a high deposition temperature. On the other hand, polymeric

semiconductors are processed from solution by techniques such as spin coating, drop-casting, ink-jet printing.[10] The level of order i.e. crystallinity achieved by small molecules is superior to their polymeric counterparts and hence small-molecules are often used for studying the fundamental behavior of organic semiconductors.[11] Small organic molecules in a solid are held by van der Waals forces and it is possible to prepare highly ordered crystals by vacuum sublimation of impurity-free materials. These highly ordered crystals form electronic bands similar to inorganic semiconductors. On the other hand, polymeric organic semiconductors make more disordered solids. Due to their simpler processibility, conjugated polymers are the ideal candidates for large area, flexible, and cheap devices.[12]

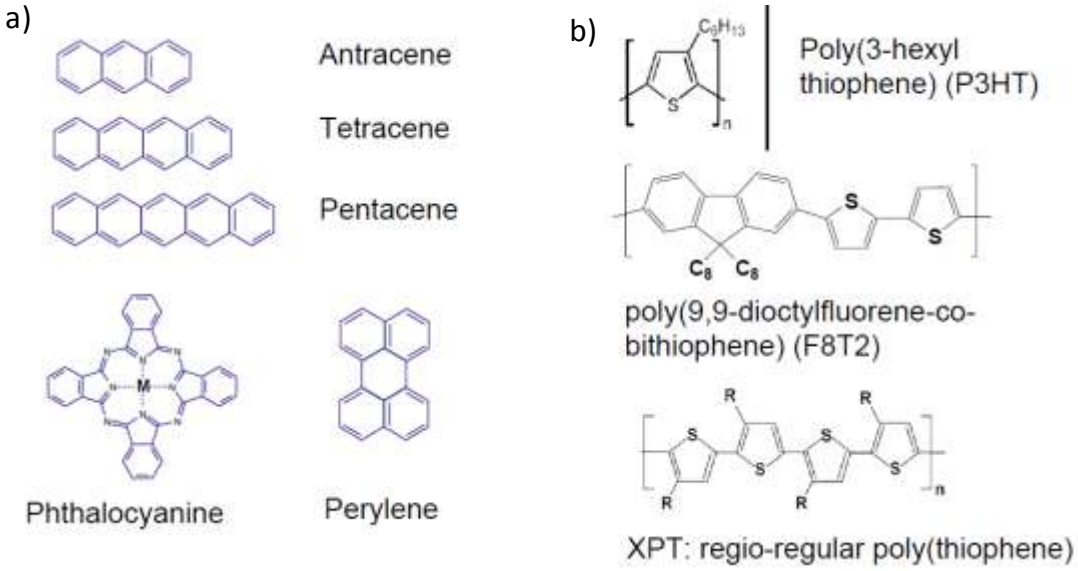

Figure 1.2. Commonly used pi-conjugated **a)** small molecules and **b)** polymers.[9]

1.2 Organic Conducting Polymers

Organic conjugated polymers are typically semiconductors in their intrinsic form. It was the doping of polyacetylene by iodine which opened the door to the world of conducting polymers. It is also possible to dope polyacetylene in solution via charge transfer or by electrochemical redox reaction.[13] Both p-type and n-type doping have been demonstrated. For p-type (n-type) doping, a molecule with high (low) electron affinity is used as an acceptor (donor). The overall charge neutrality is maintained by a counter-ion which is not involved in charge transfer processes. For example, nitrosonium hexafluoro phosphate is commonly used in solution as a p-type dopant, with the doping steps shown in the following equation.

$$(NO^{+}PF_{6}^{-}) + [CH]_{n} \rightarrow \frac{1}{2}N_{2}O_{2}(gas) + [(CH)^{+}(PF_{6}^{-})]_{n}$$

The incorporation of an additional charge will cause a local structural and energetic change of the polymer chain due to a strong interaction between the charge and the polymeric lattice. At low doping concentrations the self trapped charge/s form the bound charge quasiparticles known as polarons, and at moderate doping levels bipolarons.[14] Upon higher doping, bands at the Fermi energy, similar to metals are observed, with several orders of magnitude increase in the conductivity.

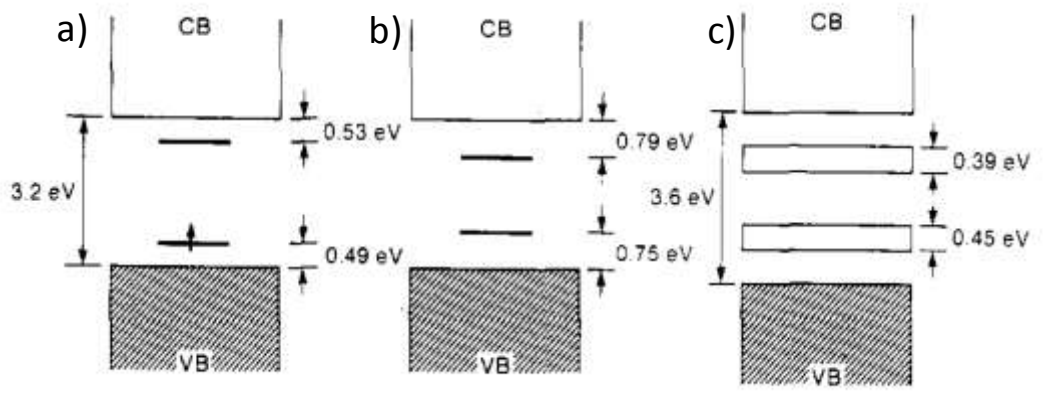

Figure 1.3. Evolution of the conjugated polymer polypyrrole upon doping from **a)** polaron **b)** bipolaron **c)** band formation.[14]

Figure 1.3 shows that polarons and bipolarons have energy states in the 'forbidden' gap between the conduction band and the valence band of the polymer and the formation of a band upon higher doping for polypyrrole.

1.3 Hole Injection Layers (HILs)

HILs are conducting materials that are used as interlayers between two device layers to facilitate the injection of holes by providing better energy alignment.[15] In organic electronics, HILs are most often put between a transparent ITO electrode with a relatively high workfunction and an organic semiconductor polymer with an even deeper ionization potential (I_P) bridging the energy gap between the Fermi energy (E_F) of the metal and the highest occupied molecular orbital (HOMO).[16] Since the main purpose of HILs is to serve as a transport layer without direct functional use, they are kept as thin interlayers ~ 50 nm. Making these layers as thin as possible is also important so as

to avoid loss in device functionality due to, for example, series resistance and drop in transparency. The two commonly used HILs are conducting polymers and transition metal oxides (TMOs).

Conducting polymers have been effectively used as interlayers for better band alignment between the anode and the organic functional layer.[16] PEDT:PSSH is the most commonly used HIL due to its high transparency, high conductivity and easy processibility.[17] In addition, its workfunction can be tailored for better energy alignment by substituting the counterion of the PSS with different ions.[18] However, PEDT:PSSH is intrinsically acidic, which can lead to etching of the anode metal.[19] Furthermore, it is found to be unstable under UV exposure,[16] and high current injection which lead to a solid state permanent dedoping of the PEDT, rendering it insulating.[20] Alternative polymer HIL based on polyaniline have also been proposed but they don't lead to more efficient devices and operate at higher voltages.[16,21] Recently, a conducting polymer S-P3MEET:PHOST has been developed which shows remarkable electrical stability compared to PEDT:PSSH.[22,23] The enhanced electrical stability of S-P3MEET:PHOST results from its inherent ultralow ionic conductivity, further suppressed by a serendipitous scavenging of excess sulfonic acid protons on S-P3MEET through a solid-state esterification reaction with PHOST during annealing. This mechanism if further elucidated in Chapter 2 of this thesis.

TMOs form the other group of most often used HILs.[24,25] The most common are MoO_3, WO_3, and V_2O_5. Often these oxides are given as MoOx, WOx, and VOx because the stoichiometric ratios are not exact under normal preparation conditions. In fact, pure MoO_3, WO_3, and V_2O_5 have been shown to be insulators.[25] It was previously believed that these oxides are p-type semiconductors, but it has been established that they are n-type semiconductors with high electron affinity (> 6.5 eV).[26,27] The n-type behaviour is attributed to oxygen deficiency in the oxide lattice. TMOs have

high transparency and provide good energy alignment with deep I_P organic polymers. However, they have low conductivity (~ 10^{-7} S/cm for 100 nm of MoO_3) which is the reason they can not be used as independent electrodes. For comparison, indium-tin-oxide, which is a commonly used anode in OLEDs and OPVs, has a conductivity of ~ 10^4 S/cm for 100 nm thick layer.[25] The limitations in the use of TMOs are their scarcity, cost of fabrication (TMOs are most often vacuum deposited at high temperatures ~400 ^{0}C), and air sensitivity. However there has been recent progress in solution-processed TMOs with efficiencies and stabilities comparable or higher than control PEDT:PSSH devices.[28]

1.4 Organic Semiconductor Devices

1.4.1 Organic-field-effect-transistors (OFETs)

OFETs, similar to their counterparts from inorganics, are composed of a source, drain, and gate electrode. The active semiconductor, which can be a small molecule or polymeric organic material, is separated from the gate electrode by a thin layer of dielectric. A bias applied on the gate electrode induces an accumulation of charges on the dielectric/semiconductor interface (see Fig 1.4). The accumulated charges can be driven across the source drain connection by applying a bias across these two electrodes. It should be noted that, contrary to OFETs, inorganic FETs work by inversion of charge carriers i.e. charge transport by minority carriers.[29]

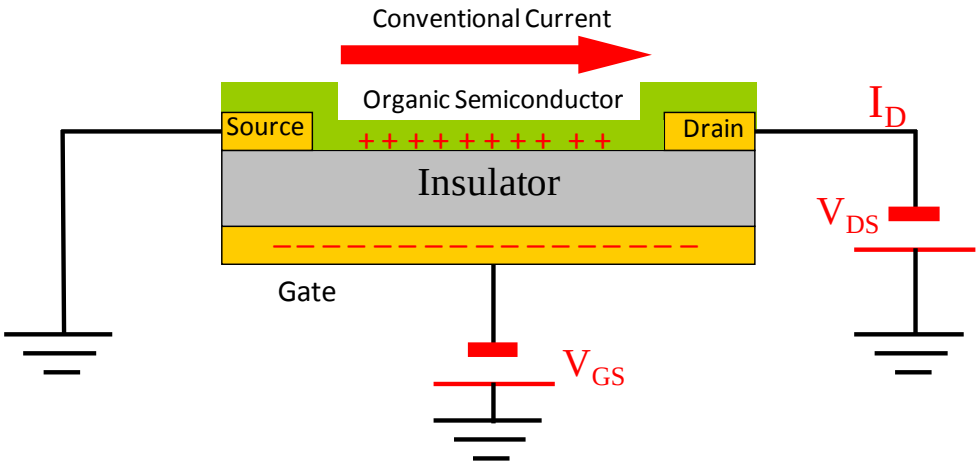

Figure 1.4. Common structure and working principles of a bottom-gate-bottom-contact organic field-effect transistor

Figure 1.4 shows a simplified bottom-gate-bottom-contact organic field-effect transistor. Here, a doped silicon serves as the gate electrode and the dielectric is a thermal silicon oxide of several hundred nanometers thickness. The type of source/drain contact deposited on top of the dielectric depends on the nature (n-type, p-type) of the organic semiconductor used on top. Apart from the alignment of the workfunction of the metal with the HOMO (LUMO) of the p-type (n-type) semiconductor, the electrode metal has to be chemically and mechanically stable under processing as well as performance conditions. Gold is the preferred electrode with p-type semiconductors because of its high workfunction and high stability. The low adhesivity of gold to surfaces is overcome by depositing a thin layer of chromium or titanium underlayer. However, gold is very expensive and is not the ideal choice for large area, mass produced electronics. In addition, gold does not provide good injection into deep HOMO polymers resulting in high contact resistance. Contact resistance becomes an increasing cause of loss of efficiency with device miniaturization because the area of contacts remains the same while other parameters decrease in area. Especially, with the emergence of high performance organic semiconducting materials, the role of

contacts becomes more and more critical. Metals such as silver are plagued by energy alignment and stability issues. Introduction of PEDT:PSSH or other buffer layers,[30-32] and contact dopants[33] have been investigated. However, a simple and robust method of minimizing contact resistance is still being searched for.

Following the fabrication of the first polymeric OFET in 1987 using polythiophene,[34] their performance and stability has undergone remarkable progress.[35,36] Small molecule OFETs have been used to study morphology, charge transport, and the role of molecular packing in devices.[35] Charge carrier mobilities in the range of 10 $cm^2V^{-1}s^{-1}$ and on off-ratios in the range of 10^9 have been achieved.[37] Although the majority of OFETs reported make use of p-type organic semiconductors due to their higher stability,[38] OFETs working with n-type materials have been reported as well,[39] opening ways for a completely organic logic systems to be built. Polymeric OFETs are also highly researched due to their faster and cheaper processibility. The level of molecular ordering is limited in polymer OFETs compared to small molecule OFETs, but mobilities in the range of 1 $cm^2V^{-1}s^{-1}$ have been reported.[38]

Miniaturization of devices in the electronic industry demands for smaller and smaller components that make up the devices. OFETs with channel length of a few tens of nanometers have been achieved by electron beam lithography. Theoretically, the maximum switching frequency and the current output of transistors scale as L^{-2} and L^{-1}, respectively, where L is the channel length.[8] However, the predicted device improvements are not achieved due to the dominance of contact resistance for short channel length transistors.

The energetics at the interface between an electrode and the organic semiconductor can lead to charge injection barriers which are quantified as contact resistance. The resistance in the individual electrode and organic semiconductor is known as sheet resistance which is independent of the contacts. Miniaturization via a decrease in the channel length will decrease the sheet resistance but the contacts remain the same, hence for smaller devices contact resistance is a significant determinant of device performance.

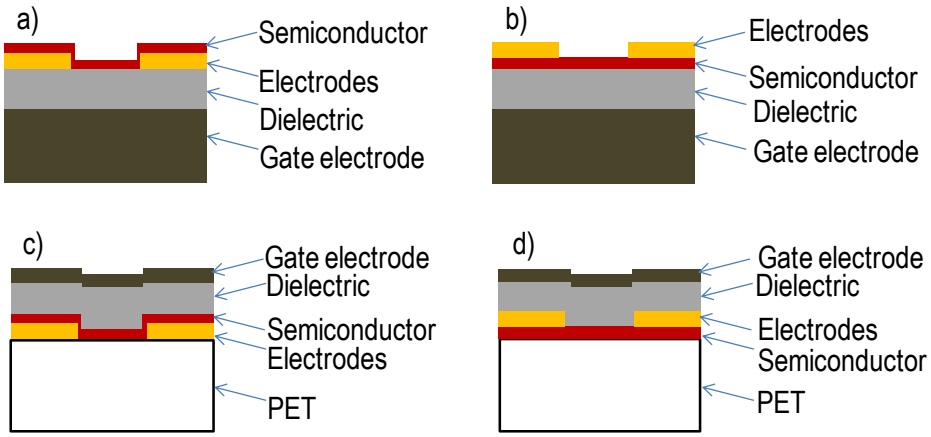

Figure 1.5. OFET configurations a) Bottom-gate-bottom-contact b) Bottom-gate-top-contact c) Top-gate-bottom-contact and d) Top-gate-top-contact

An OFET can be of any of the following four configurations: a) Bottom-gate-bottom-contact b) Bottom-gate-top-contact c) Top-gate-top-contact and d) Top-gate-bottom-contact as shown in Figure 1.5. Each configuration provides different processing and characterization possibilities. The bottom-gate devices often have a SiO_2 dielectric and a n- or p-type Si gate. Top-gate devices, on the other hand, have glass or plastic support at the bottom and use a spin-coated dielectric. Bottom-gate-bottom-contact and top-gate-bottom-contact devices have been fabricated in the

course of this work. The source and drain electrodes are lithographically patterned in order to produce miniaturized devices.

The two direct electrical measurements done on an OFET are the output and the transfer characterizations. An output curve shows the dependence of the source current I_S on the drain-source voltage V_{DS} for a constant gate voltage. A transfer curve shows the dependence of source current I_S on gate voltage V_{GS} for a constant V_{DS}. Parameters, such as charge carrier mobility, threshold voltage, and contact resistance can be extracted from these curves using equations of the gradual channel approximation.[40,41] The gradual channel approximation uses a linear potential profile across the source-drain contacts to describe charge transport. The approximation describes two regimes of transistor operation: linear or saturated regimes. In the linear regime the gate voltage is much larger than the drain-source voltage, $V_{DS} << V_{GS} – V_T$, leading to a uniform charge distribution at the organic semiconductor/ dielectric interface. The drain-source current is described by the following equation for such cases:

$$I_D \approx \frac{W}{L} C_i \mu (V_{GS} - V_T) V_{DS}$$

Where C_i is the capacitance of the dielectric and μ is the voltage-dependent charge carrier mobility.

With increasing drain-source voltage, charges are depleted faster from the semiconductor. The drain-source current shows a quadratic dependence on V_{GS} in the regime $V_{DS} >> V_{GS} – V_T$, which is referred to as the saturation regime.

$$I_D \approx \frac{W}{2L} C_i \mu (V_{GS} - V_T)^2 V_{DS}$$

1.4.2 Organic polymeric light emitting diodes (PLEDs) and lightings

Beginning with seminal work by Burroughes et al in the late 1980s[6] which resulted in the first light emitting polymeric device, PLEDs have undergone constant progress in terms of stability as well as longevity. The first PLED was made up of a very simple three layer structure, composed of an ITO anode, a light emitting poly(p-phenylene vinylene) (PPV), and an aluminium cathode. The possibility to produce flexible, cheap, large-area, light-weight, bright PLEDs with simple methods such as spin-coating, ink-jet printing makes them very appealing to the industry which seeks to make displays and lighting from PLEDs. Current PLEDs have higher sophistication for better charge transport and light outcoupling, with HILs, electron transport layers, dopants, interlayers, nanoparticles, microprisms, corrugations being added into the device geometry.[42-46]

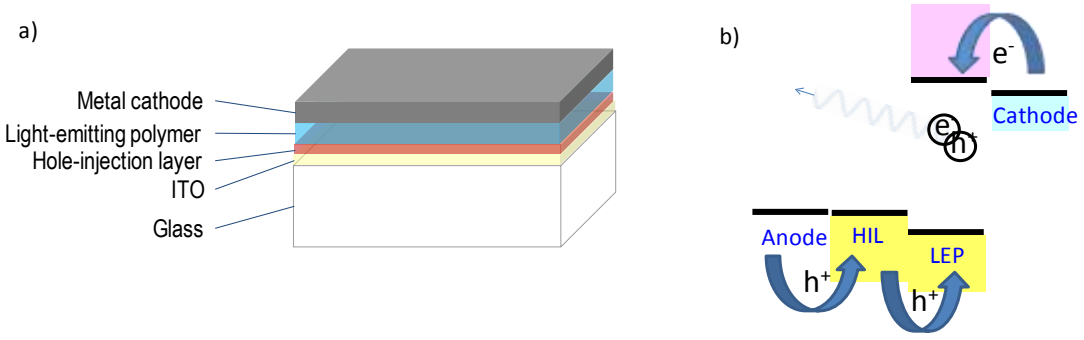

Figure 1.6. a) Simple structure of a light-emitting diode, b) light generation in a light emitting device.

Figure 1.6 shows a general structure of a state-of-the-art PLED. The requirement that one of the electrodes be transparent has made ITO the most commonly used anode. The relatively low workfunction of ITO (~4.8 eV), however, limits its efficiency as charge injector in deep IP polymers. This is often overcome by putting a thin layer of the HIL PEDT:PSSH which has a higher workfunction of ~ 5.1-5.2 eV. PEDT:PSSH makes a less rough surface than ITO and leads to

Fermi level pinning with the HOMO of the semiconductor.[47] The light emitting polymer is deposited on to the ITO via simple processing steps, such as spin coating, and annealed so as to get rid of excess solvent. The wavelength of light emitted by the polymer is determined by its π-π* gap. A combination of polymers, emitting primary colour lights, can be used for white light emission. The cathode of a PLED is a low workfunction material, often from the Group IIA of the periodic table, such as calcium or barium. Due to the high reactivity of this group of elements a layer of aluminium is deposited on top as encapsulation. A PLED operates by applying a positive bias on the anode and a negative bias on the cathode. Holes are injected from the anode into the HOMO of the polymer while electrons are injected into its LUMO. When a hole and electron are spatially bound, forming what is known as an exciton, they can undergo radiative relaxation, releasing a photon with an energy equal to the π-π* gap.

Currently, the demand for efficient blue emitting light sources and stable light emitting polymers which have deeper ionization potential is driving the search for higher workfunction electrodes, even higher than the workfunction of the ubiquitous PEDT:PSSH. The incorporation of a perfluoro ionomer (PFI) into PEDT:PSSH has been investigated to increase the workfunction of the HIL.[48,49] PEDT:PSSH blended with PFI has been reported to give high work function of up to 5.8 eV.[48,49] It has been also been reported that layer by layer deposition of PEDT:PSSH and PFI gives higher workfunctions, which were used to produce more efficient organic light emitting diodes.[50] The higher workfunctions in PFI containing films were attributed to the preferential aggregation of PFI on the top of the HIL, which creates a strong dipole.[49] However, the improvement in device performance is small. Despite the increase in the workfunction, PFI forms an insulting layer at the interface, thereby countering its positive effects. There have also been attempts to overcome

energy level mismatch between the electrode and the light emitting polymer by using cascade injection in which holes are first injected into a triarylamine polymer with a suitable *I*p between the workfunction of the PEDT:PSSH and the *I*p of the desired LEP.[51,52] Tuning of electrode workfunction has also been demonstrated by stacking bi-metal layers,[53] depositing oxide layers,[54] and using self assembled monolayers (SAMs) of small molecules.[55-57] However, there is still a need for simple and robust processing methods which provide high workfunction electrodes.

1.4.3 Organic photovoltaics (OPVs)

OPV research has gone a long way from the first demonstrations of 1% efficiency solar cell by Tang et al in 1986.[3] The possibility of 10% efficiency was predicted in 2006 by Scharber et al[58] and now even this value has been surpassed with efficiencies of 19% from champion devices having been reported for solar cells utilizing perovskite absorbers.[59] The rising success of organic solar cells is closely tied to the progress in materials research which allows efficient charge injection and transport.

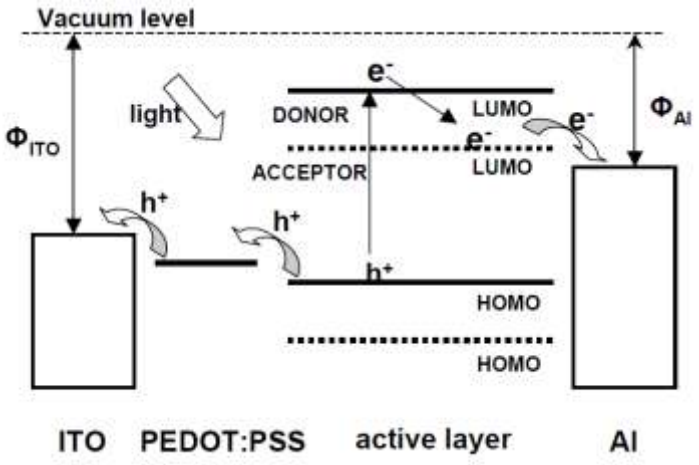

Figure 1.7. Carrier generation and diffusion in an organic photovoltaic upon exposure to light.[9]

Figure 1.7 shows the working principles of a bulk heterojunction OPV. It is composed of a light sensitive bulk semiconductor sandwiched between electron and hole extraction electrodes. The bulk semiconductor is a mix of an electron donor and an electron acceptor. Regioregular poly(3-hexylthiophene) : phenyl-C61-butyrate methyl ester (P3HT:PCBM) is one of the most investigated bulk heterojunction materials where P3HT is a p-type donor polymer and PCBM is an n-type acceptor. Incident light induces exciton (coulombically bound electron-hole pair) generation in the bulk by exciting an electron from the HOMO to the LUMO level. When the exciton reaches the interface by diffusion, it dissociates where the electron jumps from the LUMO of the donor onto the LUMO of the acceptor or the hole jumps from the HOMO of the acceptor onto the HOMO of the donor. The dissociation only happens if the coulombic energy can be overcome by the energy offset between the LUMOs or HOMOs.

Similar to OLEDS, for better energy level alignment between the active polymers and the electrodes, hole transport and electron transport layers are inserted as interlayers between the electrodes and the polymers. PEDT:PSSH is a commonly used hole extraction layer . The recently developed S-P3MEET has also been used as an efficient extraction layer.[60] Recently, perovskite-based solar cells have taken the spotlight for their unprecedented device efficiencies.[59] One of the biggest advances in perovskite solar cells came about upon the introduction of full solid-state hole transport layers composed of $CsSnI_3$ instead of the former liquid electrolytes used in dye-sensitized Graetzel cells.[32] The solid state hole transport layer put together with the dye N179 and the nanoporous electron transport layer TiO_2 dramatically improved the stability and efficiency of the cells. The absence of the liquid electrolyte got rid of leakage and corrosion issues. Furthermore, the $CsSnI_3$ is solvent processible which allowed simple processing, and importantly, the interpenetration into the nano pores of the TiO_2 making a close high surface-area contact with the

light sensitive dye. Along with good energy alignment, structural and processiblity considerations are critical for stable and efficient OPVs.

1.5 The Objective and Outline of this Thesis

As can be seen from the above introduction, the significance of efficient charge transport at interfaces to organic electronic devices is immense. In this thesis, we investigate solid-state polymeric and metallic materials for hole transport and report their successful incorporation in organic devices.

In Chapter 2, the superior electrical stability of a recent HIL, S-P3MEET:PHOST, is demonstrated. We report the successful suppression of conductivity fading under electrical bias in the HIL, achieved through the ultralow ionic conductivity of PHOST. The ultralow ionic conductivity inhibits a solid-state electrochemical reaction which leads to a doping level shift in other HILs such as PEDT:PSSH. Further, a solid-state esterification between the PHOST and the S-P3MEET depletes excess mobile protons, imparting increased stability to the S-P3MEET:PHOST blend.

In Chapter 3, we demonstrate carrier injection limitation in perfluorinated ionomer (PFI) infiltrated HILs . Despite the higher workfunction attained by blending PFI with PEDT:PSSH, the blended film is not capable of injecting into deep HOMO light-emitting-polymers more efficiently than the pure PEDT:PSSH film, which is accounted to self aggregation of PFI at the surface. The absence of δ-hole charge carrier at the OSC interface as measured by electroabsorption spectroscopy demonstrates that surface aggregation of PFI leads to a non-ohmic injection.

In Chapter 4, we present a simple and robust chemical process to generate low-workfunction (≤ 4.0 eV) and high-workfunction (≥ 5.2 eV) Cu surfaces for use in organic electronics. We utilize self assembly of thiocarbamate molecules on Cu/Cu_2O to make Cu surfaces with workfunction of 3.7 eV as confirmed by ultraviolet photoelectron spectroscopy studies. On the other hand, pH or solvent controlled oxidation in hydrogen peroxide was used to prepare smooth Cu surfaces with workfunction as high as 5.4 eV. Efficient electron and hole injection is demonstrated from the low-workfunction and high-workfunction copper surfaces, respectively. Finally, possible ways of overcoming performance instabilities in devices are proposed.

1.6 References

1 Shirakawa, H., Louis, E. J., MacDiarmid, A. G., Chiang, C. K. & Heeger, A. J. Synthesis of electrically conducting organic polymers: halogen derivatives of polyacetylene,(CH) x. *J. Chem. Soc., Chem. Commun.* **16**, 578-580 (1977).

2 Chiang, C. K. *et al.* Electrical conductivity in doped polyacetylene. *Phys. Rev. Lett.* **39**, 1098 (1977).

3 Tang, C. W. Two-layer organic photovoltaic cell. *Appl. Phys. Lett.* **48**, 183-185 (1986).

4 Tsumura, A., Koezuka, H. & Ando, T. Macromolecular electronic device: Field-effect transistor with a polythiophene thin film. *Appl. Phys. Lett.* **49**, 1210-1212 (1986).

5 Tang, C. & VanSlyke, S. Organic electroluminescent diodes. *Appl. Phys. Lett.* **51**, 913-915 (1987).

6 Burroughes, J. *et al.* Light-emitting diodes based on conjugated polymers. *Nature* **347**, 539-541 (1990).

7 Cantatore, E. *Applications of organic and printed electronics*. (Springer, 2013).

8 Klauk, H. *Organic electronics: materials, manufacturing, and applications*. (John Wiley & Sons, 2006).

9 Knipp, D., Benor, A. *Organic electronics and photovoltaics - Course Number 420442* (Jacobs University Bremen, 2008).

10 Ling, M. M. & Bao, Z. Thin film deposition, patterning, and printing in organic thin film transistors. *Chem. Mater.* **16**, 4824-4840 (2004).

11 Karl, N. *et al.* Fast electronic transport in organic molecular solids? *J Vac. Sci.Technol.* **17**, 2318-2328 (1999).

12 Facchetti, A. Π-conjugated polymers for organic electronics and photovoltaic cell applications†. *Chem. Mater.* **23**, 733-758 (2010).

13 Heeger, A. J., Kivelson, S., Schrieffer, J. & Su, W.-P. Solitons in conducting polymers. *Rev. Mod. Phys.* **60**, 781 (1988).

14 Bredas, J. L. & Street, G. B. Polarons, bipolarons, and solitons in conducting polymers. *Acc. Chem. Res.* **18**, 309-315 (1985).

15 Ishii, H. *et al.* Energy level alignment and band bending at model interfaces of organic electroluminescent devices. *J. Lumin.* **87**, 61-65 (2000).

16 Tengstedt, C. *et al.* Study and comparison of conducting polymer hole injection layers in light emitting devices. *Org. Electron.* **6**, 21-33 (2005).

17 Groenendaal, L., Jonas, F., Freitag, D., Pielartzik, H. & Reynolds, J. R. Poly (3, 4-ethylenedioxythiophene) and its derivatives: past, present, and future. *Adv. Mater.* **12**, 481-494 (2000).

18 Chia, P.-J. *et al.* Direct evidence for the role of the Madelung potential in determining the work function of doped organic semiconductors. *Phys. Rev. Lett.* **102**, 096602 (2009).

19 De Jong, M., Van Ijzendoorn, L. & De Voigt, M. Stability of the interface between indium-tin-oxide and poly (3, 4-ethylenedioxythiophene)/poly (styrenesulfonate) in polymer light-emitting diodes. *Appl. Phys. Lett.* **77**, 2255-2257 (2000).

20 Chia, P. J. *et al.* Injection-induced de-doping in a conducting polymer during device operation: asymmetry in the hole iInjection and extraction rates. *Adv. Mater.* **19**, 4202-4207 (2007).

21 Higgins, R., Zaidi, N. & Monkman, A. Emeraldine base polyaniline as an alternative to poly (3, 4-ethylenedioxythiophene) as a hole-transporting layer. *Adv. Funct. Mater.* **11**, 407-412 (2001).

22 Brown, C. T., Seshadri, V., Mathai, M., Woodworth, B. & Laird, D. 32.1: Invited paper: Plexcore® OC for HIL applications in OLED lighting and display. *SID Symp. Digest Tech. Pap.* **41**, 461-464 (2010).

23 Belaineh, D. *et al.* A high-performance p-doped conducting polymer blend based on sulfonated polyalkoxythiophene and poly (4-hydroxystyrene). *Chem. Mater.* **26**, 4724-4730 (2014).

24 Tokito, S., Noda, K. & Taga, Y. Metal oxides as a hole-injecting layer for an organic electroluminescent device. *J. Phys. D: Appl. Phys.* **29**, 2750 (1996).

25 Meyer, J. *et al.* Transition metal oxides for organic electronics: energetics, device physics and applications. *Adv. Mater.* **24**, 5408-5427 (2012).

26 Kröger, M. *et al.* Role of the deep-lying electronic states of MoO3 in the enhancement of hole-injection in organic thin films. *Appl. Phys. Lett.* **95**, 123301 (2009).

27 Kanai, K. *et al.* Electronic structure of anode interface with molybdenum oxide buffer layer. *Org. Electron.* **11**, 188-194 (2010).

28 Choi, H. *et al.* Solution processed WO3 layer for the replacement of PEDOT: PSS layer in organic photovoltaic cells. *Org. Electron.* **13**, 959-968 (2012).

29 Sze, S. & Ng Kwok, K. *Physics of semiconductor devices 3rd Edition*. (Wiley Online Library, 2007).

30 Hong, K. *et al.* Reducing the contact resistance in organic thin-film transistors by introducing a PEDOT: PSS hole-injection layer. *Org. Electron.* **9**, 864-868 (2008).

31 Li, Y.-C. *et al.* Performance improvement in transparent organic thin-film transistors with indium tin oxide/fullerene source/drain contact. *Appl. Phys. Lett.* **95**, 163303-163303-163303 (2009).

32 Chen, F.-C., Kung, L.-J., Chen, T.-H. & Lin, Y.-S. Copper phthalocyanine buffer layer to enhance the charge injection in organic thin-film transistors. *Appl. Phys. Lett.* **90**, 073504 (2007).

33 Minari, T. *et al.* Highly enhanced charge injection in thienoacene-based organic field-effect transistors with chemically doped contact. *Appl. Phys. Lett.* **100**, 093303 (2012).

34 Koezuka, H., Tsumura, A. & Ando, T. Field-effect transistor with polythiophene thin film. *Synt. Met.* **18**, 699-704 (1987).

35 Sirringhaus, H. 25th anniversary article: organic field-effect transistors: the path beyond amorphous silicon. *Adv. Mater.* **26**, 1319-1335 (2014).

36 Zhao, Y., Guo, Y. & Liu, Y. 25th anniversary article: recent advances in n-type and ambipolar organic field-effect transistors. *Adv. Mater.* **25**, 5372-5391 (2013).

37 Mei, J., Diao, Y., Appleton, A. L., Fang, L. & Bao, Z. Integrated materials design of organic semiconductors for field-effect transistors. *J. Am. Chem. Soc.* **135**, 6724-6746 (2013).

38 Wang, C., Dong, H., Hu, W., Liu, Y. & Zhu, D. Semiconducting π-conjugated systems in field-effect transistors: a material odyssey of organic electronics. *Chem. Rev.* **112**, 2208-2267 (2011).

39 Chua, L.-L. *et al.* General observation of n-type field-effect behaviour in organic semiconductors. *Nature* **434**, 194-199 (2005).

40 Shockley, W. A unipolar" field-effect" transistor. *Pro. IRE* **40**, 1365-1376 (1952).

41 Horowitz, G. & Delannoy, P. An analytical model for organic-based thin-film transistors. *J. Appl. Phys.* **70**, 469-475 (1991).

42 Adachi, C., Baldo, M. A., Forrest, S. R. & Thompson, M. E. High-efficiency organic electrophosphorescent devices with tris (2-phenylpyridine) iridium doped into electron-transporting materials. *App. Phys. Lett.* **77**, 904-906 (2000).

43 Deshpande, R., Bulović, V. & Forrest, S. White-light-emitting organic electroluminescent devices based on interlayer sequential energy transfer. *Appl. Phys. Lett.* **75**, 888-890 (1999).

44 Sun, Y. & Forrest, S. R. Enhanced light out-coupling of organic light-emitting devices using embedded low-index grids. *Nature Photon.* **2**, 483-487 (2008).

45 Meerheim, R., Nitsche, R. & Leo, K. High-efficiency monochrome organic light emitting diodes employing enhanced microcavities. *Appl. Phys. Lett.* **93**, 043310 (2008).

46 Xiao, Y. *et al.* Surface plasmon-enhanced electroluminescence in organic light-emitting diodes incorporating Au nanoparticles. *Appl. Phys. Lett.* **100**, 013308 (2012).

47 Kirchmeyer, S. & Reuter, K. Scientific importance, properties and growing applications of poly (3, 4-ethylenedioxythiophene). *J. Mater. Chem.* **15**, 2077-2088 (2005).

48 Lee, T.-W. *et al.* Hole-injecting conducting-polymer compositions for highly efficient and stable organic light-emitting diodes. *Appl. Phys. Lett.* **87**, 231106 (2005).

49 Lee, T. W., Chung, Y., Kwon, O. & Park, J. J. Self-organized gradient hole injection to improve the performance of polymer electroluminescent devices. *Adv. Funct. Mater.* **17**, 390-396 (2007).

50 Park, J., Kwon, Y. & Lee, T. W. Layer-by-layer spin self-assembled hole injection layers containing a perfluorinated ionomer for efficient polymer light-emitting diodes. *Macromol. Rapid Commun.* **28**, 1366-1372 (2007).

51 Png, R.-Q. *et al.* High-performance polymer semiconducting heterostructure devices by nitrene-mediated photocrosslinking of alkyl side chains. *Nat. Mater.* **9**, 152-158 (2010).

52 Shen, Y., Hosseini, A. R., Wong, M. H. & Malliaras, G. G. How to make ohmic contacts to organic semiconductors. *ChemPhysChem* **5**, 16-25 (2004).

53 Jeon, I. *et al.* A novel methodology on tuning work function of metal gate using stacking bi-metal layers. *IEDM Tech. Dige. IEEE Intl.* **1**, 303-306 (2004).

54 Giordano, L., Cinquini, F. & Pacchioni, G. Tuning the surface metal work function by deposition of ultrathin oxide films: Density functional calculations. *Phys. Rev. B* **73**, 045414 (2006).

55 Zehner, R. W., Parsons, B. F., Hsung, R. P. & Sita, L. R. Tuning the work function of gold with self-assembled monolayers derived from X-[C6H4-C꞉ C-] n C6H4-SH (n= 0, 1, 2; X= H, F, CH3, CF3, and OCH3). *Langmuir* **15**, 1121-1127 (1999).

56 Hong, J.-P. *et al.* Tuning of Ag work functions by self-assembled monolayers of aromatic thiols for an efficient hole injection for solution processed triisopropylsilylethynyl pentacene organic thin film transistors. *Appl. Phys. Lett.* **92**, 143311 (2008).

57 Sushko, M. L. & Shluger, A. L. Rough and fine tuning of metal work function via chemisorbed self-assembled monolayers. *Adv. Mater.* **21**, 1111-1114 (2009).

58 Scharber, M. C. *et al.* Design rules for donors in bulk-heterojunction solar cells - towards 10% energy‐conversion efficiency. *Adv. Mater.* **18**, 789-794 (2006).

59 Zhou, H. *et al.* Interface engineering of highly efficient perovskite solar cells. *Science* **345**, 542-546 (2014).

60 Mauger, S. A. & Moulé, A. J. Characterization of new transparent organic electrode materials. *Org. Electron.* **12**, 1948-1956 (2011).

Chapter 2.

A High-Performance *p*-Doped Conducting Polymer Blend Based on Sulfonated Polyalkoxythiophene and Poly(4-hydroxystyrene)

In this chapter, I describe our work in understanding the electrical stability of p-doped conducting polymer films when they are electrically driven. p-Doped conducting polymer films are important hole-injection or extraction layers in almost all organic semiconductor diode devices. However their electrically-induced degradation processes and possible stabilization mechanisms have been relatively little explored. We show that the commercially available p-doped conducting polymer sulfonated poly(3-methoxyethoxy-ethoxythiophene): poly(4-hydroxystyrene) (S-P3MEET:PHOST) (XA3551, Plextronics) exhibits a remarkable resilience to conductivity fading under electrical stress bias that is superior to that of neat S-P3MEET. In-situ UV-Vis, Raman, and Fourier-transform spectroscopies reveal that the doping level across S-P3MEET: PHOST films remains remarkably stable when they are driven at high dc biases. We show that the improved stability is related to the ultralow ionic conductivity of the PHOST matrix, which suppresses the coupled ion transfer mechanism needed to feed the electrochemical reaction. The ultralow conductivity further benefits from the occurrence of a solid-state esterification reaction during the baking step post film formation, which further depletes excess protons in the S-P3MEET films. The shutdown of the ionic conductivity cuts off the coupled ion transfer processes needed to cause a doping level shift in the film, affording a practical means to suppress electrically induced doping level instability.

2.1 Introduction

Recent advances in organic semiconductor synthesis have produced materials with very high levels of performance suitable for organic electronic applications in light-emitting diodes, field-effect transistors, and solar cells. However, further improvements particularly in the stability and reliability of these materials and their devices are needed to meet increasingly demanding specifications. Their behavior under electrical stress is of fundamental scientific interest and technological relevance.[1,2] In this chapter, we describe new insights gained in the understanding of the conductivity fade phenomenon and its stabilization in degenerately p-doped conducting polymers. These materials form an important class of organic semiconductors that are ubiquitously found in many device architectures. Therefore, their electrical stability ultimately limits the performance of these devices.

Poly(3,4-ethylenedioxythiophene): poly(styrenesulfonic acid) (PEDT:PSSH) is a particularly important example of a *p*-doped conducting polymer that has been in use for almost two decades.[3-7] Large current densities of the order of 10 -1000 mA cm^{-2} have to be sustained during normal operation as charge-transport layers, and hole-injection or collection layers in organic electronic devices,[4] or interconnects and electrodes in electrochromic devices, batteries, and capacitors.[7-9] Recent work has shown, however, that PEDT:PSSH exhibits a conductivity fade phenomenon just beyond these current densities.[10] This was established to be driven by solid-state electrochemical dedoping of the material at the cathode during passage of the current.[10] This electrically induced doping level shift exhibits an induction time and a threshold electric field that depend on the electrical conductivity of the film.[10] The threshold field is ~ 20 kV cm^{-1} for the 6 %(v/v) PEDT composition (with $\sigma_{dc} \approx 2 \times 10^{-4}$ S cm^{-1}) that is often used as HIL in organic light-emitting diodes.

In addition, electromigration of PEDT chain segments has also been detected,[11] although this does not appear to play a role in conductivity fading. This electrically-induced conductivity fade phenomenon can be exploited for write-once memory devices[12] that can be erased by chemical redoping.[13] One way to suppress the conductivity loss is by replacing the excess protons in PEDT:PSSH with larger cations,[10] but this degrades workfunction under some conditions because of the Madelung potential effect of the spectator ions.[14] Therefore, an alternative stabilization strategy is needed.

Sulfonated poly{thiophene-3-[2-(2-methoxyethoxy)ethoxy]-2,5-diyl}: poly(4-hydroxystyrene) (S-P3MEET:PHOST) was recently developed as a new generation of high-performance HIL that is now commercially available as XA-3551 (Solvay OLED/ Plextronics).[15] Preliminary characterizations by atomic force microscopy and UV-vis spectroscopy have been reported,[15,16] but the full chemical composition has not previously been disclosed. S-P3MEET:PHOST comprises a self *p*-doped S-P3MEET conducting polymer dispersed at a ratio of ~ 15 %(w/w) in a PHOST matrix. Their chemical structures are shown in Figure 2.1. The degree of ring sulfonation on S-P3MEET is ~ 65% according to X-ray photoelectron spectroscopy, and the doping level is thought to be 0.2−0.3 hole per ring (h^+/ ring). The counterions for these holes are the sulfonate ions on the thiophene rings. S-P3MEET:PHOST has a high workfunction of 5.0–5.2 eV, and a composition-tunable dc conductivity from 10^{-1} to 10^{-4} S cm^{-1}, similar to that of PEDT:PSSH.

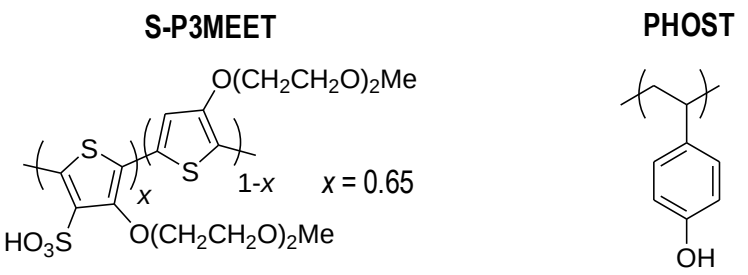

Figure 2.1. Idealized chemical structures of S-P3MEET:PHOST.

The PHOST matrix provides several key advantages. First, PHOST is considerably less acidic and hygroscopic than PSSH. This avoids acid−base reactions with substrates and overlayers.[17] Second, PHOST has a thermal degradation temperature considerably higher than that of PSSH (5% mass loss, N_2; PHOST, 375 ºC;[18] PSSH, 260 ºC[19]). Furthermore PSSH undergoes desulfonation when heated above 180 ºC, or when irradiated with UV, or even while in solution at room temperature.[20] Finally, PHOST is soluble in a variety of polar organic solvents, including lower alcohols, ketones, glycol ethers and glycol esters, but not in aromatic and chlorinated aromatic solvents. This provides S-P3MEET:PHOST with numerous processing options for a wide variety of underlayers and overlayers.

In the course of our work, we found that S-P3MEET:PHOST exhibits a surprising resilience to conductivity fading up to 60 kV cm^{-1}. Detailed analyses show that although neat S-P3MEET is vulnerable to electrically-induced drifts of its doping level, its blend with PHOST is remarkably robust. Therefore, this is a further advantage conferred by PHOST. The results suggest that while electrical instability is a fundamental characteristic of doped conducting polymers, it can be effectively suppressed without compromising work function by dispersing the conducting polymer in

a suitable ultralow ionic conductivity host. This provides a new design principle for developing high-performance doped polymer conductors with superior electrical stability.

2.2 Experimental Methods

2.2.1 Materials and film formation

S-P3MEET and S-P3MEET:PHOST (XA-3551, Solvay OLED/ Plextronics) were provided by Solvay OLED/ Plextronics and used as received. PEDT:PSSH commercial solution (Baytron P, HC Starck, Leverkusen) was used as received. Films of these materials were deposited by spin-casting on selected substrates followed by baking at 170 ºC (hot plate: 10 min) (unless otherwise stated) in a N_2 glovebox.

2.2.2 In-situ FTIR spectroscopy

The spectra were recorded in a N_2-purged Nicolet 8700 FTIR spectrometer operated with a noise floor below 1×10^{-3} absorbance unit. 300 nm thick films were spin-cast on Si wafers with 200 nm thick SiO_2 and Au source−drain interdigitated arrays with a channel length of 20 μm. The stress bias was performed in N_2 for 10 min at each applied field, and the spectra were collected *in situ* after a short period of rest (2 min) at zero bias.

2.2.3 In-situ microRaman spectroscopy

The spectra were recorded in a InVia Renishaw Raman microscope with HeNe 633-nm laser excitation focused through a 20× (NA 0.75) objective at a power that does not cause laser-induced damage, as verified by repeat measurements at the same spot. For spatially resolved studies, the spectra were collected with 2 μm spacing over the surface of the film. All films were encapsulated in N_2 for the measurements to prevent photoinduced oxidation during measurement. No bias was applied during measurement.

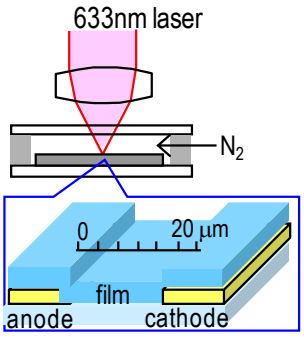

Figure 2.2 Schematic of microRaman experiment.

2.2.4 In-situ spectroelectrochemical Raman measurements

Home-built thin-layer encapsulated cells suitable for Raman spectroscopy of polymer thin films under an applied electrochemical potential were developed. The working and counter electrodes were fabricated from evaporated Au on the glass substrate and glass coverslip, respectively with Cr as the adhesion layer. A window was patterned in the counter electrode to provide optical access. The reference electrode was a Ag/AgCl thin film fabricated adjacent to the counter electrode on the same cover slip. The overlap area of the working and counter electrodes was 0.8 cm^2. The polymer film was spin-cast over the working electrode and annealed at 170 ºC (hot plate for 10 min) in the N_2 glovebox, and the excess perimeter was removed by cotton bud. This film was then encapsulated with the counter-and-reference electrode assembly using a Parafilm spacer that also provided a hermetic seal. The enclosed space was then filled with 0.10 M NBu_4PF_6 in anhydrous acetonitrile and sealed in the glovebox.

Cyclic voltammetry data were collected for the encapsulated polymer films in contact with the thin-layer electrolyte in the standard potentiostat mode using a Keithley 4200 semiconductor parameter analyzer, at a scan rate of 10 mV s^{-1} between −0.7 V and 0.15 V versus Ag/AgCl. Raman spectra

with 633 nm HeNe laser excitation was collected simultaneously through a microscope with a 50× (NA 0.7) objective through the optical access window. A blank measurement without the polymer film found a variable solvent background on the order of a few milliamperes per square centimeter, but no electrochemical current peaks. Hence, all the features observed were due to the polymer films.

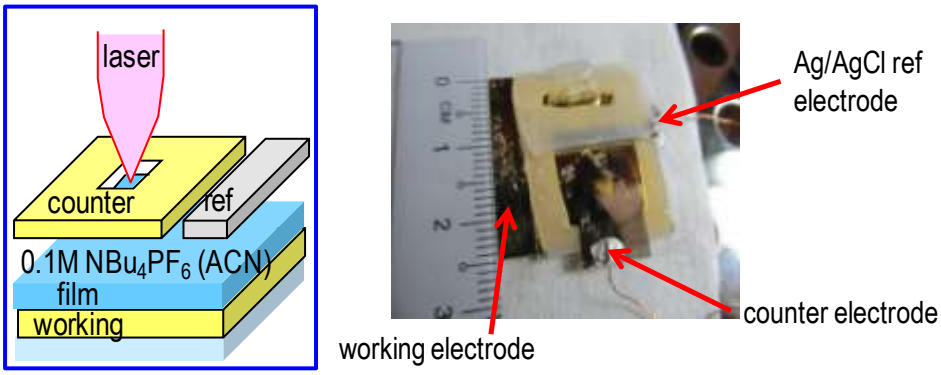

Figure 2.3 Schematic of spectroelectrochemical Raman experiment. The reference electrode is a Ag/AgCl thin film fabricated adjacent to the counter electrode.

2.2.5 Differential scanning calorimetry

S-P3MEET was formulated into PHOST to give a weight ratio of 7.5% and homogenized on a vortex mixer. For references, samples of PHOST, S-P3MEET, and 15% (w/w) S-P3MEET:PHOST were also studied; 4−5 mg portions of these samples were cast into Al sample pans at 95°C in air, annealed to 120 or 170 °C for 10 min in N_2, and then dried overnight in vacuum to completely remove solvents before the lids were crimped onto the pans. DSC thermograms were collected at a ramp rate of 10 °C min^{-1} in flowing N_2 after equilibration at −50 °C. No transitions were found between −50 °C and room temperature. After the samples had reached 200 °C, the ramp direction was reversed to cool the samples to −50 °C. Only data from the ramp-up half-cycle are presented

in this chapter. The data from the ramp-down half-cycle were used to confirm the identification of the heat capacity steps.

2.2.6 X-ray photoemission spectroscopy

XPS was performed using Mg Kα X-rays (1253.6 eV) on a VG ESCALab Mk-II spectrometer operated at a base pressure of < 1×10^{-9} mbar, with sample grounded, and with a 0.7-eV spectrometer resolution set by a constant pass energy of 20 eV. The measured C 1s, O 1s and S 2p core-level photoemission spectra were integrated and corrected by empirical atomic photoemission cross sections to give the relative carbon and sulfur atomic concentrations sampled within the inelastic electron mean free path (≈ 25 Å) from the surface.

2.3 Results and Discussions

2.3.1 Resistance to conductivity fading in S-P3MEET:PHOST

Figure 2.4 shows the normalized in-plane dc conductance of S-P3MEET (bottom) and S-P3MEET:PHOST (top) films, measured under N_2 as a function of electrical stress bias time. These films were spin-cast on lithographically-patterned Au source−drain electrode arrays and annealed at 170ºC (10 min) in N_2. The S-P3MEET film shows stable conductance to applied fields up to 10 kV cm^{-1}, for at least 5×10^4 s. However, at 20 kV cm^{-1} or larger, its conductance decays after an induction time of ~ 60 s, and falls below 50% of the initial value by 600 s. This is similar to the behavior of PEDT:PSSH that we have reported previously.[10] The conductance loss does not recover on resting. In contrast, the S-P3MEET:PHOST film shows stable conductance to applied fields up to 60 kV cm^{-1}. At 120 kV cm^{-1}, the normalized conductance falls below 50% after 10^3 s. If we define the threshold field for conductivity fading to be that which causes conductance to drop to 50% after 10^3 s, this threshold field is approximately 80−120 kV cm^{-1} for S-P3MEET:PHOST. This is a factor of 4−5 as large as that of S-P3MEET (approximately 15−20 kV cm^{-1}), and PEDT:PSSH at the same σ_{dc}.[10]

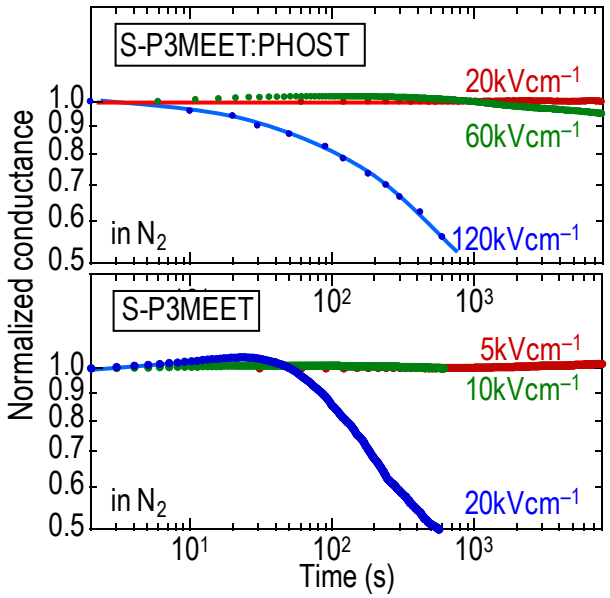

Figure 2.4 Selected conductance−time plots of S-P3MEET:PHOST (top) and neat S-P3MEET (bottom) films, measured in N_2 as a function of stress bias time at various average applied electric fields. S-P3MEET shows conductivity fading above a threshold field of approximately 15−20 kV cm^{-1}; and S-P3MEET:PHOST above approximately 80−120 kV cm^{-1}. This threshold field is defined as that required to cause conductance to drop by a factor of 2 after 10^3 s.

2.3.2 Injection induced dedoping in S-P3MEET

We show here that conductivity fading in neat S-P3MEET also arises from a solid-state electrochemical mechanism that shifts its doping level. Figure 2.5 shows the *insitu* infrared transmission spectra of S-P3MEET (bottom) and S-P3MEET:PHOST (top) films measured in N_2, after stress-bias for 10 min at various fields. Self *p*-doped S-P3MEET has a polaron absorption tail onset above 1500 cm^{-1} and infrared active vibrational (IRAV) modes between 890 and1520 cm^{-1}. The film loses both its polaron and IRAV bands when the bias reaches 20 kV cm^{-1} and gains a new absorption band at a wavelength of 495 nm, which is the $\pi-\pi^*$ absorption of undoped S-P3MEET.

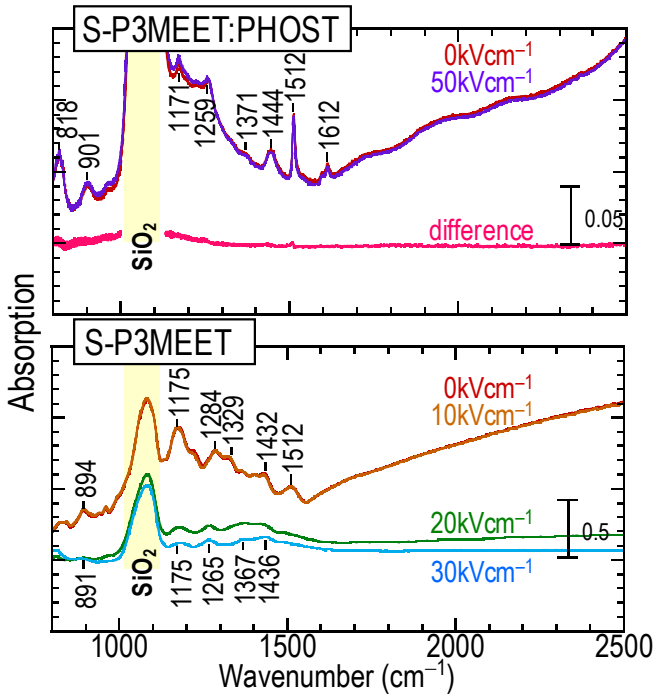

Figure 2.5 FTIR transmission spectra of film before and after electrical-stress bias for 10 min in N_2. Bottom: S-P3MEET, top: S-P3MEET:PHOST. The difference spectrum (magenta) shows that the underlying polaron and IRAV bands of the *p*-doped S-P3MEET in the blend has not changed with bias up to 50 kV cm^{-1}.

This shows that the self-*p*-doped S-P3MEET film on average undergoes dedoping when biased above the conductivity fading threshold.

In contrast, the same S-P3MEET dispersed in PHOST survives beyond 50 kV cm^{-1}. To detect any possible change in the underlying polaron and IRAV features that are now dominated by PHOST modes [1612 (ν ring), 1512 (ν ring), 1444 (ν ring), 1259 (ν ring -OH), 1171 (δ_{ip} ring -H), 818 (δ_{oop} ring -H) cm^{-1}], we checked the difference spectrum. This difference spectrum (magenta plot in Figure 2.5a) is flat, which shows the polaron and IRAV features have not changed. Also the UV-vis spectrum, shown in Figure 2.6, has not changed. Therefore, S-P3MEET surprisingly becomes resilient to electrically induced doping-level shifts when it is dispersed in PHOST.

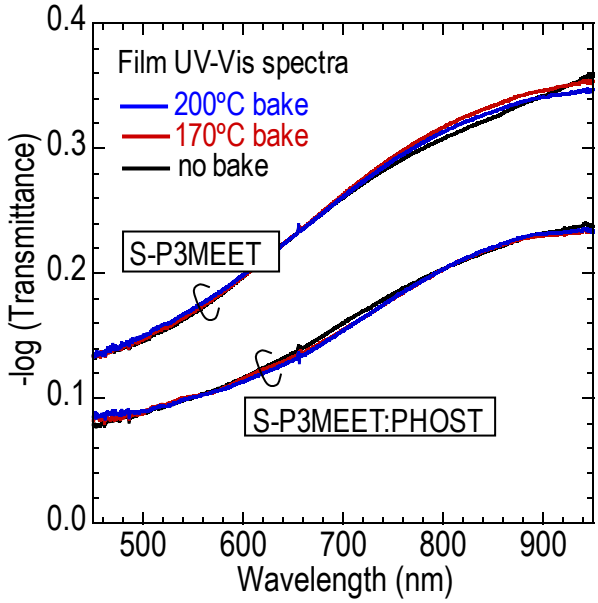

Figure 2.6 –log (Transmittance) UV-Vis-NIR spectra of S-P3MEET:PHOST and S-P3MEET films before (black) and after annealing to 170°C (red) and 200°C (blue), 10 min (hotplate) under N_2. The invariance of the spectra shape indicates that there is no change in doping level and electronic structure with annealing to 200°C.

To determine whether annealing the films induces a change in the polaron character of pure S-P3MEET and S-P3MEET:PHOST, the polymer films were probed by UV-Vis spectroscopy before and after heat treatment. Spin-cast films on spectrosil® were annealed at 170ºC and 200ºC for 10 min and the UV-Vis spectra collected. All preparations and measurements were done in the glove-box. Figure 2.6 shows the UV-Vis-NIR –log(transmittance) spectra for S-P3MEET:PHOST and S-P3MEET films before (black) and after annealing to 170 ºC (red) and 200 ºC (blue). There is no significant change in the polaron spectrum with heat treatment.

2.3.3 Doping level by micro-Raman spectroscopy

To evaluate the possible complex changes in doping level across the film, we performed micro-Raman spectroscopy on S-P3MEET across the electrode gap before and after stress bias. This technique has previously been used to resolve electrochemical changes in PEDT and in a blue light-emitting polymer under device operation.[1,2] The films were encapsulated in N_2 to avoid laser damage and possible interaction with oxygen and moisture.[21]

Figure 2.7 shows a set of spectra for S-P3MEET after electrical biasing at 25 kV cm^{-1}, just above the threshold field. The spectra were background corrected and normalized to the peak intensity at 1435 cm^{-1}. The 1300−1600 cm^{-1} region corresponds to ring breathing and inter-ring vibrational modes of the thiophene polymer backbone.[5,22] This region is therefore sensitive to the doping level of the polymer. After bias, the most prominent changes are the decrease in intensity of the 1500 and 1535 cm^{-1} modes in a 5 μm wide region next to the anode, but an increase next to the cathode. These changes do not recover upon removal of the field. Therefore, the doping level across the film has been irreversibly modified by passage of current above the conductivity fade threshold.

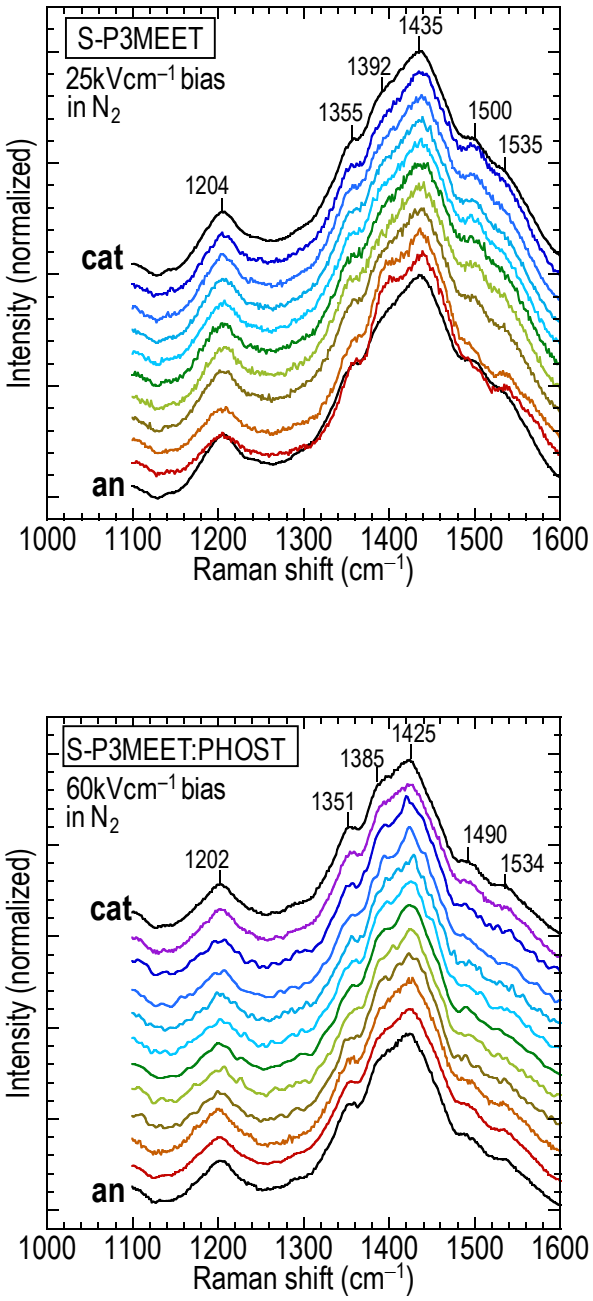

Figure 2.7 MicroRaman spectra of S-P3MEET and S-P3MEET:PHOST films collected at 2-μm sample spacing after pre-bias in N_2 for 10 min at 25 kV cm^{-1} and 60 kV cm^{-1} respectively.

To identify the direction of the shift of the doping level, a spin-cast film of the self-*p*-doped S-P3MEET was deliberately further oxidized with H_2O_2 and its Raman spectrum recorded (Figure 2.8).

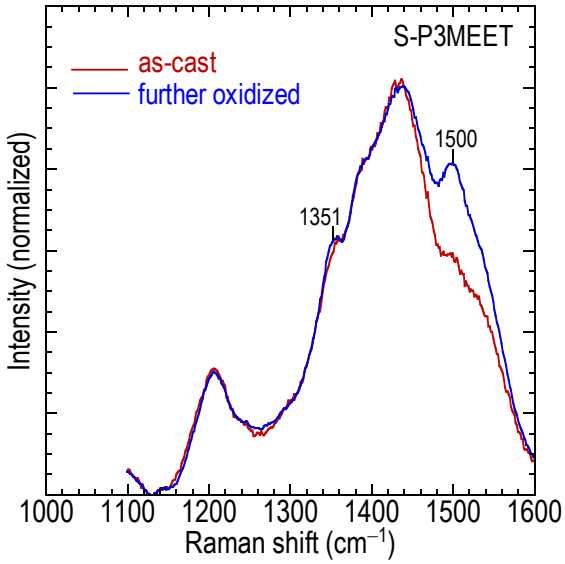

Figure 2.8 Raman spectra of S-P3MEET film as-cast (red) and after further oxidation (blue) by a 10 s contact with 30 % (w/w) hydrogen peroxide.

This spectrum shows an increase in the intensities of the 1500 and 1535 cm^{-1} modes relative to that of the 1350 cm^{-1} mode in the heavily doped regime. Therefore, the ratio of the spectral intensities at 1500 to 1350 cm^{-1} (I_{1500}/ I_{1350}) is a proxy for the doping level of S-P3MEET. This is further confirmed by spectroelectrochemical Raman measurements in the underdoped regime (Figure 2.11, vide infra). From this, we conclude that the changes observed in Figure 2.7 arise from a decrease (increase) in the doping level in the vicinity of the anode (cathode). The maximal change was estimated to be on the order of tens of percent, but a precise quantification was not yet possible. The finding of dedoping of the film in the vicinity of the anode, where oxidation is

normally expected to occur, is counterintuitive, but not impossible. This is because the electrochemical reaction needs to be situated where ions are available to complete the Faradaic process (vide infra).

To further check for possible heterogeneity effects, we performed two-dimensional micro-Raman mapping on a different S-P3MEET film and constructed a map of $\log(I_{1500} / I_{1350})$ to quantify the relative doping level across the film. Figure 2.9 shows a strip of this map. The map shows the final doping level fluctuates over the film but a narrow strip of overdoped material clearly forms along the cathode edge. The doping level over the electrodes does not change significantly, however, so the effect is not simply driven by electric potential but requires the passage of current. In contrast, S-P3MEET:PHOST does not show any change in its micro-Raman spectra after prebiasing to 60 kV cm^{-1} (Figure 2.7).

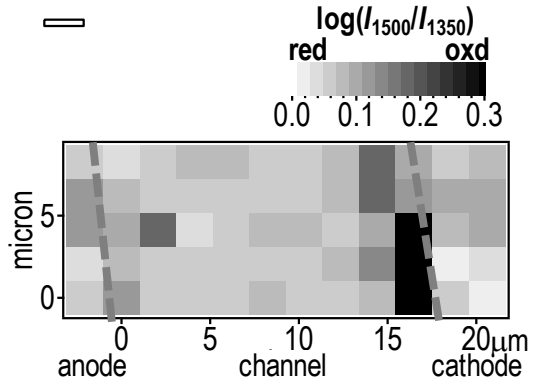

Figure 2.9 Micro-Raman map of a 20 μm wide electrode gap region in S-P3MEET film after prebiasing to the conductivity fade threshold. The scale bar gives the doping level in arbitrary units (red for reduced and oxd for oxidized)

These results are significant because they generalize the conductivity fade phenomenon that was previously observed in PEDT:PSSH, where it was associated with localized dedoping. Here it is

clear that this doping level instability can occur in both directions, i.e., both dedoping and overdoping, as one would *a priori* expect. Because electrical conductivity typically shows a maximum at an intermediate doping level due to lack of hopping redox sites in the case of lower doping level and intermolecular deformation of the conducting polymer in the case of higher doping,[3,5,23] the dedoping and overdoping can ultimately cause electrical conductivity to fall. Furthermore, the results show that dedoping (or over-doping) can occur at either contact, depending on the supply of counterions. This will be discussed below.

2.3.4 Role of ionic conductance in the stability of S-P3MEET:PHOST

The fundamental processes responsible for electrochemical modification of the doping level in devices are schematically illustrated in Figure 2.10. Two types of processes are required: the reduction or oxidation of the polymer segment (in general P, P^+, or P^-) by a carrier injected at one contact and the generation of the requisite counterion at the other contact. Let us consider the case of an increase in positive charge on a polymer segment by one unit, i.e., oxidation or trapping of a hole on that segment. This has to be counterbalanced by the transfer of 1 equiv of an anion into the vicinity of that segment, or 1 equiv of a cation out of its vicinity, to preserve charge neutrality. Otherwise, the space charge density created would become unsustainable. For example, if an initial *p*-doping density of 2×10^{20} cm^{-3} were to increase by 10%, the positive space charge density formed would be 2×10^{19} cm^{-3} in the absence of charge compensation, which would yield an electric field gradient on the order of 10^{13} V cm^{-2}!

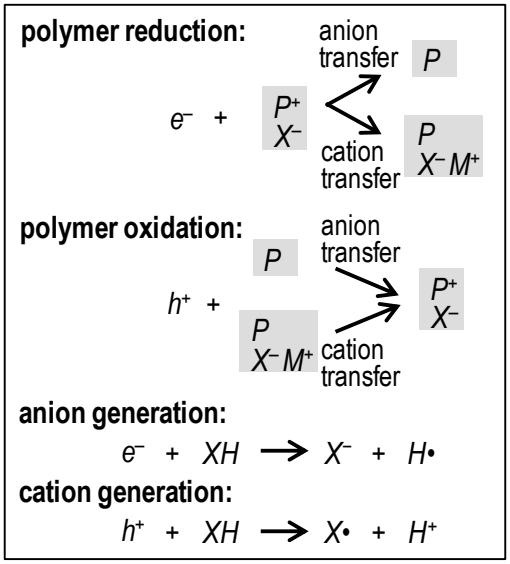

Figure 2.10 Schematic of coupled electron−ion transfers required to produce doping-level shifts in organic semiconductor films, illustrated with two examples of charge injection into polymer segments (P for the neutral polymer segment; P+ for the positively-charged polymer segment) at one contact, and two examples of ion generation (XH for the hydrogen-containing functional group) at the other contact.

If the anion is highly mobile, or the background ion density is high, the requisite anion can be readily supplied to the anode contact, so the polymer segment can be locally oxidized there. This is the usual situation in electrochemistry with a supporting electrolyte. However, if the anion in less mobile and the background ion density is low, the anion generated at the cathode may not be able to reach the anode. In this case, the irreversible oxidation of the polymer segment is confined to occur at the cathode where the anion is generated. This appears to be the case here.

The requisite ion transfer appears to be satisfied by an ionic conductivity σ_{ion} as low as 10^{-12} S cm^{-1}! To derive this, consider the amount of anions required to compensate for an increase in the positive doping charge density of 2×10^{19} cm^{-3} in a 100 nm wide region. These ions can be supplied in 10^3 s at 10 kV cm^{-1} by a σ_{ion} of 3×10^{-12} S cm^{-1}. To shut down the electrochemical mechanism, one therefore needs to depress σ_{ion} by several orders of magnitude below this value.

This requires the concentration or mobility (or both) of the ions to be exceedingly low. The process is thus fundamentally the same as that in an electrochemical cell, except that it occurs here in the solid state without the deliberate addition of electrolytes, albeit at a much longer but still relevant time scale.

We attribute the superior electrical stability of S-P3MEET:PHOST to the much lower σ_{ion} in PHOST than in PSSH or in neat S-P3MEET. Accurate measurement of σ_{ion} in the ultralow regime 10^{-12} S cm^{-1} is not readily possible. For reference, the proton σ_{ion} in hydrated PSSH films at room temperature and 30% relative humidity (where $[H_2O]$/ [sulfonic acid] ≈ 2) is ~ 1×10^{-3} S cm^{-1}.[24] This decreases by several orders of magnitude when the film becomes anhydrous, but the ultimate σ_{ion} is still likely to be > 10^{-12} S cm^{-1}.[25] In contrast, PHOST is a markedly poorer proton conductor because of the much lower acidity of its hydroxyl protons and the less extensive hydrogen bonding network. From high-temperature data, we extrapolated its σ_{ion} to be < 1 x 10^{-12} S cm^{-1} at 30% relative humidity at room temperature and $\ll$ 1 x 10^{-13} S cm^{-1} in the anhydrous state.[26] The low σ_{ion} in PHOST is thus consistent with our mechanism. Further reduction in σ_{ion} by proton substitution may thus be useful in this regard.

2.3.5 Electrochemical stability of S-P3MEET:PHOST

Does the intrinsic electrochemical stability of S-P3MEET play a role? To check this, we performed *insitu* spectroelectrochemical Raman measurements on S-P3MEET and S-P3MEET:PHOST films by potential cycling in a home-built three-electrode thin-layer cell with 0.1 M NBu_4PF_6 in acetonitrile

as the supporting electrolyte. The potential cycling was performed at 10 mV s^{-1} from 0.0 to –0.7 V, and then at 0.15 V and back to 0.0 V versus Ag/AgCl.

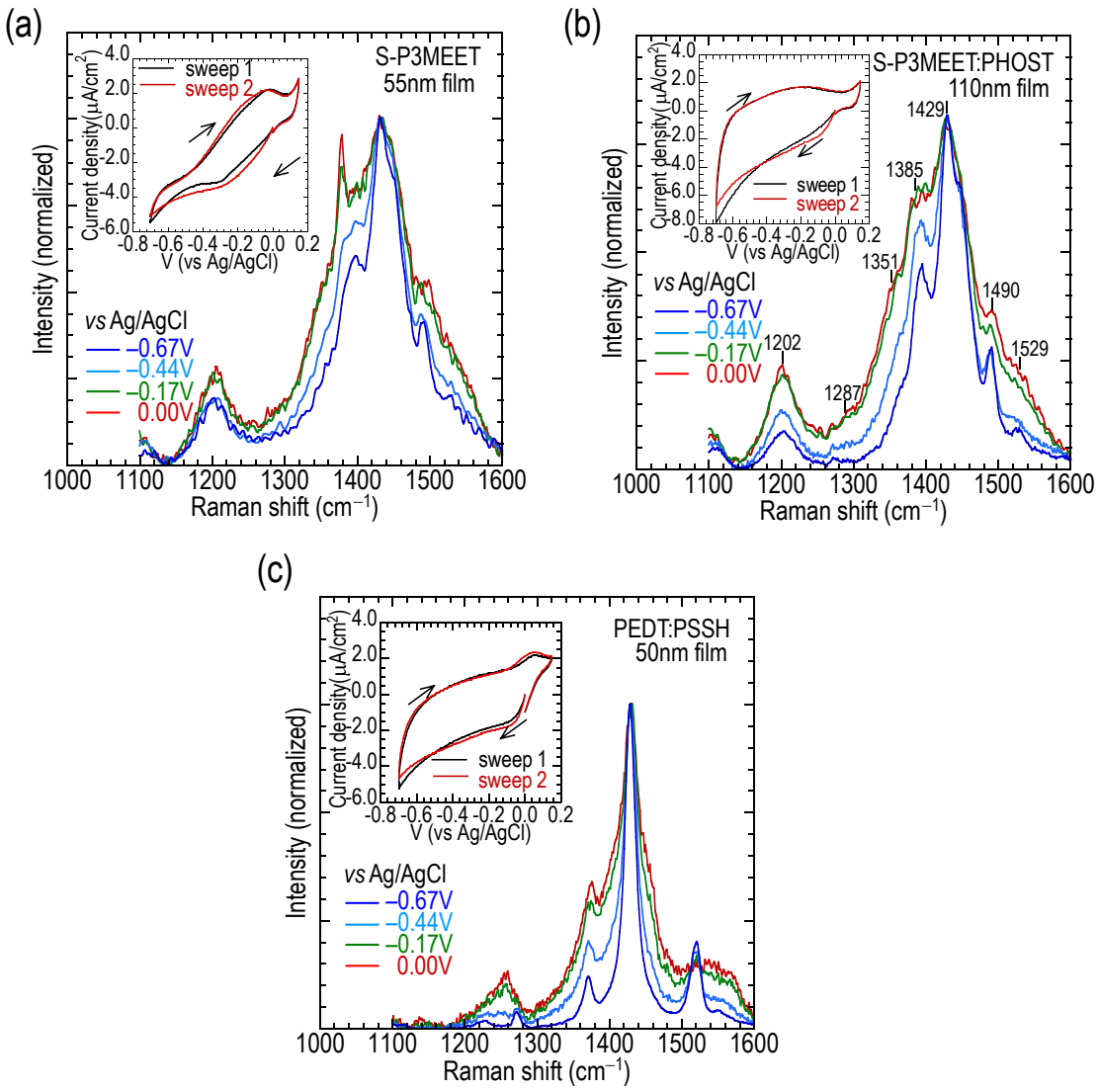

Figure 2.11 Electrochemical potential dependent micro-Raman spectra of **(a)** S-P3MEET, **(b)** S-P3MEET:PHOST, and **(c)** PEDT:PSSH thin films. To reveal the changes in the spectral band shape, the spectra were normalized to the intensity at 1430 cm^{-1}. Insets are cyclic voltammograms recorded during the experiment.

Panels a and b of Figure 2.11 show the data for S-P3MEET and S-P3MEET:PHOST respectively. The cyclic voltammograms were reversible for S-P3MEET: PHOST and S-P3MEET, which suggests that degradation and/or dissolution of the polymer does not occur. No difference in the cycle characteristics of S-P3MEET:PHOST and S-P3MEET was found. Therefore, PHOST does not confer an unusual electrochemical stability to the *p*-doped S-P3MEET dispersed in it, under the conditions used in these experiments. In contrast, PEDT:PSSH undergoes more facile dedoping than S-P3MEET or S-P3MEET:PHOST under the same conditions (Figure 2.11c). The PEDT:PSSH band shape is considerably narrower than that of S-P3MEET or S-P3MEET:PHOST at −0.67 V. This shows that the PEDT has more closely reached the fully dedoped state, as suggested also by integration of the reduction current.

2.3.6 Role of PHOST in the stability of S-P3MEET:PHOST

Next, we show that the PHOST is not an inert spectator but a reactive matrix toward S-P3MEET. The S-P3MEET has been determined to form a miscible blend with PHOST. S-P3MEET:PHOST films are typically annealed at 170−200°C for 10 min in N_2 for device fabrication. UV–vis–NIR spectroscopy shows that this does not cause a large change in the polaron spectrum at wavelengths 450−1000 nm.

However, the glass transition temperature (T_g) of PHOST shows a large downshift in the presence of S-P3MEET (Figure 2.12a). Differential scanning calorimetry shows that PHOST has a T_g of 165ºC, while neat self-*p*-doped S-P3MEET does not show any perceptible T_g in the measured temperature range. When S-P3MEET was mixed into PHOST at 7.5 %(w/w), and dried at 120 ºC, T_g decreases to 100 ºC. When the sample was further annealed to 170 ºC, T_g increases to 120ºC.

The initial sizable reduction in T_g suggests that S-P3MEET is intimately mixed, i.e., miscible, with PHOST and that mixing generates free volume in the matrix. Thus, PHOST acts as the matrix for molecularly dispersed S-P3MEET.

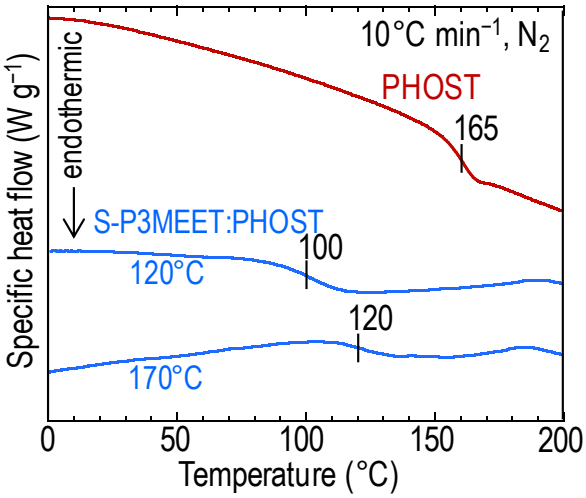

Figure 2.12 Differential scanning calorimetry thermograms for PHOST preannealed at 170°C in N_2 and S-P3MEET:PHOST preannealed at 120 and 170 ºC.

This remarkable compatibility appears to be underpinned by a solid-state reaction between the sulfonic acid group of S-P3MEET and the hydroxyl group of PHOST. This reaction produces a sulfonate ester, which has a thermal stability better than the sulfonic acid. Figure 2.13 shows the S 2p core level X-ray photoelectron spectra of *p*-doped S-P3MEET films after different heat treatment temperatures up to 200 ºC in N_2. The S 2p core levels of the thiophene ring and the pendant sulfonic acid/ sulfonate (i.e., $-SO_3$) group can be resolved (S $2p_{3/2}$, thiophene, 163.5 eV; $-SO_3$, 168.0 eV). The thiophene S 2p spectrum can be accurately fitted to a vibronic progression for the *p*-doped state[11] to give the number of $-SO_3$ groups per thiophene repeat unit. The inset of Figure

2.13 shows the dependence of this ratio on heat treatment temperature for S-P3MEET and S-P3MEET:PHOST.

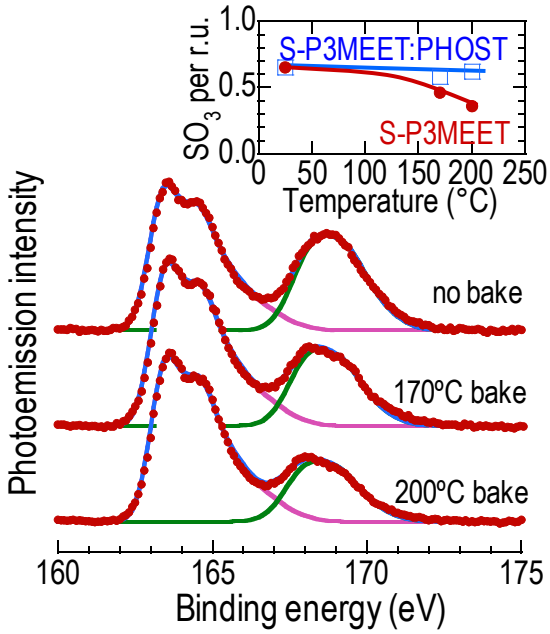

Figure 2.13 S 2p core level spectra of a S-P3MEET film before and after different heat treatments in N_2. Each spectrum is curve-fitted for thiophene and sulfonate. Symbols, data; smooth blue line, fitted sum; smooth purple, thiophene; smooth green, sulfonate. The inset is a plot of sulfonate per thiophene repeat unit vs annealing temperature, derived from S 2p core level spectra.

The key finding is that S-P3MEET loses 50–60% of $–SO_3$ groups after being heated to 200 ºC, but S-P3MEET:PHOST does not lose $–SO_3$ groups at all. The thermal desulfonation of aromatic sulfonic acids is a well-known reaction.[19] The results suggest that the $–SO_3$ group in S-P3MEET:PHOST is not in the labile sulfonic acid form, but the salt or ester form.

To determine whether annealing induces change in S-P3MEET and S-P3MEET:PHOST, the polymer films were probed by difference Fourier transform infrared (FTIR) spectroscopy before and

after heat treatment. Spin-cast films on intrinsic Si wafer were annealed at 200ºC for 10 min in N_2 and the FTIR spectra collected. Figure 2.14 shows the FTIR spectra of S-P3MEET and S-P3MEET:PHOST films before and after baking at 200°C in N_2.

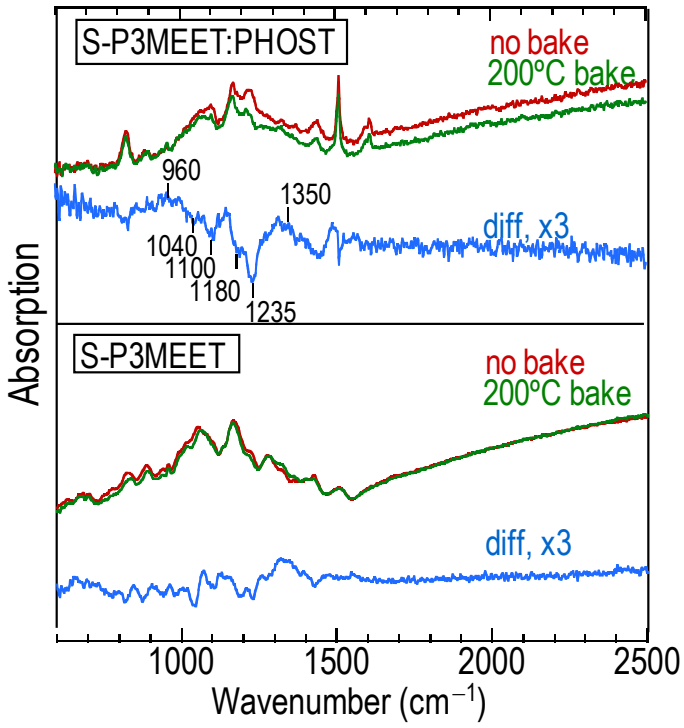

Figure 2.14 FTIR spectra of S-P3MEET:PHOST (top) and S-P3MEET (bottom) thin film before (red) and after annealing to 200°C for 15 min in N_2 (green). The difference spectra (blue) show the loss of C-OH vibrations in S-P3MEET:PHOST at 1230 cm^{-1} after annealing.

The S-P3MEET:PHOST spectra indicate intensity losses at 1235 and 3330 cm^{-1} but intensity gains at 960 and 1350 cm^{-1}. These four modes can be assigned to ν ring–OH, ν O–H, ν SO_2–OR and ν_{as} SO_2, respectively.[27,28] They are not coupled to the polaron and hence remain as good group frequencies. Also, the sulfonate intensities of S-P3MEET at 1180 (ν_s SO_3^-) and 1100 cm^{-1} (ν ring–SO_3) decrease, and new modes at 960 and 1350 cm^{-1} emerge, which can be assigned to ν SO_2–

OR and ν_{as} SO_2, respectively. These changes suggest a solid-state esterification reaction between the sulfonic acid and hydroxyl groups. The neat S-P3MEET and PHOST films do not show these changes.

To confirm this transformation, we have performed a model study of poly(vinyl alcohol) doped with a 1:1 molar ratio (by repeat unit) of *p*-toluenesulfonic acid (PVA:TSA) to avoid spectral interference in the 1150–1250 cm^{-1} spectral region. The results provide definitive evidence of such a chemical transformation at 120 °C, with further details given in section 2.3.7. Altogether, the results strongly point to an esterification reaction in S-P3MEET:PHOST. The resultant cross-linking does not appear to generate sufficiently large stresses to crack the film.

This esterification reaction appears to scavenge the excess sulfonic acid groups present in S-P3MEET, thereby serendipitously limiting their contribution to σ_{ion}. To find indications for this, we measured the stress-bias characteristics at 60 kV cm^{-1} for a S-P3MEET:PHOST film dried under vacuum without annealing and one annealed to 170°C to promote the esterification. The unannealed film shows a larger excursion in conductance than the annealed film. This suggests that the presence of residual sulfonic acid groups in the unannealed (but dry) film leads to more facile doping-level shifts (Figure 2.15).

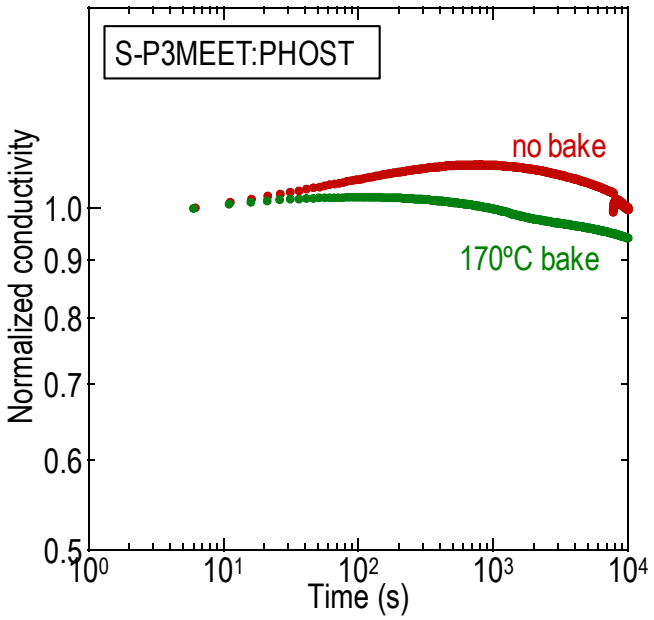

Figure 2.15 Conductivity-time plots of S-P3MEET:PHOST films with and without annealing measured at 60 kV cm^{-1} in N_2.

2.3.7 Role of esterification in the stability of S-P3MEET:PHOST

We have separately acquired unambiguous spectroscopic evidence for the formation of sulfonate esters from a solid-state condensation reaction between sulfonic acid and hydroxyl groups in a model system of poly(vinyl alcohol) doped with 1:1 mol/mol (repeat unit) *p*-toluenesulfonic acid (PVA:TSA). PVA and 1:1 molar ratio of PVA:TSA films were cast on intrinsic Si wafers. The FTIR spectra of these films were collected in N_2 after different heat treatments up to 170ºC also conducted in N_2. Figure 2.16a shows the FTIR spectra of the PVA film. The results show that the infrared spectrum of PVA does not change perceptibly with heat treatment up to 170 °C. Likewise, the infrared spectrum of PHOST does not change perceptibly with heat treatment up to 200 ºC.

Figure 2.16 shows the corresponding spectra of the PVA:TSA film. The spectrum of the pristine film is a composite of features from both PVA and TSA. In particular the ν OH mode (3360 cm^{-1}) of PVA persists substantially unchanged in intensity relative to the ν CH_2 modes (2918 and 2943 cm^{-1}). New modes appear due to the TSA: 815 (δ_{oop} ϕ–H); 1010 and 1035 (δ_{ip} ϕ–H); 1100 (ν ϕ–S); 1125, 1170 and 1220 cm^{-1} (ν_s and ν_{as}: $-SO_3^-$); 1497 and 1600 (ν C–C ϕ); 2350 and 2700 cm^{-1} (ν H_3O^+). This shows that the TSA exists primarily in the hydrated ionized sulfonate form in PVA. The infrared vibrational mode frequencies of authentic anhydrous and hydrated forms of TSA are known in the literature, which have been used for assignment here.

Upon heating to 120 ºC, pronounced changes are found in the FTIR spectrum in both the PVA and TSA vibrational modes. The O–H band (3360 cm^{-1}) of PVA greatly diminishes in intensity, and one of its C–H bands redshifts to 2860 cm^{-1}. Concomitantly, the ionic sulfonate bands also greatly diminish in intensity, and new features characteristic of the anhydrous TSA appears: 905 (ν: $-SO_2-OH$), 1175 (ν_s: $-SO_2-$) and 1350 cm^{-1} (ν_{as}: $-SO_2-$). This demonstrates that at this stage, the TSA exists primarily in the dehydrated form, as anhydrous sulfonic acid. This is confirmed by the loss of intensities of the 1010 and 1035-cm^{-1} δ_{ip} ϕ–H modes which are known separately to absorb strongly when coupled to the sulfonate anion but weakly when coupled to the non-ionic sulfonic acid. Anhydrous TSA is a strong acid that can be expected to catalyze the dehydration of the PVA to give ether and sulfonate ester formation. Indeed there is direct spectroscopic evidence for formation of the latter. There is emergence of intensities at 905 (ν: $–SO_2–OR$), 1205 cm^{-1} (ν_s: $–SO_2–$) and 1368 cm^{-1} (ν_s: $–SO_2–$), which are characteristic of sulfonate esters. With increasing heat treatment temperature, the acetate C=O band (impurity due to incomplete hydrolysis of PVAc

during manufacture of PVA) at 1740 cm^{-1} also diminishes due to acid catalysis and subsequent volatilization of the acetic acid liberated.

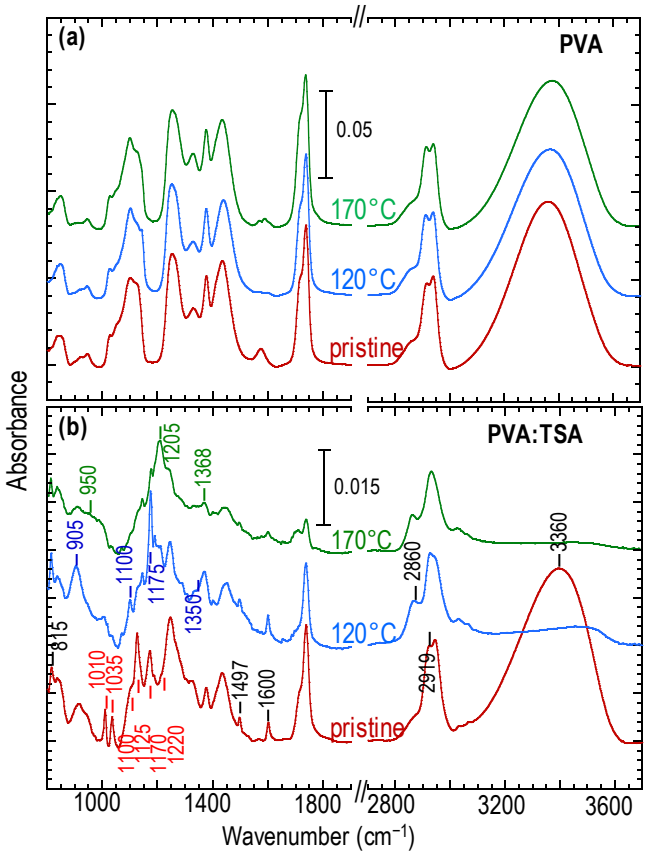

Figure 2.16 Infrared spectroscopic evidence for a thermal-induced sulfonate ester formation in the solid state in a 1:1 mol/mol (repeat unit) poly(vinyl alcohol): *p*-toluenesulfonic acid blend (PVA:TSA) model system. FTIR spectra of thin films of: **(a)** PVA, and **(b)** PVA:TSA, subjected to various heat treatment temperatures. The red ticks mark the key sulfonate-related modes of the hydrated *p*-toluenesulfonic acid. These dominate the TSA contribution in the as-cast film. The blue ticks mark the key sulfonic acid-related modes of the anhydrous *p*-toluenesulfonic acid. These emerge in the film baked at 120 ºC. The green ticks mark the expected sulfonate ester modes. These emerge in the film baked at 120 ºC and dominate the film baked at 170 ºC.

This transformation is practically complete at 170ºC. The characteristic modes of anhydrous sulfonic acid at 905 and 1175 cm^{-1} greatly diminish in intensity, leaving a broad band at 950 cm^{-1} and a dominant band at 1205 cm^{-1}. It is clear that the C–O skeletal modes of PVA in the 1250–1450-cm^{-1} have also changed significantly. Hence it is clear that at this stage, the TSA exists primarily in the sulfonate ester state. This demonstrates the formation of sulfonate esters from sulfonic acids embedded in a polyhydroxyl matrix.

2.4 Conclusions

Understanding the fundamental mechanisms of electrical degradation or instability in organic semiconductor devices is a key step toward their rational design for higher performance and more demanding applications. Here we reported the successful suppression of the conductivity fade phenomenon that occurs in doped conducting polymers when they are stress-biased with a large electric field or current density. While poly(3,4-ethylenedioxythiophene): poly(styrenesulfonic acid) (PEDT:PSSH) shows a relatively low threshold to conductivity fading, the recently developed sulfonated poly{thiophene-3-[2-(2-methoxyethoxy)ethoxy]-2,5-diyl}: poly(4-hydroxystyrene) (S-P3MEET:PHOST), which is an intimate blend of S-P3MEET and PHOST, is far more resilient. Insitu UV-vis, Raman, and Fourier-transform infrared spectroscopies revealed that the doping level across S-P3MEET:PHOST films remains remarkably stable when they are driven at high dc biases. Spectroelectrochemical Raman measurements suggest that both S-P3MEET and S-P3MEET:PHOST are also less susceptible to electrochemical dedoping than PEDT:PSSH. Comparison of the conductivity fading characteristics of S-P3MEET in the presence or absence of PHOST, however, revealed a large matrix effect. We obtained evidence that the enhanced electrical stability of S-P3MEET:PHOST results from its inherent ultralow ionic conductivity, further suppressed by a serendipitous scavenging of excess sulfonic acid protons on S-P3MEET through a solid-state esterification reaction with PHOST during annealing. The shutdown of the ionic conductivity cuts off the coupled ion transfer processes needed to cause a doping level shift in the film. This affords a practical means of suppressing the electrically induced doping level instability in doped conducting polymer systems.

2.5 References

1 Kim, J. S., Ho, P. K. H., Murphy, C. E., Baynes, N. & Friend, R. H. Nature of non-emissive black spots in polymer light-emitting diodes by in-situ micro-raman spectroscopy. *Adv. Mater.* **14**, 206-209 (2002).

2 Kim, J. S. *et al.* Electrical degradation of triarylamine-based light-emitting polymer diodes monitored by micro-Raman spectroscopy. *Chem. Phy. Lett.* **386**, 2-7 (2004).

3 Morvant, M. C. & Reynolds, J. R. In situ conductivity studies of poly(3,4-ethylenedioxythiophene). *Synth. Met.* **92**, 57-61 (1998).

4 Groenendaal, L. B., Jonas, F., Freitag, D., Pielartzik, H. & Reynolds, J. R. Poly(3,4-ethylenedioxythiophene) and Its derivatives: past, present, and future. *Adv. Mater.* **12**, 481-494 (2000).

5 Lapkowski, M. & Proń, A. Electrochemical oxidation of poly(3,4-ethylenedioxythiophene) - "in situ" conductivity and spectroscopic investigations. *Synth. Met.* **110**, 79-83 (2000).

6 Kvarnström, C., Neugebauer, H., Ivaska, A. & Sariciftci, N. S. Vibrational signatures of electrochemical p- and n-doping of poly(3,4-ethylenedioxythiophene) films: an in-situ attenuated total reflection Fourier transform infrared (ATR-FTIR) study. *J. Mol. Struct.* **521**, 271-277 (2000).

7 Kirchmeyer, S. & Reuter, K. Scientific importance, properties and growing applications of poly(3,4-ethylenedioxythiophene). *J. Mater. Chem.* **15** (2005).

8 Conway, B. E. *Electrochemical supercapacitor, scientific fundamentals and technological applications*. (Kluwer Academic /Plenum Publishers, 1999).

9 Groenendaal, L. B., Zotti, G., Aubert, P. H., Waybright, S. M. & Reynolds, J. R. Electrochemistry of poly(3,4-ethylenedioxythiophene) derivatives. *Adv. Mater.* **15**, 855-879 (2003).

10 Chia, P. J. *et al.* Injection-induced de-doping in a conducting polymer during device operation: asymmetry in thoe hole injection and extraction rates. *Adv. Mater.* **19**, 4202-4207 (2007).

11 Png, R. Q. *et al.* Electromigration of the conducting polymer in organic semiconductor devices and its stabilization by crosslinking. *Appl. Phys. Lett.* **91**, 013511 (2007).

12 Möller, S., Perlov, C., Jackson, W., Taussig, C. & Forrest, S. R. A polymer/semiconductor write-once read-many-times memory. *Nature* **426**, 166-426 (2003).

13 Chia, P. J., Yeo, Y. C., Burroughes, J. H., Friend, R. H. & Ho, P. K. H. Chemical reversability of the electrical dedoping of conducting polymers: An organic chemically erasable programmable read-only memory. *Appl. Phys. Lett.* **93**, 033314 (2008).

14 Chia, P. J. *et al.* Direct evidence for the role of the Madelung potential in determining the work function of doped organic semiconductors. *Phys. Rev. Lett.* **102**, 0966021-0966024 (2009).

15 Brown, C. T., Seshadri, V., Mathai, M., Woodworth, B. & Laird, D. 32.1: Invited paper: Plexcore® OC for HIL applications in OLED lighting and display. *SID Symp. Digest Tech. Pap.* **41**, 461-464 (2010).

16 Mauger, S. A. & Moulé, A. J. Characterization of new transparent organic electrode materials. *Org. Electron.* **12**, 1948-1956 (2011).

17 de Jong, M. P., van IJzendoorn, L. J. & de Voigt, M. J. A. Stability of the interface between indium-tin-oxide and poly(3,4-ethylenedioxythiophene)/poly(styrenesulfonate) in polymer light-emitting diodes. *Appl. Phys. Letts.* **77**, 2255 (2000).

18 Still, R. H. & Whitehead, A. Thermal degradation of polymers. XVI. Thermal analysis studies on poly(p-methoxystyrene) and poly(p-hydroxystyrene) in air and nitrogen *J. Appl. Polym. Sci.* **21**, 1215-1225 (1977).

19 Jiang, D. D., Yao, Q., McKinney, M. A. & Wilkie, C. A. FTIR studies on the thermal degradation of some polymeric sulfonic and phosphonic acids and their sodium salts. *Polym. Degrad. Stability* **63**, 423-434 (1999).

20 Reddy, M. & Marinsky, J. A. A further investigation of the osmotic properties of hydrogen and sodium polystyrenesulfonates. *J. Phys. Chem* **74**, 3884-3891 (1970).

21 Zhuo, J. M. *et al.* Direct spectroscopic evidence for a photodoping mechanism in polythiophene and poly(bithiophene-alt-thienothiophene) organic semiconductor thin films involving oxygen and sorbed moisture. *Adv. Mater.* **21**, 4747-4752 (2009).

22 Garreau, S., Louarn, G., Buisson, J. P., Froyer, G. & Lefrant, S. In situ spectroelectrochemical raman studies of poly(3,4-ethylenedioxythiophene) (PEDT). *Macromolecules* **32**, 6807-6812 (1999).

23 Zotti, G. *et al.* Electrochemical and XPS studies toward the role of monomeric and polymeric sulfonate counterions in the synthesis, composition, and properties of poly(3,4-ethylenedioxythiophene). *Macromolecules* **36**, 3337-3344 (2003).

24 Randin, J. P. Ion-containing polymers as semisolid electrolytes in WO_3-based electrochromic devices. *J. Electrochem. Soc.* **129**, 1215-1220 (1982).

25 Bozkurt, A. Anhydrous proton conductive polystyrene sulfonic acid membranes. *Turk. J. Chem.* **29**, 117-123 (2005).

26 Nagamani, C. *et al.* Importance of dynamic hydrogen bonds and reorientation barriers in proton transport. *Chem. Commun.* **47**, 6638-6640 (2011).

27 Colthup, N. B., Daly, L. H. & Wiberley, S. E. *Introduction to infrared and Raman spectroscopy*. (Academic Press, Inc, 1990).

28 AIST RIO-DB spectral database for organic compounds. Natl. Inst. Adv. Ind. Sci. Technol., Japan.

Chapter 3.

On the Nature and Injection Characteristics of Perfluorinated Ionomer-Modified Hole-Injection Layers

In this chapter, I describe our work in understanding the nature of the surfaces of p-doped conducting-polymer films of poly(3,4-ethylenedioxythiophene): poly(styrenesulfonic acid) (PEDT:PSSH) blended with Nafion® oligomers, i.e., 2-(2-sulfonatotetrafluoroethoxy)tetrafluoro-ethoxyfunctionalized oligotetrafluoroethylene, also called perfluorinated ionomers (PFIs), which are previously known to increase workfunction to *ca*. 5.6 eV and proposed to give improved hole injection into the adjacent semiconductor layer. However, we show here that despite their ultrahigh workfunctions, they do not provide sufficiently fast hole transfer rate to an adjacent semiconductor. Thus they are not able to furnish ohmic contacts to polymer organic semiconductors with ionization potentials deeper than ca. 5.2 eV. This is a consequence of the molecular segregation of a perfluoroalkyl monolayer at the surface of the hole-injection layer (HIL) that sets up the surface dipole providing the ultrahigh workfunction but shields the p-doped PEDT segments from the adjacent semiconductor. X-ray and ultraviolet photoemission spectroscopies confirm that the increase in workfunction arises from this surface dipole rather than a relative shift of the Fermi level within the partially-occupied electronic band. Electroabsorption spectroscopy confirms the hole density at the semiconductor interface can only be weakly modulated, and hence hole transfer rate is low. Therefore an electrode that has a large workfunction generated by an insulating dipolar surface layer cannot in general provide ohmic contacts in devices.

3.1 Introduction

Fundamentally, an ohmic injection contact is one that furnishes a sufficiently large carrier density at the semiconductor side of the contact so that the effective interfacial resistance is minimal and ohmic (i.e., current proportional to electric field). Achieving ohmic contacts is key to maximizing the power efficiency of semiconductor devices and improving their operational stability. Ohmic contacts are required for light-emitting diodes, field-effect transistors and solar cells fabricated from both conventional inorganic semiconductors and the more recently developed organic semiconductors (OSCs). However, the characteristics and conditions for ohmic contacts in OSC devices are still being investigated.[1-3] The presence at the contact of an interfacial layer of mobile carriers, which we call a δ-doped layer, has been directly measured in the sub-bandgap region by electromodulated absorption (EA) spectroscopy, and a threshold density of this layer ($\approx$ few 10^{11} cm^{-2}) is required for ohmic contacts.[4,5]

A well-known way to achieve ohmic hole contacts is to use electrodes with large workfunctions. How large a workfunction ϕ is required has not been fully established, but a rule-of-thumb is for ϕ to be near to or larger than the conventional ionisation potential I_p of the semiconductor, which lies well beyond the pinned Fermi level measured in ultraviolet photoemission spectroscopy. This criterion receives support from device studies using PEDT:PSSM electrodes with variable workfunctions.[4,6] However, this should not be a sufficient condition, and perhaps may not even be a necessary condition.[7] The contact should also provide a sufficiently fast hole injection to maintain the carrier density required for space-charge-limited current flow, as stipulated in the fundamental definition of an ohmic contact. However, this aspect has often been neglected in the

literature. In this work, we wish to illuminate this requirement using PEDT: PSSH and PEDT: PSSH: PFI electrodes as models.

The current industry effort to migrate towards deeper-I_p OSCs for better stability and easier electron injection makes it a pressing goal to develop new solution-processable *p*-doped semiconductors with workfunctions deeper than *ca*. 5.2 eV to provide efficient HILs into these OSCs. Recently, it was reported that PFIs (chemical structure in Fig. 3.1)[8] can be blended into the well-established HILs, such as PEDT: PSSH[9,10] and sulfonated poly(thiophene-3-[2-(2-methoxyethoxy)ethoxy]-2,5-diyl): poly(4-hydroxystyrene) (S-P3MEET:PHOST)[11,12] to give significantly larger workfunctions. The ϕ of the resultant PFI-modified HILs increase from 5.0−5.2 eV to 5.6−5.7 eV.[13-17] An improvement in the current density−voltage (*JV*) characteristics of some test diodes has been reported.[14-17] However, little is known about the surface composition and electronic properties of these PFI-modified blends, other than they are surface-enriched with PFI, which appears responsible in some ways to generate the large workfunction.[14,15] Curiously, the reported improvement has been modest,[14-17] far short of the expected performance of an ultrahigh workfunction HIL, such as one which we have generated by strong *p*-doping of the deep-I_p semiconductor.[7] In addition, an electron-blocking mechanism may have contributed to or even dominated the characteristics of double-carrier diodes used in those reports, analogous to that observed when monolayer semiconducting or insulating films are assembled at the hole-injection contact.[18,19]

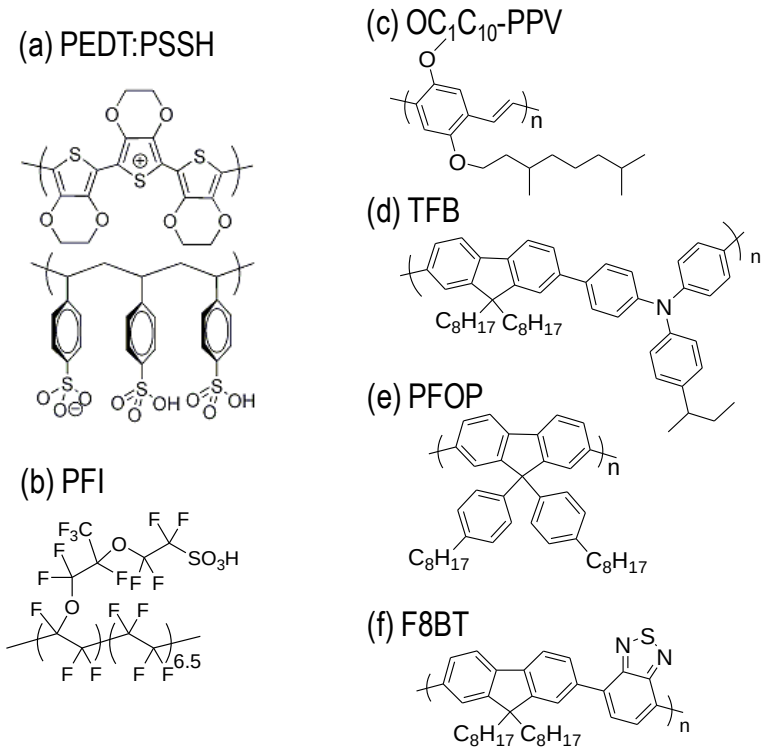

Figure 3.1. Chemical structures of materials used in this study. (a) PEDT:PSSH, (b) PFI, (c) OC1C10-PPV, (d) TFB, (e) PFOP, (f) F8BT.

In this chapter, we therefore wish to clarify these two central puzzles of PFI-modified HILs – the origin of their increased workfunction, and the prospect for making ohmic contacts with this approach. We studied the PFI-modified PEDT: PSSH system. One may consider this an important model of the approach to create ultrahigh workfunction electrodes using a dipolar dielectric surface layer. The insights gained may thus be relevant to other related approaches using dipolar dielectric self-assembled monolayers,[20-22] and self-assembled dielectric polyelectrolytes and amine-functionalized dielectric polymers.[23]

We show here that the ultrahigh workfunction in PEDT: PSSH: PFI is generated by an interfacial vacuum level shift associated with the frontier monolayer of the film surface. This downshifts the

Fermi level E_F of the electrode relative to the highest-occupied-molecular-orbital (HOMO) band edge of the adjacent semiconductor, without greatly increasing the rate of hole transfer. As a consequence, while these ultrahigh-workfunction HILs are eminently suitable for energy-level alignment studies that probe the thermodynamic equilibrium limit, they are inadequate in providing the required kinetic charge-transfer rates to provide an ohmic contact to deep-I_p polymers. Charge-transfer rate refers to the rate at which charges are supplied from the contacts to the adjacent semiconductor. This rate has to be sufficiently fast to maintain the contact carrier density and must equal the current passing through the film by the current continuity equation. For a typical current density of 100 $mAcm^{-2}$, the charge transfer rate required is 6×10^{17} charges $cm^{-2}s^{-1}$. The modified HILs could not provide anything remotely close to this rate. As a result, PEDT: PSSH: PFI performs only a little better than PEDT: PSSH to provide hole-dominated currents into a range of OSCs.

3.2 Experimental Methods

3.2.1 Materials

PEDT:PSSH was obtained from HC Starck (Baytron P, Leverkussen, Germany; now Clevios P VP Al 4083, from Heraeus Precious Metals GmbH) as a 1: 6 w/w (weight/ weight) material corresponding to 14 vol% PEDT dispersed in 86 vol% PSSH. PSSH (Mw = 70k) was obtained from Scientific Polymer Products (N.Y.) and dissolved in Millipore water. PFI was obtained from Sigma Aldrich (Nafion® perfluorinated resin solution) as a 5 w% dispersion in a mixed solvent of 45 vol% water and 55 vol% lower aliphatic alcohols. The equivalent weight is 1100.

3.2.2 Ultraviolet photoemission spectroscopy

50-nm thick HIL films were spin-cast on Au-coated Si substrates and baked at 140°C (hotplate) in the N_2 glovebox (pH2O, pO2 < 1ppm). Valence band spectra were collected using He I radiation (21.21 eV) on an ESCALAB MkII spectrometer with the electron analyzer operated at constant pass energy of 5 eV to give a spectral resolution of 50 meV. The base pressure was ~ 10^{-9} mbar. The photoemission angle was set at θ=90°, and a standard sample bias of –10.00 V was applied to collect all the photoelectrons. The Fermi level kinetic energy $E_{k,Ef}$ was established from the Fermi step observed on a reference Ag foil. The work function φ was extracted from the low-energy cutoff $E_{k,LECO}$: $\varphi = E_{k,LECO} + 21.21 – E_{k,Ef}$.

3.2.3 X-ray photoemission spectroscopy

X-ray photoelectron spectroscopy (XPS) was performed on the same films as the UPS, after UPS, using MgKα X-ray (1253.6 eV), respectively, on VG ESCALab Mk-II spectrometer, at 30° and 90° acceptance angles (with respect to the analyzer). All spectra have been corrected using linear

backgrounds. The integration of these spectra after correction with the empirical sensitivity factors provides the atomic stoichiometry determined by XPS. Quantification error is expected to be ±10%.

3.2.4 Device fabrication and characterisation

Hole-dominated devices were fabricated by spin coating HIL solutions, in ambient, on standard clean 1 (SC1) cleaned ITO substrates to attain 50 nm film. The solutions were pre-filtered through a 0.45-μm nylon syringe filters. The films were annealed at 140°C (hotplate) in glovebox. 10 mg/mL OC_1C_{10}-PPV, 15 mg/mL TFB and 15 mg/mL PFOP solutions in toluene were prepared from polymers obtained from Cambridge Display Technology. The polymer OSC films were spin-coated over the HILs in the glovebox to give 120 nm-thick films and annealed at 120°C (hotplate) in glovebox. 120-nm-thick aluminum film was then thermally evaporated through a shadow mask at a base pressure of 10^{-7} Torr to give the cathode for eight 4.3 mm^2 pixels on each substrate. The current-voltage characteristics were collected on a probe station in the glovebox using a Keithley 4200 semiconductor parameter analyser. Film thicknesses were measured by a profilometer (Tencor P2).

3.2.5 Contact angle measurement

Static and dynamic (advancing and receding) contact angles of various probe liquids on different surfaces were measured by sessile drop shape analyzer (FTA1000; First Ten Angstroms) at room temperature (22°C). The HILs and the PFI films were annealed at 140°C (hotplate) for 10 min in glovebox before the contact angle measurements. The PTFE substrate was cleaned by standard clean 1 (SC1). The surface tension of the probe liquids was determined by the pendant drop method. The probe liquid was pumped at a rate of 0.6 $\mu L\ s^{-1}$ for the dynamic measurements.

3.2.6 Electromodulated absorption spectroscopy

Electroabsorption spectroscopy (EA) is a technique used to determine the built in potential, V_{bi}, in devices.[24-26] It makes use of the dependence of a material's light absorption on frequency of light and the electric field inside the material. The sample is generally isolated in vacuum and put to low temperatures (~30 K). It has been demonstrated that even though the V_{bi} is temperature independent, measuring at low temperatures where the bulk charge density is very low is advantageous.[27] A DC bias with an additional modulation is applied and the absorption of reflected light from the device is measured for a range of monochromatized light. The V_{bi} in devices is caused by the difference in work function of the opposite electrodes. This built in electric field can be cancelled by applying a DC bias which is equal to the difference in work function of the two metals.

EA makes use of the Stark effect, the splitting of electronic energy levels in an electric field. It is analogous to the Zeeman effect, which refers to the splitting of energy levels by the application of a magnetic field. The splitting of the energy levels brings about a change in the absorption and hence the absorption coefficient, α, of the material. The change in intensity of light absorbed by a material of thickness d is related to the change in absorption coefficient by the following equation, as derived from the Lambert-Beer law:

$$\frac{\Delta I}{I} = -d\Delta\alpha$$

How the applied bias affects the light absorption is described in the following. The applied electric field is induces a polarization **P** in the material according to the following equation where ε_0 is the permittivity of free space and χ is the susceptibility of the material.

$$\boldsymbol{P} = \varepsilon_0 \chi \boldsymbol{E}$$

Generally the susceptibility is nonlinear and is dependent on the applied electric field

$$\chi = \chi^1 + \chi^{(2)} \cdot E + \chi^{(3)} \cdot E^2$$

$X^{(3)}$ is the lowest order nonlinear susceptibility since the second order terms cancel each other out as:

$$P^{(2)} = \varepsilon_0 \, \chi^{(2)} \, (+E)^2 \quad , \quad -P^{(2)} = \varepsilon_0 \, \chi^{(2)} \, (-E)^2$$

The complex dielectric constant of the material is defined as

$$\varepsilon = 1 + \chi$$

$$\varepsilon = \varepsilon_1 + i\varepsilon_2 = (n + i\kappa)^2$$

Where n is the refractive index of the material and κ is the imaginary refractive index. The imaginary part of the dielectric constant is related with the absorption coefficient with the following equation:

$$\varepsilon_2 = 2n\kappa = \frac{nc}{\omega}\alpha(E)$$

Where c is the speed of light and ω is the frequency of the light. Hence, the change in intensity of the light absorbed is proportional to the imaginary part of third order susceptibility.

$$\frac{\Delta I}{I} \propto Im\chi^{(3)} \cdot E^2$$

For an applied voltage V with AC modulation given as the following:

$$V = V_{DC} - V_{bi} + V_{AC} \cdot \sin(\omega t)$$

The change in absorbance is given as follows

$$\frac{\Delta I}{I} \propto Im\chi^{(3)} \cdot (V_{DC} - V_{bi} + V_{AC} \cdot \sin(\omega t))^2$$

Hence the change in absorbance is related to the fundamental and the second harmonic frequencies by the following:

$$\frac{\Delta I}{I}(\omega) \propto (V_{DC} - V_{bi}) \cdot V_{AC} \cdot \sin(\omega t)$$

$$\frac{\Delta I}{I}(2\omega) \propto V_{AC}^2 \cdot \cos(2\omega t)$$

Therefore, when the applied DC bias is the same as the built-in voltage V_{bi}, the change in absorbance at the fundamental harmonic frequency becomes zero.

In this chapter, EA measurements of the diodes were performed at 30 K in a closed-cycle He cryostat (Janis APD HC-2). The pressure inside the chamber was maintained at 10^{-6} mbar. A sinusoidal drive voltage superposed on the selected DC bias was injected into the diode. Monochromatic light was incident through the glass substrate at 45°, and its reflection of the cathode collected by mirror optics onto a photodiode. The voltage output was demodulated by a lock-in amplifier phase locked to the AC to give the change in absorbance for a range of wavelength.

3.2.7 Current−voltage (*JV*) characteristics simulation

The JV characteristics were simulated using standard diffusion−drift equations assuming a hole-dominated current, a diffusion slope $\frac{\partial \ln J}{\partial V} = \frac{\mathrm{e}}{nkT}$, with *n* = 2, and a contact carrier density of 2 x 10^{17} cm^{-3}. The integrated contact carrier density is *ca*. 1 x 10^{11} cm^{-2}, as suggested experimentally.[4,5]

3.3 Results and Discussions

3.3.1 High work function of PEDT:PSSH:PFI films due to dipole layer

Figure 3.1 shows the chemical structures of the materials used in this work. The commercial solution of PEDT: PSSH comprises *p*-doped PEDT chains dispersed together with poly(styrenesulfonic acid)[9] that often contains metallic ion and other impurities. In this work, PEDT: PSSH and PSSH solutions were purified by dialysis with semiconductor-grade hydrochloric acid (0.1 M) followed by Millipore water.[28] This step is important to remove free ions, and sulfuric acid generated by PSSH desulfonation, eliminating these impurities from the final films. PEDT: PSSH solutions with different volume fractions of PEDT and PSSH were prepared by diluting the purified PEDT: PSSH solution with the purified PSSH solution to give formulations containing 8 and 12 vol% PEDT with balance made of PSSH. These compositions were known to give optimal organic light-emitting diode performances. PEDT: PSSH: PFI formulations containing identical 8 and 12 vol% PEDT were prepared by mixing the purified PEDT: PSSH solution with the PFI dispersion. We used vol% to label these formulations as this is the most important parameter that determines composition and percolation. Four formulations were prepared: PEDT-12S, PEDT-8S, PEDT-12F and PEDT-8F, where the number gives the PEDT vol%, "S" denotes the unmodified formulation (i.e., PEDT: PSSH) and "F" denotes the PFI-modified formulation (i.e., PEDT: PSSH: PFI). Table 1 gives the detailed compositions of these formulations. All formulations have PSSH, a good film-former, as the majority component. PFI tends to aggregate. Films were then spin-cast and baked in the N_2-filled glovebox (hotplate 140ºC, 15 min).

Table 1. Compositions of HILs used in this study.

HIL	weight fraction[a]			volume fraction[b]		
	PEDT	PSSH	PFI	PEDT	PSSH	PFI
PEDT-12S	0.12	0.88	0.00	0.12	0.88	0.00
PEDT-8S	0.08	0.92	0.00	0.08	0.92	0.00
PEDT-12F	0.11	0.65	0.24	0.12	0.72	0.16
PEDT-8F	0.06	0.37	0.56	0.08	0.48	0.44

We first show that the high workfunction in the PFI-modified films derives from a surface dipole effect rather than an electrochemical potential shift of the E_F. Figure 3.2a shows the valence band (VB) spectra of the four HILs measured by ultraviolet photoemission spectroscopy (UPS) with He I excitation, referenced to the vacuum level E_{vac}. The PEDT sulfur lone pair (S3p) and phenyl-ring molecular orbital (MO) emission of the PSSH overlap at −8.5 eV,[29] while CF bonds contribute no MO features to the displayed region. This band is suppressed in the PFI-modified films, suggesting that the PSSH component is depleted at the film surface where the UPS photoemission originates. The inelastic mean free path for photoelectrons excited by He I is very short, *ca*. 0.6 nm, and so the spectra are characteristic of the topmost or so monolayer of the surface. Figure 3.2b shows the expanded spectra for the E_F region. This region arises solely from photoemission of PEDT segments located at the surface of the films. ϕ is determined in the usual way from the photoelectron kinetic energy at the E_F (KE_{Ef}) and that at the low-energy cut-off (KE_{LECO}): $\phi = KE_{LECO} + h\nu - KE_{Ef}$, where $h\nu$ is the photon energy (21.21 eV).[30] The 8S and 12S HILs have ϕ = 5.1 eV and 5.2 eV respectively, while both 12F and 8F HILs have ϕ = 5.6 eV, consistent with previous reports.[14,17,31] The workfunctions of PEDT: PSSH: PFI films are thus not dependent on the PFI ratio over this composition range. These spectra reveal that the PEDT density-of-states (DOS) extend up to E_F, as established previously for PEDT:PSSH,[29] characteristic of heavily *p*-

doped conducting polymers.[32] The lower intensity of PEDT spectra in the PFI-modified films suggests that the PEDT concentration in the topmost 0.6-nm of the surface is one-half to one-third of that of the unmodified films.

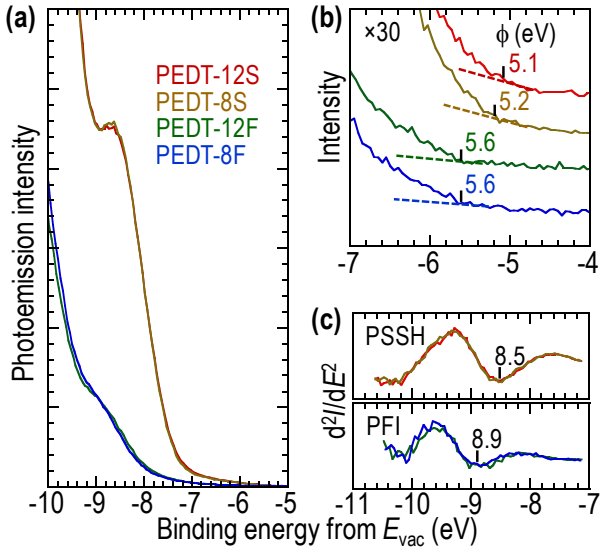

Figure 3.2. Ultraviolet photoemission spectroscopy of the hole-injection layers. (a) UPS spectra showing the valence band region. (b) Expanded UPS spectra for the Fermi edge region. (c) Second-derivative photoemission spectra showing the rigid shift in the molecular orbital energy on the vacuum energy scale. The spectra in (b) are offset and EF marked for clarity. Sample bias, −10.00 V. He I, 21.21 eV. Legend for all parts is as given in (a).

The workfunction in general is given by the sum of electrochemical and surface-dipole contributions, $\phi = \mu + \chi$, where μ is the electrochemical potential of the carriers at E_F (measured with respect to the Galvani potential) and χ is the surface-dipole potential. For the family of PEDT:PSSM (where M is spectator cation), it has been established that the dependence of ϕ on M arises solely from μ effects due to the ionic (Madelung) potential set up by the spectator cations and the sulfonate counter-anions.[29] We examined the situation here for the PFI-modified HILs. Figure 3.2c

shows the second derivatives of the VB spectra to accurately locate the position of the S/phenyl MO band. We found it lies at −8.5 eV in PEDT: PSSH and −8.9 eV in PEDT: PSSH: PFI, downshifted by 0.4 eV. The widths of second-derivative features indicate the bandwidths are identical. These together with the 0.4-eV downshift of the onset of PEDT photoemission (Fig. 3.2b) confirms that the PEDT and PSSH features in PEDT: PSSH: PFI are rigidly downshifted by 0.4 eV. This reveals the increase in ϕ arises entirely from a surface dipole effect. The origin of this dipole is attributed to oriented $-CF_2-$ segments present at the surface (negative end oriented outwards).

3.3.2 Surface enrichment of PFI

To further verify the composition profile in the surface region of these films, we collected core-level X-ray photoemission spectra at both 90° and 30° emission angles. Figure 3.3 shows the C1s, F1s, O1s and S2p core-level spectra plotted against binding energies (BE) referenced to E_F and collected at 90° (i.e., perpendicular emission).

First, there is no shift in the binding energy of each component, referenced to E_F, across the films despite the 0.4-eV change in workfunction. The C1s peaks from PEDT and PSSH appear together at 284.0 eV, while that from PFI at 291.0 eV. The F1s peak from PFI appears at 688.2 eV. The O1s peaks from PEDT and PSSH appear together at 531.4 eV, while that from PFI at 534.7 eV. The S2p peak from PEDT appears at 163.6 eV, and from sulfonic acid (both PSSH and PFI) at 168.0 eV.[33] This provides independent confirmation that the rigid bandshift observed in the VB region also applies to the core levels. This further confirms the increase in ϕ arises from a surface dipole that upshifts E_{vac}, rather than an increase in μ which would decrease the binding energies of all electronic bands measured with respect to E_F.

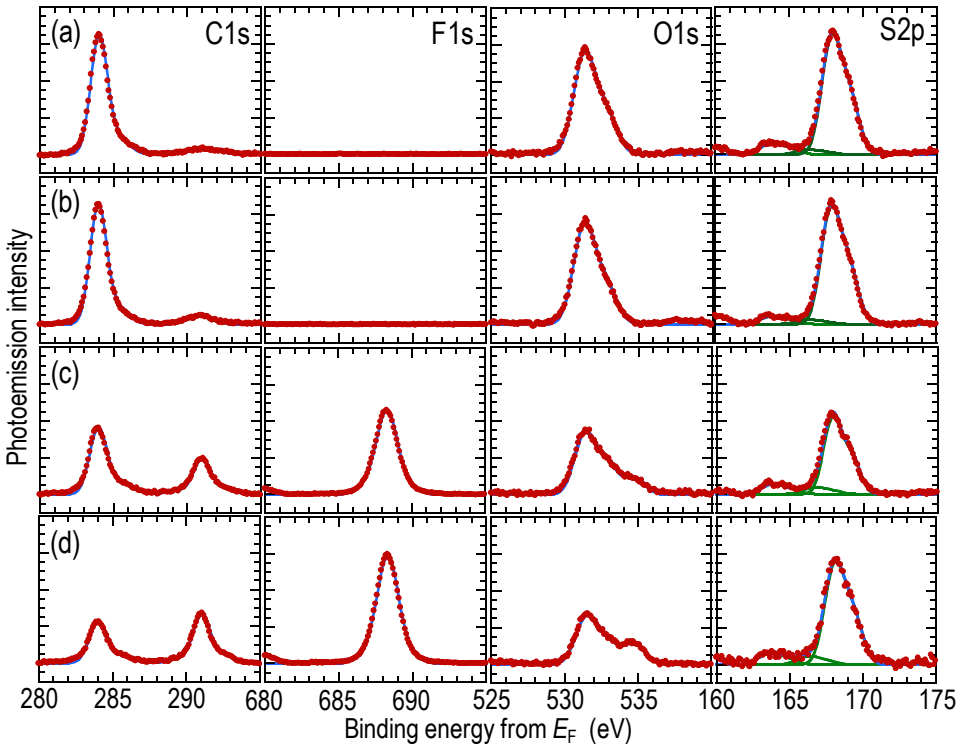

Figure 3.3. X-ray photoemission spectroscopy of the hole-injection layers. (a) PEDT-12S, (b) PEDT-8S, (c) PEDT-12F and (d) PEDT-8F. Photoemission angle, 90º. Curve-fitting is shown for S2p core level.

Second, the combined C1s emission from PEDT and PSSH in the PFI-modified films is less severely attenuated (only by half) than their VB emissions. This suggests a strong composition grading right at the surface. To quantify this effect, we evaluated the PEDT, PSS and PFI stoichiometries from the detected photoemission intensities to reconstruct their composition−depth profile assuming a simple monotonic decay from the surface. The $^1/_e$ effective escape depth is *ca*. 2.5 nm at 90° and *ca*. 1.2 nm at 30° for these core emissions. The *p*-doped PEDT contribution was resolved from the S2p spectra by curve-fitting using a known asymmetric shape-generating function with primary $S2p_{3/2}$ BE component at 163.6 eV[33]. The PSSH and PFI contributions were then evaluated from a self-consistent analysis of the sulfonate, fluorine, oxygen, hydrocarbon and fluorocarbon intensities, corrected with photo-ionization cross sections. The results are shown in

Figure 3.4 which plots the detected XPS volume compositions at the different electron escape depths. The escape depth corresponds also to the depth where the detected composition occurs in a linearly graded profile.

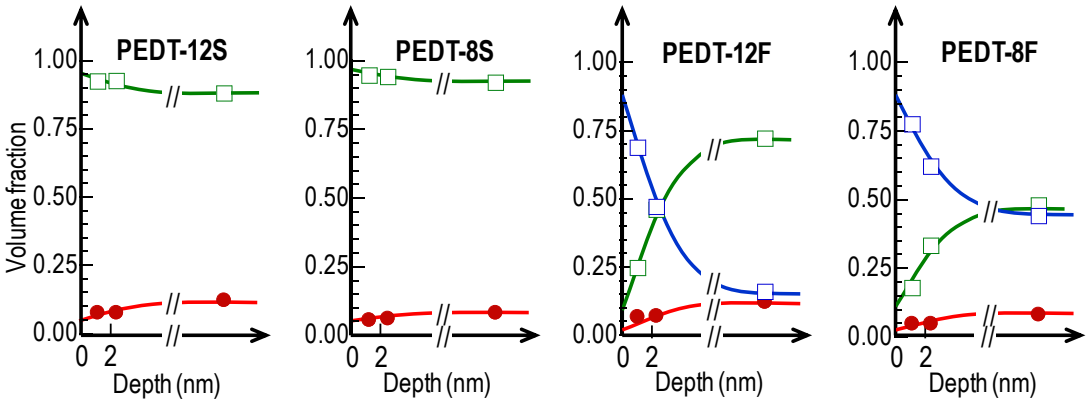

Figure 3.4. Surface composition profile models for the hole-injection layers. The XPS compositions are plotted at the corresponding electron escape depths, which are good approximations to the depths at which the compositions are detected for linear profiles. The bulk compositions are theoretical values computed from the experimental mixing ratio.

The PFI-modified films exhibit a marked surface enrichment of PFI at the expense of PSSH. This enrichment occurs deep into the sub-surface, leading to a composition inversion of the matrix polymer in the top 2 nm for the 12F film and top *ca*. 10 nm for the 8F film. For example, while the bulk of the 12F film comprises 12 vol% PEDT, 72 vol% PSSH and 16 vol% PFI (Table 1), the topmost 2.5 nm comprises on average 6.9 vol% PEDT, 45 vol% PSSH and 49 vol% PFI, while the topmost 1.2 nm comprises 6.5 vol% PEDT, 23 vol% PSSH and 70 vol% PFI. The deep PEDT composition profiles, however, are broadly identical between corresponding unmodified S and modified F films. Yet right at the surface itself, the PEDT in F films is locally depleted by a factor of 2−3 compared to the S films. Such details of the surface composition do not appear to have been

previously noted. The surface depletion of PEDT in the S films, however, is well-known from XPS[34] and neutron reflectivity[35,36] measurements, and has been shown to be reversible by PEDT electromigration.[33]

The results here show that in the PEDT: PSSH: PFI films, the frontier *p*-doped PEDT segments at the surface are overlaid by a perfluoroalkyl monolayer to a much greater extent than they are by PSSH monolayer in the unmodified films. Furthermore the deeper PEDT segments down to a few nm in the sub-surface of the PEDT: PSSH: PFI films are embedded in a PFI-rich rather than a PSSH-rich matrix. Since the HOMO (LUMO) of PFI is considerably deeper (shallower) than that of PSSH, one may expect the key consequence is a depression of the hole (electron) tunneling rate between the PEDT segments and any overlying semiconductor.

A question arises about possible differences in the morphology of the electrically-conducting PEDT segments in the surface and sub-surface of these films. The morphology of PEDT in PEDT: PSSH has been a matter of some controversy. Early studies were interpreted in support of a core-shell structure[37] but later work suggested a network morphology of the PEDT chains, consistent with the measured low conductivity percolation threshold and the layer-by-layer assembly to give ultrathin smooth PEDT: PSSH films.[19,38] Here there is no indication that PEDT adopts a different morphology in the PFI-modified films.

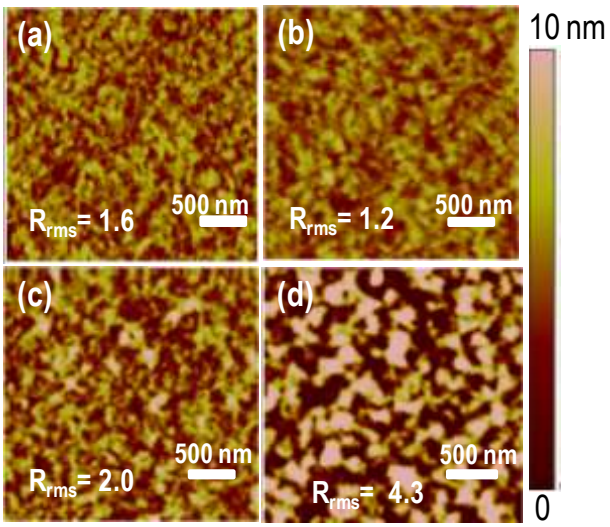

Figure 3.5. Atomic force microscopy images. (a) PEDT-12S, (b) PEDT-8S, (c) PEDT-12F and (d) PEDT-8F. Images were collected in the tapping mode. Root-mean-square roughness (Rrms) values are given in nm, averaged over the entire image. Film thickness, 50 nm. Substrate, indium-tin oxide glass. Solutions pre-filtered by 0.45-mm syringe filters.

Atomic force microscopy confirms the PFI are not precipitated out in separate phases (see Figure 3.5). All the HILs give nodular surface morphologies. The unmodified HILs show fine nodules in the 10-nm diameter range with a root-mean-square roughness (R_{rms}) of 1.2−1.6 nm, while the PFI-modified HILs show larger nodules of up to a few hundred nm in diameter and increasing R_{rms} with PFI ratio (R_{rms} = 2.0 nm for 12F, 4.3 nm for 8F). Nevertheless these films are much smoother than neat PFI films which show severe aggregation of the colloidal PFI particles which are not well solvated in aqueous alcohols.[8] The smooth ternary blend films obtained suggest PSSH helps to disperse and compatibilize the PFI with the solvent, suppressing phase segregation beyond the molecular length scale. Nevertheless, there is a surface energy difference between the modified and unmodified HILs as suggested by dynamic contact angles with aromatic and aliphatic hydrocarbon solvents which showed higher contact angles on the modified HILs compared to the unmodified ones (see Table 2).

Table 2. Liquid probe advancing (a) and receding (r) angles on the different surfaces.

	p-xylene		dichlorobenzene		decane	
	θ_a(°)	θ_r(°)	θ_a(°)	θ_r(°)	θ_a(°)	θ_r(°)
PEDT12S	5	5	6	6	6	6
PEDT12F	55	38	69	60	45	31
PFI	56	25	64	50	43	21
PTFE	56	23	66	39	40	9

3.3.3 Energy-level alignment and device performance

We next deduced the *in-situ* diode energy-level alignment of these HILs in contact with a set of model polymer OSCs with different I_p values (UPS): poly(9,9-bis(4-octylphenyl)fluorene-3,6-diyl) (PFOP) (deep-I_p, 5.8 eV); poly(9,9'-dioctylfluorene-2,7-diyl-1,4-phenylene-N-(*p*-sec-butylphenyl)amino-1,4-phenylene) (TFB) (medium-I_p, 5.5 eV); and 2,5-dialkoxy-substitued poly(*p*-phenylenevinylene) (OC_1C_{10}-PPV) (shallow-I_p, 5.1 eV) (chemical structures in Fig. 3.1), and related these to the measured and simulated diode *JV* characteristics. These polymers are amorphous or nanocrystalline and thus their film morphologies are not sensitive to differences in the surface energies of the various HILs. To do this, we first used electromodulated absorption (EA) spectroscopy to measure the diode built-in potential V_{bi},[39,40] and deduced the flatband energy-level diagrams.[5] The V_{bi} is obtained as the applied dc bias V_{dc} required to null out the quadratic EA Stark effect spectrum.[41,42] We performed these measurements at 30 K to avoid bulk injection and attendant spectral complications.[5] The V_{bi} is also given theoretically by the difference in effective workfunctions of the contacts, $V_{bi} = \phi_{el2} - \phi_{el1}$, where ϕ_{el2} and ϕ_{el1} are the effective workfunctions of the respective electrodes ($\phi_{el2} > \phi_{el1}$).[5] Thus if the effective workfunction of one of the contacts is known *a priori*, the effective workfunction of the other contact can be deduced. Furthermore, the V_{bi} can be considered to comprise two terms: the sum of electrostatic band-bending in the vicinity of the contacts arising from the thermal carrier diffusion tail, and what we call the bare potential

which is the hypothetical difference between the electrode E_Fs relative to E_{vac} in the OSC at flatband in the absence of electrostatic band-bending.[43] The electrostatic band bending term can be computed by standard diffusion-drift equations which give also the *JV* characteristics of the diodes.[44] The electron contact in these diodes was chosen to be Al to give hole-dominated devices. Although Al is not fully electron-blocking, the injected electron current appears to be small and does not degrade our conclusions.

The effective workfunctions of the electrode incorporate the effects of the adjoining semiconductor: electrostatic band bending in the semiconductor in the vicinity of the contact, and vacuum-level offset at the interface due to charge shift or transfer.[5] For buried metal contacts evaporated on polymer semiconductors, we obtained effective workfunctions that are surprisingly robust and transferrable across different polymer OSCs in the unpinned regime.[5] For Al, this is 3.4 ± 0.1 eV. Since the lowest unoccupied MO edges of PFOP, TFB and OC_1C_{10}-PPV are all considerably higher than 3.4 eV, the electron contacts here are unpinned, and ϕ_1 = 3.4 eV is taken as the reference for all energy-level diagrams.

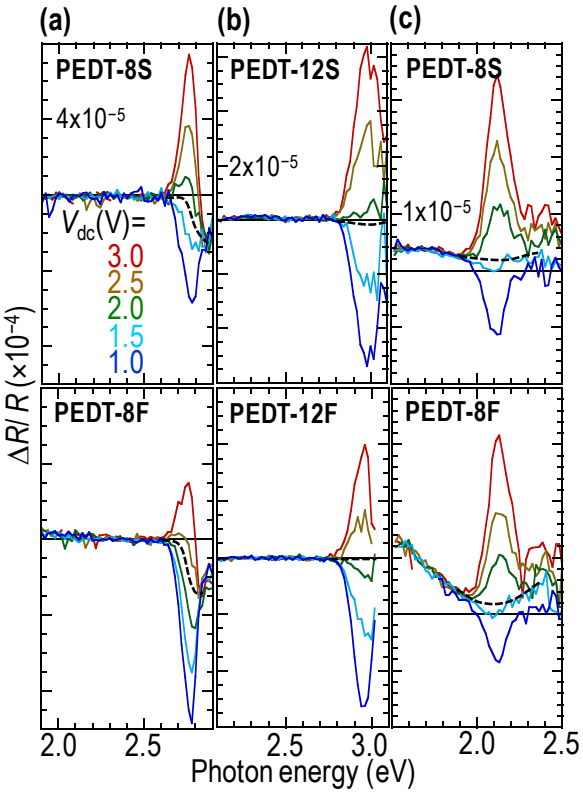

Figure 3.6. Electromodulated absorption spectra for the hole-dominated diodes with different HILs. (a) PFOP, (b) TFB and (c) OC_1C_{10}-PPV. Value for first major tick in each panel column is indicated. Positive value indicates induced absorption in-phase with forward bias half-cycle. Cathode, Al. Temperature, 30 K. Modulation frequency, 535 Hz. Horizontal line, zero. Dashed line, estimated null spectrum. Actual HIL used is as indicated.

Figure 3.6 shows the normalized modulated reflectance spectra $\Delta R / R$, where ΔR is the root-mean-square reflectance in-phase with the forward-bias half-cycle, and R is the dc reflectance. Figure 3.7 shows the energy-level diagrams deduced for the diodes at 30 K (top) and the measured *JV* characteristics at 298 K (bottom). The EA $\Delta R / R$ spectra for PEDT-*x*/ PFOP/ Al diodes, where x = 8S and 8F are shown in Figure 3.6a. The Stark peak occurs at 2.75 eV, near the π–π^* absorption edge of PFOP. PFOP does not exhibit the β-phase aggregation present in the usual poly(9,9-dioctylfluorene-3,6-diyl) and hence provides a suitable model of a non-trapping

deep-I_p polymer. The estimated "null spectrum" is shown as a dotted line regarded as background for the Stark effect spectrum. The Stark peak shows polarity inversion at 1.8 (±0.05) V for 8S, and 2.25 (±0.05) V for 8F. Hence, the effective workfunction of 8S is ϕ_{el} = (3.4 + 1.8) eV = 5.2 eV, and 8F is (3.4 + 2.25) eV = 5.65 eV, in excellent agreement with the measured vacuum workfunctions (± 0.05 eV). Therefore, the effective workfunctions of these HILs in contact with PFOP in the diode is the same as against vacuum. This means the vacuum levels at the contact are aligned. There is no significant dipole at the HIL/ OSC interface that alters its effective workfunction.

The energy-level diagrams are shown in Figure 3.7a. Since the E_{vac} offset is negligible (< 0.1 eV, Fig. 3.7a, top panel), there is also little or no δ-hole density at the PFOP interfaces to both these types of HILs. This is further confirmed by the weak or absent subgap polaron absorption in EA. Despite the more favorable effective workfunction of the PFI-modified HIL and low apparent thermodynamic hole barrier, $\Delta_h = I_p - \phi_{el2}$ = 0.15 eV, the hole density at the contact is small and insufficient to drive the contact ohmic. The *JV* characteristics for 8S, 12F and 8F HILs (Fig. 3.7a, bottom panel) are practically identical. The simulated *JV* characteristic for a hypothetical ohmic hole contact with the bare potential set to a realistic value (2.3 V) and an assumed constant space-charge-limited mobility $\mu_{SCLC} = 2 \times 10^{-4}$ cm^2 V^{-1} s^{-1} is shown by the grey curve. The experimental curves show a large upshift of *ca*. 1 V in the turn-on characteristics, which indicates the hole contacts are initially limiting. Above *ca*. 5 V, the contacts approach ohmic behavior for both types of HILs. Thus despite the more favorable energy-level alignment, the PFI-modified HIL does not offer a sufficiently large contact δ-carrier density[4,5] to reach ohmic behavior.

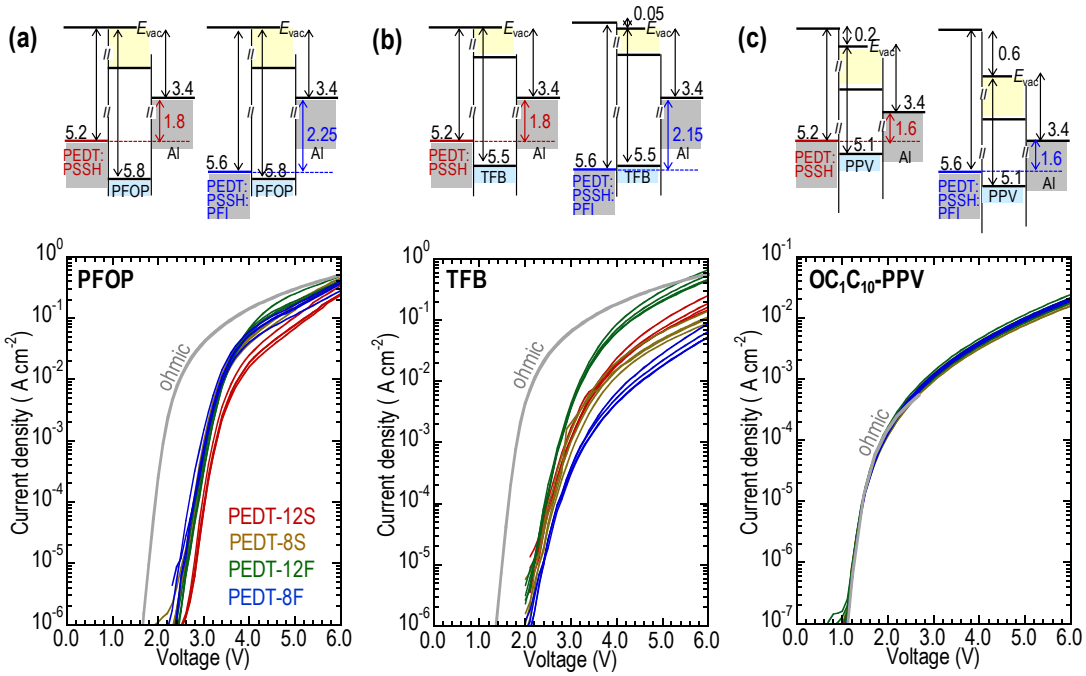

Figure 3.7. Energy-level alignment diagrams and JV characteristics of diodes with the different HILs. (a) PFOP, (b) TFB and (c) OC1C10-PPV. Four representative characteristics are shown for each type of diodes. JV characteristics are for second sweep. Grey lines show the simulated ohmic JV characteristics, with parameters given in the text.

The EA spectra for PEDT-*x*/ OC_1C_{10}-PPV/ Al diodes, where *x* = 8S and 8F are shown in Figure 3.6c. OC_1C_{10}-PPV provides an important model to probe the behavior of these contacts with a low-I_p OSC. The Stark peak occurs at 2.1 eV, near the OC_1C_{10}-PPV absorption edge. This peak shows polarity inversion at 1.6 (±0.05) V in both cases. Hence, the E_F for both HILs are now pinned identically at 5.0 eV *vs* E_{vac} of OC_1C_{10}-PPV, 0.1 eV above its HOMO edge (Fig. 3.7c, top panel). The marked reduction in effective workfunctions from the vacuum values indicates large E_{vac} offsets of 0.2 eV and 0.6 eV for pristine and PFI-modified HIL contacts respectively. The large attendant δ-hole densities are evidenced also by strong modulated subgap absorptions[4] in the EA spectra below 2.0 eV (Fig. 3.6c). The δ-hole density is likely to be larger at the PFI-modified HIL

contact, despite its slightly smaller interfacial capacitance since the conductive PEDT segments are embedded in a lower dielectric constant PFI matrix and further away from the interface. Since the higher hole density leads to stronger electrostatic band bending, the E_F must be pinned closer to the OSC HOMO edge for the PFI-modified HIL contact than the PEDT: PSSH contact. The shift of E_F pinning to deeper energies is attributed to reduction of polarization energy of the polaron at the PFI-modified HIL contact.[45-47] The simulated ohmic *JV* characteristics are shown in grey in Figure 3.7c for a bare potential of 1.6 V, and constant μ_{SCLC} = 1.5 x 10 $cm^2\ V^{-1}\ s^{-1}$.[48] The measured *JV* characteristics of these diodes closely follow this simulation up to 3 V, beyond which the density dependence of μ_{SCLC}[49] needs to be considered. The remarkable agreement confirms that both types of HILs form ohmic hole contacts with OC_1C_{10}-PPV, as may be expected. Hence, the currents are space-charge limited and the additional δ-hole density provided by the PFI-modified HIL does not provide a larger current.

The situation for the case of an intermediate-I_p OSC is given by TFB, which is expected to be most sensitive to any improvement in hole-injection efficiency. The EA spectra for PEDT-*x*/ TFB/ Al diodes, where *x* = 12S and 12F are shown in Figure 3.6b. The Stark peak occurs at 2.95 eV, near the TFB absorption edge. The PEDT: PSSH/ TFB contact resides near the blocking−ohmic borderline regime for hole injection and appears to be somewhat variable.[6,33] The Stark peak shows polarity inversion at 1.8 (±0.05) V for 12S, and 2.15 (±0.05) V for 12F. Hence, the effective workfunctions of 12S and 12F in these diodes are 5.2 and 5.55 eV respectively at 30 K. The effective workfunction of 12S is again identical to its vacuum workfunction, indicating vacuum level alignment at the contact with TFB. The effective workfunction of 12F is only 0.05 eV smaller than its vacuum workfunction, indicating incipient E_F pinning opening a E_{vac} offset of 0.05 eV (Fig. 3.7b,

top panel). This is surprising as it indicates that E_F of the PFI-modified HIL pins much closer to the HOMO edge of TFB than that of PEDT: PSSH.[6] Therefore, the PFI-modified HIL appears to be less effective in transferring holes into the adjacent semiconductor than the pristine HIL at the same hypothetical workfunction, probably a consequence of its lower interfacial capacitance. Previous experiments has suggested a threshold interfacial density of a few 10^{11} cm^{-2} is required for ohmic contacts.[4,5]

As a result, the PFI-modified HIL increases the hole current only modestly despite its favorable thermodynamic alignment with the HOMO edge of the semiconductor. The simulated ohmic *JV* characteristics are shown as a grey line in Figure 3.7b, for a bare potential of 2.0 V, and μ_{SCLC} = 2 x 10^{-4} cm^2 V^{-1} s^{-1}.[50] The experimental *JV* characteristics fall well below the simulated characteristic at low voltages, approaching it at high voltages, in particular for the 12F HIL.

Hence, it is clear from these results that workfunction alone is not a sufficient condition for ohmic contacts. The contact needs to be able to inject the required carrier density at the semiconductor interface to provide for ohmic behavior. This should come as no surprise, but has often been misunderstood in the literature. The PFI-modified HILs here produce a high workfunction favorable for hole injection, but this is generated through a dipolar dielectric layer. As a consequence, the contact resistance is high, and the equilibrium δ-hole density is low. The combined effect nearly completely mitigates the expected improvement in hole injection into a variety of model polymer OSCs. While the modified HILs may induce a different molecular packing of the OSC overlayer, a consistent picture has emerged from the three amorphous or nanocrystalline polymer OSCs tested that the dominant effect studied here is related to the energetics and kinetics of charge transfer.

Finally, we briefly outline what appears to be the situation in double-carrier OLEDs. An example for a model luminescent polymer OSC, poly(dioctylfluorene-*alt*-benzothiadiazole) (F8BT) (chemical structure in Fig. 3.1) (I_p = 5.9 eV), is given in Figure 3.8, where Ca is used as the electron-injecting cathode.

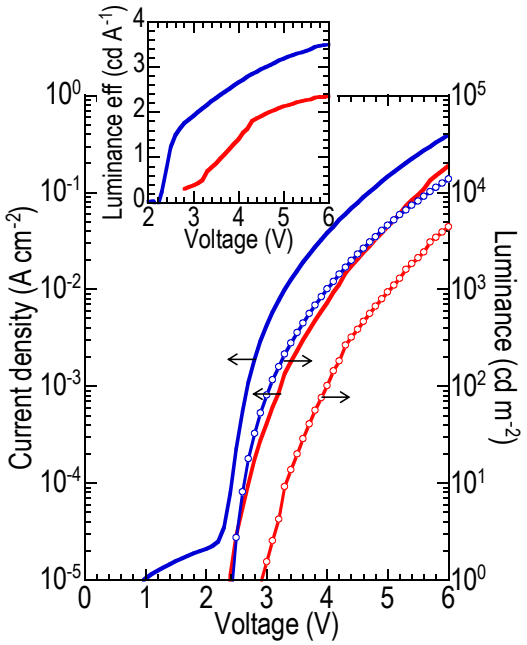

Figure 3.8. JVL characteristics of double-carrier light-emitting diodes with F8BT as light-emitting polymer. HIL = PEDT-8S (red), PEDT-8F (blue). Inset shows the voltage dependence of luminance efficiency. Emission spectrum center wavelength, 550 nm.

Although hole-dominated diodes do not show any clear evidence of enhancement of the current−voltage characteristics, similar to the situation in PFOP, the double-carrier diodes do give a significant enhancement in both *J* and the luminescence efficiency, i.e., recombination fraction, by an order of magnitude just above turn-on, decreasing to more modest values well above turn-on. This behaviour clearly indicates a considerably more efficient hole injection in the presence of the opposite carriers, which is very similar to that observed when an ultrathin self-assembled undoped PEDT−polyelectrolyte monolayer[19] or thin TFB layer[51] is used to block electron leakage and

improve hole injection into F8BT model diodes. Therefore, we consider that electron blocking contributes significantly to the improved characteristics of double-carrier diodes previously reported with PFI-modified HILs.

3.4 Conclusions

In summary, the ultrahigh workfunction of PEDT: PSSH: PFI blends is due to the development of a dipolar surface layer due to surface segregation of PFI chains. Despite the higher workfunction, the contact to deep ionization potential organic semiconductors remains far from ohmic due to the sluggish injection of holes at these contacts combined with the low equilibrium density there. As a result, the interface is unable to dynamically maintain the required carrier density for an ohmic contact. Thus, workfunction matching alone is not sufficient to ensure ohmic injection into the adjacent OSC. A more effective hole-injection (-extraction) layer would be one that imposes a large hole density at the semiconductor interface.

3.5 References

1 Malliaras, G. G. & Scott, J. C. The roles of injection and mobility in organic light emitting diodes. *J. Appl. Phys.* **83**, 5399-5403 (1998).

2 Shen, Y., Hosseini, A. R., Wong, M. H. & Malliaras, G. G. How to make ohmic contacts to organic semiconductors. *Chem. Phys. Chem.* **5**, 16-25 (2004).

3 Nicolai, H. T. *et al.* Space-charge-limited hole current in poly(9,9-dioctylfluorene) diodes. *Appl. Phys. Lett.* **96**, 172107 (2010).

4 Zhou, M. *et al.* The role of delta-doped interfaces for Ohmic contacts to organic semiconductors. *Phys. Rev. Lett.* **103**, 0366011-0366014 (2009).

5 Zhou, M. *et al.* Effective work functions for the evaporated metal/organic semiconductor contacts from in-situ diode flatband potential measurements. *Appl. Phys. Lett.* **101**, 013501 (2012).

6 Zhou, M. *et al.* Determination of the interface delta-hole density in a blue-emitting organic semiconductor diode by electromodulated absorption spectroscopy. *Appl. Phys. Lett.* **97**, 113505 (2010).

7 Sivaramakrishnan, S., Anto, B. T. & Ho, P. K. H. Optical modeling of the plasmon band of monolayer-protected nanometal clusters in pure and in polymer matrix thin films as a function of heat treatment. *Appl. Phys. Lett.* **94**, 091909 (2009).

8 Mauritz, K. A. & Moore, R. B. State of understanding of Nafion. *Chem. Rev.* **104**, 4535-4586 (2004).

9 Groenendaal, L. B., Jonas, F., Freitag, D., Pielartzik, H. & Reynolds, J. R. Poly(3,4-ethylenedioxythiophene) and Its derivatives: past, present, and future. *Adv. Mater.* **12**, 481-494 (2000).

10 Kirchmeyer, S. & Reuter, K. Scientific importance, properties and growing applications of poly(3,4-ethylenedioxythiophene). *J. Mater. Chem.* **15** (2005).

11 Brown, C. T., Seshadri, V., Mathai, M., Woodworth, B. & Laird, D. Invited Paper: Plexcore®OC for HIL Applications in OLED Lighting and Display. *SID Int Sym Dig Tec* **41**, 461-464 (2010).

12 Belaineh, D. *et al.* A high-performance *p*-doped conducting polymer blend based on sulfonated polyalkoxythiophene and poly (4-hydroxystyrene). *Chem. Mater.* **26**, 4724–4730 (2014).

13 Tengstedt, C. *et al.* Fermi-level pinning at conjugated polymer interfaces. *Appl. Phys. Lett.* **88**, 053502 (2006).

14 Lee, T. W. *et al.* Hole-injecting conducting-polymer compositions for highly efficient and stable organic light-emitting diodes. *Appl. Phys. Lett.* **87**, 231106 (2005).

15 Lee, T. W., Chung, Y., Kwon, O. & Park, J. J. Self-organized gradient hole injection to improve the performance of polymer electroluminescent devices. *Adv. Funct. Mater.* **17**, 390-396 (2007).

16 Park, J., Kwon, Y. & Lee, T. W. Layer-by-layer spin self-assembled hole injection layers containing a perfluorinated ionomer for efficient polymer light-emitting diodes. *Macromol. Rapid Commun.* **28**, 1366-1372 (2007).

17 Mauger, S. A. *et al.* High work-function hole transport layers by self assembly using a fluorinated additive. *J. Mater. Chem. C* **2**, 115-123 (2014).

18 Ho, P. K. H., Granström, M., Friend, R. H. & Greenham, N. C. Ultrathin self-assembled layers at the ITO interface to control charge injection and electroluminescence efficiency in polymer light-emitting diodes. *Adv. Mater.* **10**, 769-774 (1998).

19 Ho, P. K. H. *et al.* Molecular-scale interface engineering for polymer light-emitting diodes. *Nature* **404**, 481-484 (2000).

20 Sushko, M. L. & Shluger, A. L. Rough and fine tuning of metal work function via chemisorbed self-assembled monolayers. *Adv. Mater.* **21**, 1111-1114 (2009).

21 Osikowicz, W. *et al.* Transparent low-work-function indium tin oxide electrode obtained by molecular scale interface engineering. *Appl. Phys. Lett.* **85**, 1616 (2004).

22 Hotchkiss, P. J. *et al.* Modification of the surface properties of indium tin oxide with benzylphosphonic acids: A joint experimental and theoretical study. *Adv. Mater.* **21**, 4496-4501 (2009).

23 Zhou, Y. *et al.* A universal method to produce low–work function electrodes for organic electronics. *Science* **336**, 327-332 (2012).

24 Campbell, I. *et al.* Probing electronic state charging in organic electronic devices using electroabsorption spectroscopy. *Synthetic metals* **80**, 105-110 (1996).

25 Liess, M. *et al.* Electroabsorption spectroscopy of luminescent and nonluminescent π-conjugated polymers. *Physical Review B* **56**, 15712 (1997).

26 Brown, T. *et al.* Built-in field electroabsorption spectroscopy of polymer light-emitting diodes incorporating a doped poly (3, 4-ethylene dioxythiophene) hole injection layer. *Appl. Phys. Lett.* **75**, 1679-1681 (1999).

27 Zhou, M. *et al.* Effective work functions for the evaporated metal/organic semiconductor contacts from in-situ diode flatband potential measurements. *Appl. Phys. Lett.* **101**, 013501 (2012).

28 Chia, P. J. *et al.* Injection-induced de-doping in a conducting polymer during device operation: asymmetry in thoe hole injection and extraction rates. *Adv. Mater.* **19**, 4202-4207 (2007).

29 Chia, P. J. *et al.* Direct evidence for the role of the Madelung potential in determining the work function of doped organic semiconductors. *Phys. Rev. Lett.* **102**, 0966021-0966024 (2009).

30 Koch, N., Chan, C., Kahn, A. & Schwartz, J. Lack of thermodynamic equilibrium in conjugated organic molecular thin films. *Phys. Rev. B* **67**, 1953301-1953305 (2003).

31 Tang, J. X., Lee, C. S. & Lee, S. T. Electronic structures of organic/organic heterojunctions: from vacuum level alignment to Fermi level pinning. *J. Appl. Phys.* **101**, 0645041-0645044 (2007).

32 Lögdlund, M., Lazzaroni, R., Stafström, S., Salaneck, W. R. & Brédas, J. L. Direct observation of charge-induced π-electronic structural changes in a conjugated polymer. *Phys. Rev. Lett.* **63**, 1841-1844 (1989).

33 Png, R. Q. *et al.* Electromigration of the conducting polymer in organic semiconductor devices and its stabilization by crosslinking. *Appl. Phys. Lett.* **91**, 013511 (2007).

34 Greczynski, G. *et al.* Photoelectron spectroscopy of thin films of PEDOT-PSS conjugated polymer blend: a mini-review and some new results. *J. Electron Spectrosc. Relat. Phenom.* **121**, 1-17 (2001).

35 Jukes, P. C. *et al.* Controlling the surface composition of poly(3,4-ethylenedioxythiophene)-poly(styrene sulfonate) blends by heat treatment. *Adv. Mater.* **16**, 807-811 (2004).

36 Martin, S. J. *et al.* Current-induced chain migration in semicondutor polymer blends. *Phys. Rev. B* **71**, 081308 (2005).

37 Crispin, X. *et al.* Conductivity, morphology, interfacial chemistry, and stability of poly(3,4-ethylenedioxythiophene)-poly(styrenesulfonate): A photoelectron spectroscopy study. *J. Polym. Sci. B: Polym. Phys.* **41**, 2561-2583 (2003).

38 Nardes, A. M. *et al.* Microscopic understanding of the anisotropic conductivity of PEDOT:PSS thin films. *Adv. Mater.* **19**, 1196-1200 (2007).

39 Campbell, I. H., Joswick, M. D. & Parker, I. D. Direct measurement of the internal electric field distribution in a multilayer organic light-emitting diode. *Appl. Phys. Lett.* **67**, 3171-3173 (1995).

40 Campbell, I. H. *et al.* Measuring internal electric fields in organic light-emitting diodes using electroabsorption spectroscopy. *Polymer. Adv. Tech.* **8**, 417-423 (1997).

41 Brown, T. M., Kim, J. S., Friend, R. H. & Cacialli, F. Built-in field electroabsorption spectroscopy of polymer light-emitting diodes incorporating a doped poly(3,4-ethylene-dioxythiophene) hole injection layer. *Appl. Phys. Lett.* **75**, 1679-1681 (1999).

42 Bodrozic, V. *et al.* The built-in potential in blue polyfluorene-based light-emitting diodes. *Adv. Mater.* **20**, 2410-2415 (2008).

43 Liu, B., Png, R. Q., Tan, J. K. & Ho, P. K. H. Evaluation of built-in potential and loss mechanisms at contacts in organic solar cells: Device model parameterization, validation, and prediction. *Adv. Energy Mater.* **4**, 1200972 (2014).

44 Pasveer, W. F. *et al.* Unified description of charge-carrier mobilities in disordered semiconducting polymers. *Phys. Rev. Lett.* **94**, 206601-206604 (2005).

45 Zhao, L. H. *et al.* Polarization effects on energy-level alignment at the interfaces of polymer organic semiconductor films. *Appl. Phys. Lett.* **101**, 053304 (2012).

46 Tsiper, E. V., Soos, Z. G., Gao, W. & Kahn, A. Electronic polarization at surfaces and thin films of organic molecular crystals: PTCDA. *Chem. Phys. Lett.* **360**, 47-52 (2002).

47 Koch, N. *et al.* Influence of molecular conformation on organic/metal interface energetics. *Chem. Phys. Lett.* **413**, 390-395 (2005).

48 Blom, P. W. M. & Vissenberg, M. C. J. M. Dispersive hole transport in poly(*p*-phenylene vinylene). *Phys. Rev. Lett.* **80**, 3819-3822 (1998).

49 Tanase, C., Meijer, E. J., Blom, P. W. M. & de Leeuw, D. M. Unification of the hole transport in polymeric field-effect transistors and light-emitting diodes. *Phys. Rev. Lett.* **91**, 216601-216604 (2003).

50 Blakesley, J. C. *et al.* Towards reliable charge-mobility benchmark measurements for organic semiconductors. *Org. Electron.* **15**, 1263-1272 (2014).

51 Png, R. Q. *et al.* High-performance polymer semiconducting heterostructure devices by nitrene-mediated photocrosslinking of alkyl side-chains. *Nature Mater.* **9**, 152-158 (2010).

Chapter 4.

Novel Surface Modifications of Copper for Applications in Organic Electronics

In this chapter, I describe our work in developing both low-workfunction and high-workfunction copper surfaces that may be suitable for use in organic electronic devices. Cu is an attractive electrode material for use in large area organic electronic devices because of its low cost. However, Cu has a native oxide layer that sets a Fermi level that typically falls deep within the gap of organic semiconductor materials which makes it unsuitable for charge-carrier injection into these materials. We show there is a practical solution-based method to generate low-workfunction (≤ 4.0 eV) and high-workfunction (≥ 5.2 eV) Cu surfaces. We utilize self assembly of thiocarbamate molecules on Cu/Cu_2O to make Cu surfaces with work-function of 3.7 eV according to ultraviolet photoelectron spectroscopy (UPS). XPS analysis reveals a Cu in Cu(I) state tightly bound to thiocarbamate. Efficient electron injection from these copper surfaces is demonstrated into the LUMO of poly{[N,N9-bis(2-octyldodecyl)-naphthalene-1,4,5,8-bis(dicarboximide)-2,6-diyl]-alt-5,59-(2,29-bithiophene)} (P(NDI2OD-T2), Polyera ActivInk N2200. On the other hand, pH or solvent controlled oxidation in hydrogen peroxide was used to prepare smooth Cu surfaces with workfunction as high as 5.4 eV as determined by UPS. X-ray photoelectron spectroscopy (XPS) results confirmed the dominant presence of oxidized copper in the Cu(II) state. The oxidized Cu shows superior injection in diode structures compared to the traditional PEDT:PSSH into [(9, 9'- dioctylfluorenyl -2,7- diyl) -co- (4, 4'-(N-(4- sec–butyl phenyl)) diphenylamine)] (TFB). Organic field effect transistors (OFETs) fabricated with these Cu films as source-drain electrode show lower contact resistance than gold for a poly(diketopyrrolopyrrole) (DPP) based semiconducting polymer.

4.1 Introduction

4.1.1 Alternative electrodes for organic electronics

Electrodes are critical components of polymer electronics, such as organic transistors, polymer light-emitting diodes (PLEDs) and organic photovoltaics (OPVs). For efficient devices, it is important to obtain electrodes with high sheet conductivity along with, for PLEDs and OPVs, high optical transmission.[1,2] Other factors such as price, ease of patterning, flexibility and stability should also be considered.

For optoelectronic devices, indium-tin-oxide (ITO) is currently the electrode of choice owing to its high conductivity and high transparency.[3] Oxygen vacancies in the indium oxide and doping by tin atoms leads to a Fermi level that is above the conduction band. This leads to a high conductivity in the range of 5000 S cm^{-1}.[4] ITO has a high band gap energy (>3.5 eV) which makes it transparent in the visible region. However, the short supply of indium sources has led to a sharp rise in the price of ITO.[5,6] In addition, most of the ITO deposition methods require either high deposition/annealing temperature or use sophisticated equipment such as pulsed lasers. Furthermore, ITO is brittle upon bending on flexible substrates. Indium diffusion in polymers has also been reported to be a reason for drop in device performance.[7] Hence, there is a need for viable alternatives to ITO. Other materials such as graphene, carbon nanotubes, and poly(3,4-ethylenedioxythiophene): poly(styrenesulfonic acid) (PEDT:PSSH), despite their high transparency, do not have high enough sheet conductivity to be independent electrodes.[6,8,9] Metal meshes, however, are becoming suitable substitutes to ITO in the fabrication of lighting devices.[2,10]

In the field of organic-field-effect transistors, gold has been the most commonly used electrode, owing to its stability and also its relatively high workfunction (clean gold has workfunction ~ 5.2 eV),[11,12] which facilitates charge injection into deep ionization potential polymers. However, there is a need for a replacement due to the high price of gold.

Currently, due to its low price and its processing flexibility, copper is being considered as a viable alternative to gold for the state-of-the-art conjugated polymer electronics. Pure copper with native copper oxide on top has a workfunction of 4.8 eV,[13] which makes it unsuitable for injection of electrons / holes into the highest-occupied-molecular-orbitals/lowest-unoccupied-molecular-orbitals (HOMO /LUMO) of polymers, which are often > 5.2 eV or < 4.0 eV, respectively. However, a copper electrode with an oxidized cupric oxide (workfunction ~ 5.3 eV)[14] can combine the superior electrical properties of pure copper and the injection capabilities of the oxidized copper. On the other hand, surfaces modified with self assembled molecules, which cause a decrease in the vacuum level of the top surface, leading to a drop in workfunction, can be used as electron injectors/ acceptors.

4.1.2 Copper and its oxides

Copper is a group IB transition metal, with atomic number 29 and atomic mass 63.55 amu. Pure copper is ductile and malleable at room temperature. It is one of the most abundant elements on earth's continental crust with 55 ppm (parts per million) concentration, which makes it more than 10^4 times more abundant than gold.[15] This overabundance of copper makes it more than 5000 times cheaper than gold. It is most often used, alloyed for higher mechanical strength, in electrical wiring. The excellent heat conductance of pure copper, 394

W/m·K and electrical conductance, 5.9 X 10^{-7} ohm^{-1}, make it an attractive metal for use in integrated circuits.[16] Towards the end of the 20th century, copper has replaced aluminum as the metal of choice in the microelectronic industry due its lower electromigration in interconnects.[17]

Copper surfaces oxidize in the ambient, forming copper oxides of a few nanometers thickness.[18,19] Copper oxidizes to the Cu(I) state as Cu_2O, and/or to the Cu(II) states, CuO and $Cu(OH)_2$ upon air exposure. Platzman et al describe a three step oxidation where a) the formation of Cu_2O due to copper ion migration to the surface b) formation of metastable $Cu(OH)_2$ due to adsorption of OH^- ions and c) conversion of the unstable $Cu(OH)_2$ into the more stable CuO.[20]

4.1.3 Cuprous oxide (Cu_2O)

Cu_2O has a simple cubic lattice with a lattice constant of 4.27 Å.[21] Due to copper vacancies in the lattice structure, Cu_2O is a p-type semiconductor.[22,23] The p-type nature of Cu_2O is supported by theoretical studies by Scanlon et al that show the copper vacancy V_{Cu} and the split vacancy V^{split} (a vacancy which is accompanied by a translocation of a lattice Cu atom towards the vacancy site) are more favorable than formation of interstitial oxygen (see Fig 4.1).[24] The Fermi level of Cu_2O is ~ 0.1 eV above the valence band with a band gap of ~ 2.3 eV, as measured by photocurrent measurements. The resistivity of Cu_2O has been reported to be in the range of 1000 – 2000 Ωcm,[25] and its charge carrier mobility 130 $cm^2V^{-1}s^{-1}$ at room temperature. Despite this low resistivity value (comparable to PEDT:PSSH used in devices),

the workfunction of Cu_2O is 4.84 eV, which limits its application as a charge carrrier injector into polymers with ionization potential (I_p) > 5.0 eV or LUMO < 4.0 eV.

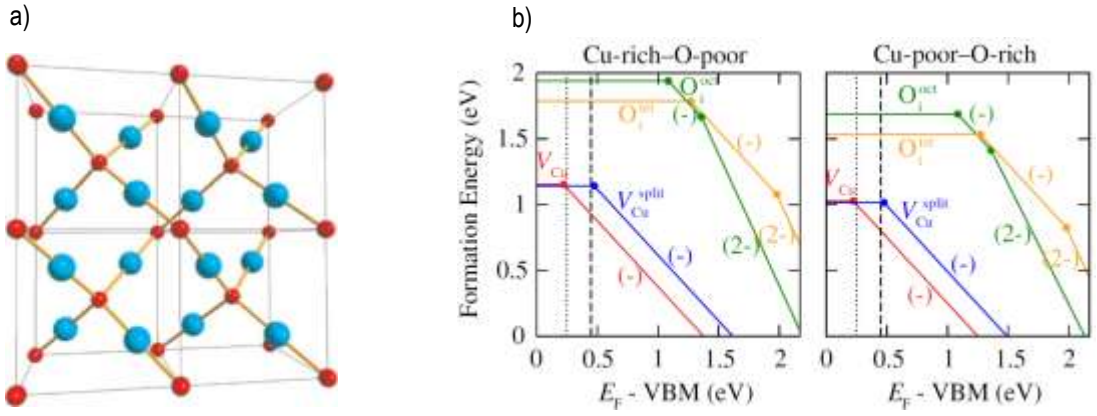

Figure 4.1. a) Cu_2O lattice[13] b) formation energy of the different possible defects in the lattice of Cu_2O.[24]

Cuprous oxide is commonly generated by heat treatment in air at a temperature range below 200 ^{0}C.[26] Higher temperatures are known to generate cupric oxide. Thin films of Cu_2O can be deposited via radio-frequency sputtering,[27,28] electrochemical reduction,[29] reactive evaporation,[30] or by plasma evaporation.[31] Metallic copper can also be oxidized to Cu_2O and CuO electrochemically. The formation of Cu_2O or CuO depends on the applied oxidation potential. Vvedenskii et al report that primary electrochemical reaction at the copper surface leads to the formation of Cu_2O at lower oxidative potential, and secondary mechanism (dissolution, oversaturation of near electrode layer, precipitation) leads to the formation of CuO at higher oxidative potential.[32] During the electrochemical process, conversion of Cu into Cu_2O comes about by the adsorption of OH on top of the copper surface which is followed by reorganization of the surface by long range atomic transport and hole/edge formation.[33] Figure 4.2a shows the oxidation of Cu(0) to Cu(I) in the range of the first anodic reaction (peak A_1) and to Cu(II) in the range of peak A_2. C2 and C1 show the stepwise reduction of the oxidized

copper during the cathodic process. The potential is plotted in Standard Hydrogen Electrode (SHE). The following reactions are expected depending on the applied potential.

$$2Cu + H_2O \rightarrow Cu_2O + 2H^+ + 2e^-$$

$$Cu + H_2O \rightarrow CuO + 2H^+ + 2e^-$$

$$Cu + 2H_2O \rightarrow Cu(OH)_2 + 2H^+ + 2e^-$$

$$Cu_2O + H_2O \rightarrow 2CuO + 2H^+ + 2e^-$$

$$Cu_2O + 3H_2O \rightarrow 2Cu(OH)_2 + 2H^+ + 2e^-$$

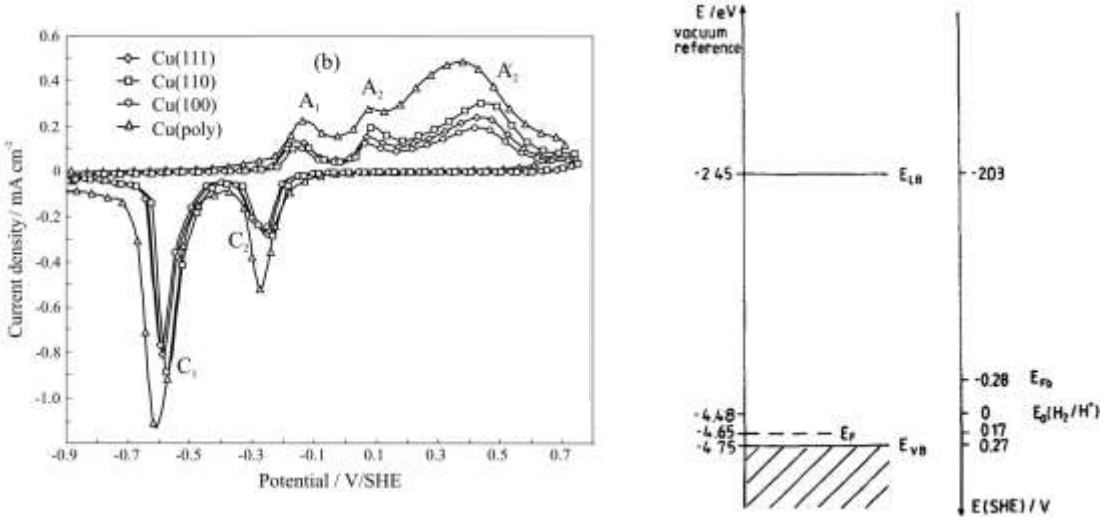

Figure 4.2. a)Voltammograms of the different copper crystal surfaces,[32] b)band diagram of Cu_2O.[22]

4.1.4 Cupric oxide (CuO)

CuO has a monoclinic symmetry with a unit cell containing four CuO molecules.[13] Similar to Cu_2O, CuO has copper vacancies in its crystalline structure and is hence a p-type semiconductor, with a Fermi level at 5.3 eV and a 3d valence band at 5.42 eV. This high

workfunction makes it attractive for applications with deep ionization-potential polymers.[14] It has a high mobility of ~ 0.1 cm^2/Vs, and high carrier concentration ~ $4X10^{18}$ cm^{-3}.

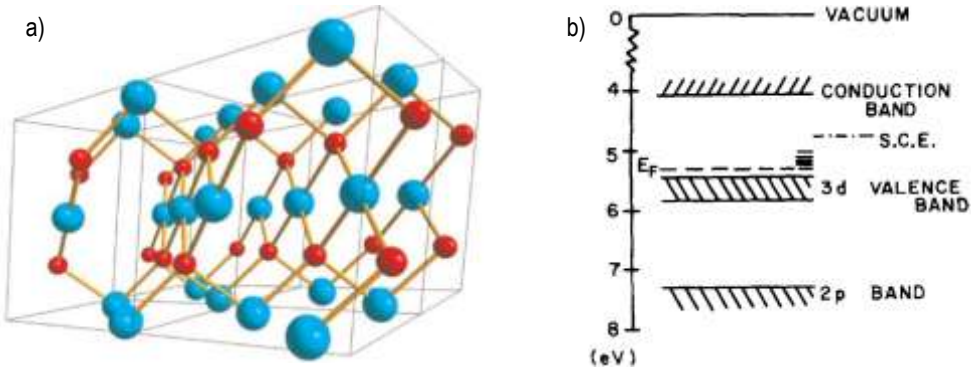

Figure 4.3. a) CuO lattice[13] b) band diagram of CuO.[14]

CuO can be made by oxidizing metallic copper via high temperature baking,[34] UV-ozone treatment,[35] oxygen plasma,[36] or electrochemical oxidation.[32] Cu_2O can be converted to CuO by baking at ~500 ^0C in 10^{-4} mbar of oxygen.[34] However, this high temperature method is not suitable for polymer substrates such as polyethylene terephtalate (PET) which undergo structural deformation at temperatures greater than ~ 140 ^0C. Murdoch et al report that 60 min of UV-ozone treatment can give ~ 6 nm thick CuO on top of metallic copper.[35] Although the UV-ozone method is compatible with plastic substrates, it produces pinholes and spikes with length scale of 30 nm on the copper surface, which could lead to device failure by causing shorted contacts. Since the formation of CuO by electrochemical oxidation involves dissolution and precipitation, the oxidized surface is rough and non-uniform which is undesirable in the preparation of multi-layered optoelectronic devices. Hence, a mechanism which converts metallic copper into CuO without affecting the underlying substrate and causing significant surface roughness is needed.

4.1.5 Passivation and cleaning of copper

On clean Cu, a thin layer of Cu_2O forms immediately after exposure to ambient, while it takes several hours for detectable amounts of CuO to form.[20] The speed of oxidation can be retarded by annealing to 580 ^{0}C in high vacuum.[37] This high temperature annealing leads to the formation of larger crystalline grains and smaller grain boundaries, which limit the concentration of the adsorbed OH^- ions which cause oxidation. Several other forms of oxidation inhibition have also been investigated. Platzman et al report on a self-assembled monolayer (SAM) of terephthalic acid (TPA) which can inhibit the formation of Cu(II) for more than 2 months in ambient.[37] Other SAMs such as n-dodecanthiol, n-dodecaneselenol,[38] benzotriazole,[39-41] octadecylthiol, propylthiol,[42] n-alkanethiols[43] have also been investigated which reduce the rate of copper oxidation by limiting the adsorption of OH^- ions. Several process of cleaning copper oxide from surfaces have also been developed. Etching by acetic acid,[18] and by vapor phase ethanol[44] have been demonstrated to remove copper oxides without etching the underlying copper. It is also possible to clean the oxides by a controlled etching with copper etchants, such as nitric acid and sulfuric acid, which also react with the underlying copper.[16]

4.1.6 Application of copper in organic electronics

There have been several attempts to use copper and/or its oxides as electrode components in organic devices such as light-emitting diodes, solar cells, and transistors.

Wang et al reported on an oxygen plasma oxidation of a very thin ~ 5 -10 nm thick film of copper deposited on glass for applications in organic light-emitting devices.[36] They reported light emitting efficiencies comparable to ITO based devices. However, light outcoupling is

limited by the transmittance of the copper surface. Hu et al improved hole injection of ITO into a light emitting polymer by depositing a nanometer thick layer of copper on top of ITO and oxidizing it by oxygen plasma.[45] They reported that the oxidized Cu(II) reduces the energy barrier by 0.2 eV without significant drop in light transmission, leading to lower operational voltage and higher luminance. Murdoch et al proposed UV-ozone treatment as an effective method to oxidize copper to cupric oxide (CuO) for efficient organic light emitting diodes.[35] Despite the attractive features such as high luminosity, low drive voltage, and easy patterning, the UV-ozone, introduces structural modifications of the copper giving rise to pin holes and spikes, which can lead to shorts and device failure.

Cuprous oxide (Cu_2O) has been studied for applications in Schottky barrier solar cells extensively. Its direct band gap of 2.0 eV, non-toxicity, abundance, and low price have made it very attractive.[25,46] Theoretically, Cu_2O solar cells can give efficiencies up to 20 %. However, so far, only cells with maximum efficiency of 2 % have been fabricated.[47] This is due to the resistivity of Cu_2O, the difficulty to produce controlled thicknesses of Cu_2O, and the inability to make n-type Cu_2O. Yoshida et al report on the improvement of Schottky-barrier cells by aging in air, but the final efficiencies do not exceed 0.5 %.[48] Cu_2O has also been used as a hole acceptor material in hybrid organic solar cells. Khan et al used electrochemically deposited Cu_2O to make a hybrid solar cell with PCBM.[49] However, due to low mobility and lifetime of charges in Cu_2O the overall power conversion efficiency did not exceed 0.1%. Lin et al use the sol-gel method to spin 10 nm of copper oxides, of which Cu_2O is the main component, between the silver electrode and the bulk polymers to facilitate hole collection.[50] They report an efficiency increase from 3.1 % to 4.0 %. However, this method is cumbersome because it involve an additional step of silver evaporation to make a low resistance electrode. In this

chapter, surface modification of complete copper electrodes are investigated. It is expected that such electrodes will combine the high conductivity of copper with the improved charge collection capabilities of the modified surface.

In the field of organic transistors, several groups have used the oxides of copper as electrode material in their devices. Park et al thermally evaporated CuO on top of pentacene to make top contact thin-film organic transistors.[51] They report improvement of the field effect mobility from 0.16 $cm^2V^{-1}s^{-1}$ to 0.34 $cm^2V^{-1}s^{-1}$ compared to transistors which have only gold electrodes due to better energy matching of the CuO and pentacene HOMO. Di et al report on pentacene based organic transistors with a Cu/CuOx electrode, which shows comparable device characteristics as devices made with gold electrodes.[52] They oxidized the high performance copper electrodes by exposure to ambient. However, they did not investigate the exact nature of this oxidized copper. Hence there is a need for a more robust and reproducible method of developing oxidized copper oxides.

4.1.7 The objective of this chapter

The aim of this chapter is to understand the processing space and determine whether practical solution-based methods can be found to develop high-workfunction (≥5.2 eV) and low-WF (≤ 4.0 eV) Cu surfaces that can provide high carrier injection rates into an adjacent semiconductor. Self assembly of small molecules on Cu/Cu_2O leads to low-workfunction surfaces while pH control and solvent control are found to be viable ways of attaining smooth high-workfunction surfaces. These modified surfaces have been successfully used to make organic electronic devices.

First, the state of copper in its intrinsic form is studied, followed by the effects of air exposure and ways of remaking 'clean' copper surfaces by acetic acid treatment. Next, the viability of low-workfunction Cu devices via thiocarbamate self assembly is investigated. Low-workfunction ~ 3.7 eV is achieved. With regards to high-workfunction copper surfaces, the effect of oxidation by hydrogen peroxide is investigated. Copper surfaces oxidized in 30 % H_2O_2 (in water) are found to be rough due to dissolution and back deposition of Cu(II) ions. At the hand of a Pourbiax diagram, the pH and oxidative potential space for the formation of Cu(II) is explained and supported by results of pH controlled experiments. Further control of oxidation is shown by using a solvent, diethyl carbonate, that limits the dissolution of Cu(II) ions into the solution. *n*-Type transistors are fabricated from the low-workfunction electrodes demonstrating their applicability to inject electrons into organic polymers. The high-workfunction oxidized copper surfaces are used to fabricate diodes which demonstrate superior hole injection into model TFB polymer. Transistors using the high-workfunction copper and poly(diketopyrrolopyrrole) (DPP) based polymer as organic semiconductor are also fabricated with comparable mobility and charge injection to control gold contact electrode devices.

4.2 Experimental Methods

4.2.1 Materials and film formation

Copper pellets of ~3 mm size with 99.99% purity were purchased from Testbourne for thermal evaporation. Glacial acetic acid with ≥ 99% purity was purchased from Sigma Aldrich. Electronic grade hydrogen peroxide (30% in water) was bought from Tee Hai, Singapore. The polymer TFB was purchased from Cambridge Display Technology (CDT), UK and Polyera ActivInk N2200PNDI polymer was purchased from Polyera Corporation, USA.

4.2.2 Ultraviolet photoemission spectroscopy

Valence band spectra were collected using He I radiation (21.21 eV) on an ESCALAB MkII spectrometer with the electron analyzer operated at constant pass energy of 5 eV to give a spectral resolution of 50 meV. The base pressure was ~ 10^{-9} mbar. The photoemission angle was set at θ=90°, and a standard sample bias of –10.00 V was applied to collect all the photoelectrons. The Fermi level kinetic energy $E_{k,Ef}$ was established from the Fermi step observed on a reference Ag foil. The workfunction φ was extracted from the low-energy cutoff $E_{k,LECO}$: $\varphi = E_{k,LECO} + 21.21 – E_{k,Ef}$.

4.2.3 X-ray photoemission spectroscopy

XPS was performed using MgKα X-ray (1253.6 eV) on a VG ESCALab Mk-II spectrometer operated at a base pressure of < 1 x 10^{-9} mbar, with sample grounded, and with 0.7 eV spectrometer resolution set by constant pass energy of 20 eV. The measured C1s, O1s, S2p,

N1s, Na1s, Cu2p core-level photoemission spectra were background/satellite corrected, curve fitted, integrated and corrected by empirical atomic photoemission cross sections to give the relative carbon and sulfur atomic concentrations sampled within the inelastic electron mean free path from the surface. The CuLMM Auger spectra were collected to give qualitative information about the existence of the different Cu species.

The XPS data was further used to make a quantitative study of the different copper surfaces. The atomic stoichiometry of top surface (overlayer) of a sample was analyzed by noting the peak area of an element (intensity, I), its' atomic sensitivity factor (ASF) and the number of scans. The ratio of element A to element B is given by the following equation:

$$\frac{n_A}{n_B} = \frac{I_A/ASF_A/n_{scansA}}{I_B/ASF_B/n_{scansB}}$$

Once the ratio of the different elements was identified, the thickness of the overlayer was calculated using the formula shown below, which describes the exponential loss of intensity of the emitted photoelectrons. The parameter ρ describes the atomistic density, d the thickness of the overlayer and λ is the inelastic mean free path (IMFP) for the specific core level electron and specific overlayer with known density and crystal structure.

$$\frac{I_{overlayer}}{I_{bulk}} = \frac{\rho_{overlayer}}{\rho_{bulk}} \times \left[\frac{1 - e^{\frac{-d}{\lambda}}}{e^{\frac{-d}{\lambda}}} \right]$$

4.2.4 Diode fabrication and characterisation

Hole-unipolar and electron-unipolar diodes were fabricated by spin coating 120 - 130 nm of TFB or PNDI polymer on surface modified copper electrodes, in the N_2 glovebox. Control devices were made by spin coating in ambient 1:6 PEDT:PSSH, dialyzed to remove ionic impurities, on Standard Clean 1 (SC1) cleaned ITO substrates to attain 50 nm film. The PEDT:PSSH solutions was pre-filtered through a 0.45-μm nylon syringe filter and the spun films were annealed at 140°C (hotplate) in N_2 glovebox. 120-nm-thick cathode film was thermally evaporated through a shadow mask at a base pressure of 10^{-7} Torr to give the cathode for eight 4.3 mm^2 pixels on each substrate. The current-voltage characteristics were collected on a probe station in the glovebox using a Keithley 4200 semiconductor parameter analyzer. Film thicknesses were measured by a profilometer (Tencor P2).

4.2.5 OFET fabrication and characterisation

OFETs in top-gate-bottom-contact (TGBC) structure were made by image reversal lithography patterned 50-nm-thick Cu or Au (on top of 7 nm Cr adhesion layer) electrodes thermally evaporated on polyethylene (PET) foils in a thermal evaporator at 10^{-6} mbar at a deposition rate of 0.15 – 0.25 nm/s. 30 nm thick poly(diketopyrrolopyrrole) (DPP) film was spin cast from 10mg/mL chlorobenzene solution followed by a 10 min bake at 100 ^{0}C in N_2-glovebox. The dielectric was 500 nm of polystyrene (2 million molecular weight) spin cast from 30 mg/ml solution in butyl acetate, and annealed at 80 ^{0}C for 10 min. Channel width of devices was 0.5 cm and channel length of the devices ranged from 3 to 100 μm. The gate electrode was thermally evaporated 7nm Cr and 30 nm Ag. FET measurements were done in the N_2-glovebox using a Keithley 4200-SCS semiconductor parameter analyzer.

4.2.6 Electromodulated absorption spectroscopy

Electron Absorption (EA) spectroscopy measurements of the diodes were performed at 30 K in a closed-cycle He cryostat (Janis APD HC-2). The pressure inside the chamber was maintained at 10^{-6} mbar. A sinusoidal drive voltage amplitude superposed on the selected dc bias was injected into the diode. Monochromatic light was incident through the glass substrate at 45°, and its reflection of the cathode collected by mirror optics onto a photodiode. The voltage output was demodulated by a lock-in amplifier phase locked to the ac to give the change in absorbance for a range of wavelength.

4.2.7 Atomic Force Microscopy

Atomic force microscopy (AFM) operating in tapping-mode (Dimension 3100, Digital Instruments) was used in ambient to study the topography of surfaces. Silicon cantilevers, scanning typically at 1 Hz scan speed were used.

4.2.8 Scanning Electron Microscopy

Scanning electron microscopy (SEM) was performed using JEOL JSM 5600LV scanning electron microscope. Substrates were cleaved and mounted vertically to investigate the thickness of the oxidized layers.

4.3 Results and Discussions

XPS is the primary technique used to characterize the copper surfaces. The core level spectra, Cu2p, O1s, and C1s and the Auger LMM transition were collected. The binding energies of the core levels for each compound are given in Table 4.1. The presence of Cu(II) can be quickly identified by the presence of the shake-up peaks that appear from 940 to 945 eV binding energy. Shake-up peaks are caused by photoelectrons which lose some of their kinetic energy by exciting an ion in an incomplete d-band.

Table 4.1 Binding energy values for investigated core levels

Core level	Compound	Binding energy (eV)
C1s	Hydrocarbon	284.5
O1s	CuO	529.6
	$Cu(OH)_2$	531.4
	Cu_2O	530.4
Cu2p	CuO	933.7
	$Cu(OH)_2$	935.0
	Cu_2O	932.7
	Cu	932.7
CuLMM	CuO	336.0
	$Cu(OH)_2$	335.7
	Cu_2O	336.8
	Cu	335.0

The Cu2p spectra can not distinguish between Cu(0) and Cu(I) states, both of which have a binding energy of 932.7 eV. To differentiate between the Cu(0) and Cu(I) the Cu LMM Auger spectra is used. In the Cu LMM spectra Cu (0) and Cu(I) give signals at 334.9 eV and 337.0 eV, respectively. From the O1s core spectra the state of the oxide for Cu(I) and Cu (II) can be identified. Oxygen bonded to Cu can exist predominantly in any of the following three

environments: Cu_2O, CuO or $Cu(OH)_2$ which are centered at 530.4 eV, 529.6 eV, and 531.4 eV, respectively. It is possible to have small amounts of oxygen which are bonded to adventitious carbon in the form of hydroxyl, carboxylic, carbonic or other forms. Shift in the adventitious C1s spectra give information about the surface nature of the underlying copper surface and/or the existence of dipole layers which lead to a shift of the vacuum level. The main part of the C1s spectra arises from adventitious carbon on the surface of the copper.

4.3.1 As-deposited copper

Copper was deposited in a thermal evaporator at a rate of 0.1 - 0.2 nm/s under a pressure of $1X10^{-6}$ Torr on 9X9 mm native-Silicon substrates. The sample was transferred in a N_2 atmosphere to the XPS measurement chamber to avoid air contamination and oxidation.

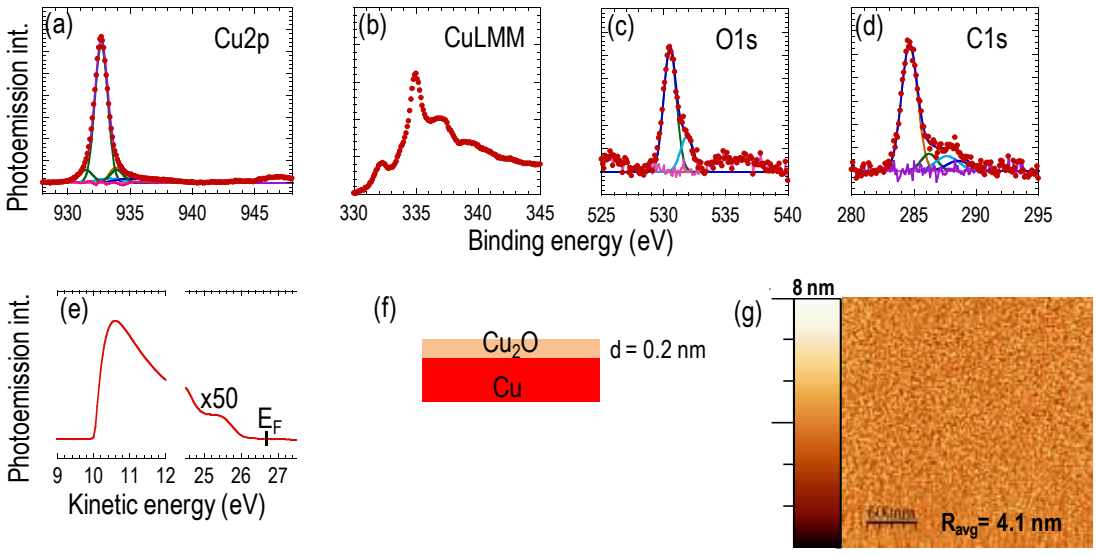

Figure 4.4. a) Cu2p, b) CuLMM, c) O1s, d) C1s XPS spectra, e)UPS spectra f) surface model and g) AFM of as-deposited Cu

Figure 4.4 shows the XPS and UPS spectra of the as-deposited copper. Figure 4.4a shows the Cu2p spectrum. Here, the Cu2p spectra of the as–deposited copper has only one main peak at 932.7 eV demonstrating that copper exists only in the Cu(0) and Cu(I) state. The existence of Cu(II) can be confidently excluded due to the lack of the characteristic Cu(II) shake-up peaks. By looking at Figure 4.4b we can conclude that the majority of the Cu at the top surface is Cu(0) as the peak is centered at 334.9 eV. Therefore, the state of the copper is the pristine form possible and has not been heavily oxidized or contaminated during evaporation and transfer of samples to the XPS chamber.

Figure 4.4c is the O1s core spectrum. The main peak centered at 530.4 eV, signifying predominant Cu_2O state, is in agreement with the Cu2p and CuLMM spectra. The C1s spectrum shown in Figure 4.4d shows adventitious methylated carbon centered at 284.6 eV, hydroxylated carbon at 286.2 eV, carboxylated carbon at 287.7 eV, and carbonated carbon at 288.7 eV. Figure 4.4e shows the UPS spectrum of the sample which shows the kinetic energy of the photoelectrons vs. the intensity at the low-energy-cut-off (LECO) (left) and the Fermi edge (right). The workfunction of Cu is determined by using $\phi = h\nu - (E_f - E_{LECO})$ where E_f is the energy at the Fermi edge and E_{LECO} is the energy at the LECO. The workfunction is determined to be 4.6 eV which is in agreement with literature values.[53,54]

The concentration of oxygen atoms bonded to copper was calculated from the O1s spectra, taking in consideration the sensitivity factor of the spectrometer and the number of sweeps done. This value was inserted in the model to find the thickness of Cu_2O on top of the bulk copper. For the model (Fig 4.4f), the Cu_2O cubic structure with the Cu atoms in face-centered-cubic (FCC) and the O atoms in body-centered-cubic (BCC) arrangement was used.

The inelastic mean free path (IMFP) was calculated with the NIST Standard Reference Database 71.[55] The values are given in Table 4.2.

Table 4.2 Calculated inelastic mean free path (IMFP) in nm for core level electrons travelling in different surfaces

Core level	CuO	Cu2O	Cu	Cu(OH)2
Cu2p	0.9	1.04	0.76	1.05
O1s	1.49	1.69		1.75

As can be seen in Figure 4.4f, the model predicts an ultrathin overlayer of copper oxide ~ 0.2 nm thick, which covers a bulk pure copper. It should be noted that, copper, similar to other reactive metals, forms an oxide layer even in the presence of low levels of oxygen, which is the case in the N_2 glove box. The fact that the copper oxide layer is ultrathin is attested by the observation of the Fermi level edge in the UPS spectra (Figure 4.4e). The electrons at the Fermi edge have a much lower energy (~ 26 eV) than the photoelectrons in the Cu2p XPS measurements and hence have a much lower IMFP (< 5 Å).

The AFM image in Figure 4.4g shows a smooth copper surface with an average roughness of 4.1 nm. This surface provides a defined reproducible state for further chemical modifications.

4.3.2 Effect of air exposure

A thicker layer of native oxide formed upon air exposure on a sample stored in air for 1 day in a class 1000 clean room at a temperature of 24 ^{0}C and 80% room humidity.

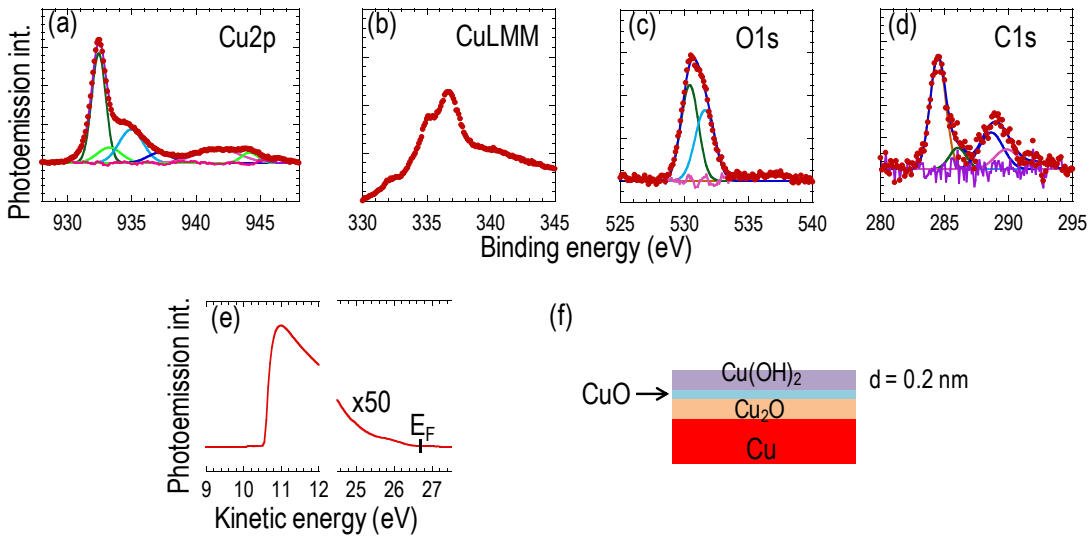

Figure 4.5. a) Cu2p, b) CuLMM, c) O1s, d) C1s XPS spectra, e)UPS spectra and f) surface model of air exposed Cu.

The emergence of the shake-up peaks in the Cu2p spectra (Fig 4.5a) is a clear indication of the formation of Cu(II) at the top surface. The Auger CuLMM spectra shows an increase in the Cu(II), specifically CuO, intensity. The O1s spectrum shows spectral components at 530.4 eV (Cu_2O) and at 531.4 eV ($Cu(OH)_2$). The model used to describe the surface is shown in Figure 4.5f. The model used to describe the top surface of the air-exposed sample is more complicated than as-evaporated copper because of the presence of multi oxide components. A thin monolayer of $Cu(OH)_2$ on top of thin layers of CuO and Cu_2O and bulk layer of Cu(0) is used to describe the surface. The thickness of the $Cu(OH)_2$ overlayer is found to be 0.2 nm. The workfunction of the native oxide is 5.1 eV. It is reported in the literature that oxidized Cu has higher workfunction than pure copper, in the range 4.9 - 5.3 eV.[13,14,56]

4.3.3 Effect of acetic acid treatment

To investigate the possibility of retaining pristine state of copper from rolled commercial copper, used copper films, and air-exposed copper surfaces, acetic acid treated sample was investigated by XPS and UPS.

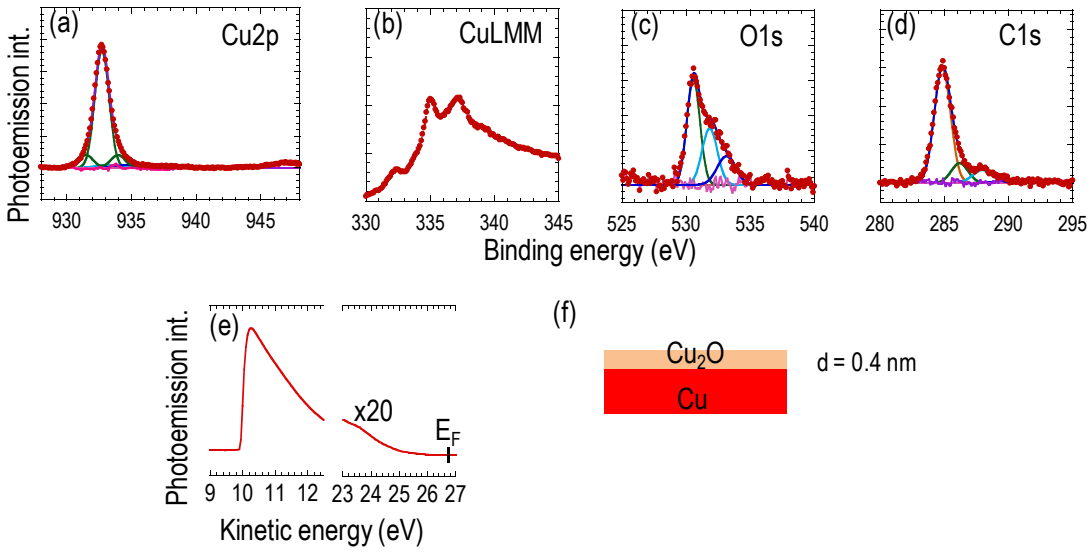

Figure 4.6. a) Cu2p, b) CuLMM, c) O1s, d) C1s XPS spectra, e)UPS spectra and f) surface model of copper cleaned by acetic acid.

Acetic acid is known to remove oxidized copper surface within less than 1 minute.[18] Typically, substrates to be cleaned were immersed in glacial acetic acid heated to ~ 60 ^{0}C for 4 min and then rinsed with isopropanol. Figure 4.6a shows that acetic acid removes Cu(II) from the top surface as indicated by the lack of the shake-up peaks in the Cu2p spectra. The CuLMM spectrum shows that there is Cu(I) at the top surface. Since the acetic acid treatment is done in ambient it is natural that there is a layer of Cu_2O. Using a model of a thin Cu_2O overlayer on bulk Cu, the thickness of the oxide layer has been modeled to be twice that of the evaporated Cu at 0.4 nm. The higher thickness of the oxide is confirmed by the non-existence of the Fermi

edge in the UPS spectra. The workfunction is found to be 4.5 eV suggesting that the higher workfunction observed in oxidized copper is due to the Cu(II).

4.3.4 Low WF copper with thiocarbamate surface modification

A self assembled layer chemically adsorbed on the copper surface can reduce the workfunction and workfunction manipulations of conducting electrodes via dipolar self assembled monolayers and polymers have been reported.[57-60] Apart from the workfunction matching with the adjacent organic polymer, the thickness of the SAM should also be minimized so that it does not act as a resistive layer between the copper and the polymer. Attaining ohmic contact between the adjacent layers is crucial for facilitated charge injection.

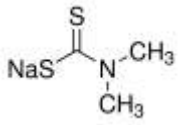

Figure 4.7. Chemical structure of sodium dimethyldithiocarbamate.

The use of dithiocarbamate compounds to modify work function of model gold surfaces has been reported.[61] In this thesis, dimethyldithiocarbamate is selected as a surface modifier. It has an electron rich S=C=S region and electron deficient C-N-C region, as seen in Figure 4.7. Clean copper surface was reacted with 1M of sodium dimethyldithiocarbamate in water. Preliminary results from XPS (see Figure 4.8) show that the dimethyldithiocarbamate reacts with the copper in 1:1 ratio. The copper is found in Cu(I) state as observed from the lack of shake-up peaks in the Cu2p core level spectra. The absence of oxygen and sodium as seen from the O1s and Na1s spectra indicates that there are no oxides of copper and no remnant

sodium dimethyldithiocarbamate on the surface of copper. The ratio N:S is found to be 1:2, which is the theoretical ratio in the original chemical (Fig 4.7), indicating that no chemical degradation took place. The workfunction is 3.7 eV, which is 1.1 eV lower than the workfunction of clean copper (Fig 4.8g). The surface keeps its low-workfunction upon baking to 140 ^{0}C, indicating its high stability and compatibility with organic electronic device processing. AFM, however, show that the surface of copper treated with sodium dimethyldithiocarbamate is rough with maximum average roughness ~ 40 nm. Hence, improved methodology to produce smooth, sodium dimethyldithiocarbamate treated Cu surfaces need to be explored. One possibility is through the control of the processing solvent to limit the dissolution of copper dimethyldithiocarbamate molecules, which could be causing the roughened surface due to back deposition. Nevertheless, this low-workfunction copper has been shown to inject electrons into model organic semiconductors (see section 4.3.5).

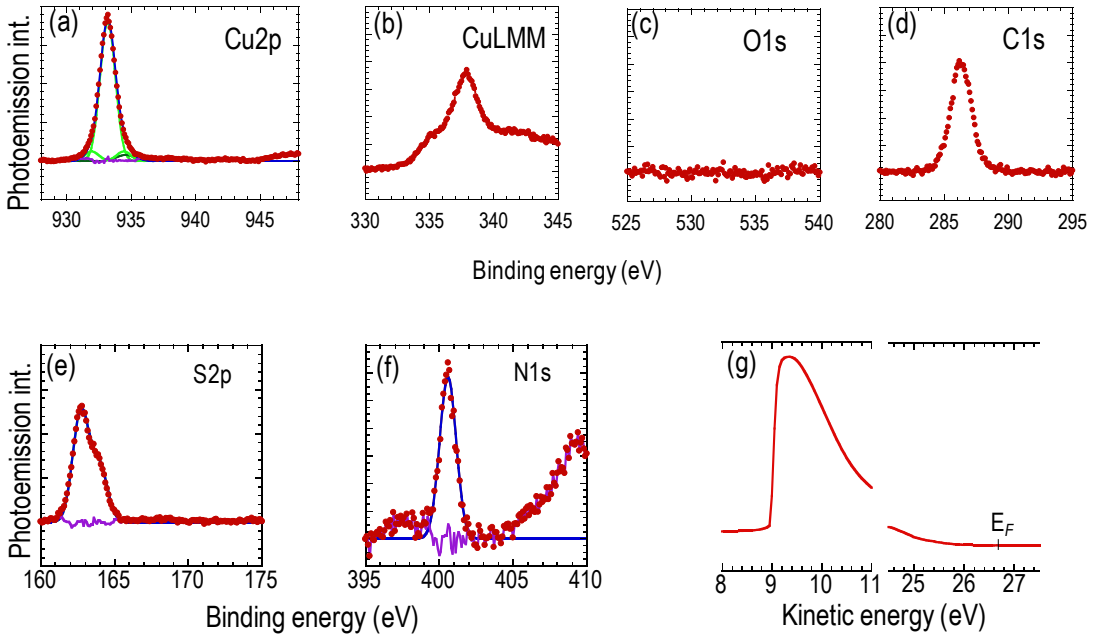

Figure 4.8. a) Cu2p, b) CuLMM, c) O1s, d) C1s e) S2p, f) N1s XPS spectra, g)UPS spectra of copper surface reacted with sodium dimethyldithiocarbamate.

4.3.5 Cu oxidized by hydrogen peroxide generating high-workfunction copper

Hydrogen peroxide is the most common oxidizing component used in chemical mechanical planarization (CMP) slurries used to smoothen copper surfaces in the semiconductor industry.[62] Despite its common use in CMP, the effect of hydrogen peroxide on the workfunction of pure copper surfaces and the applicability of these surfaces in electronic devices has not been investigated.

In this chapter the oxidation effect of hydrogen peroxide on copper is investigated. In a typical experiment, clean copper (50 nm Cu evaporated on 9X9 mm native silicon wafer and cleaned by acetic acid) is immersed in 30% H_2O_2 beaker kept at 36 ^{0}C in a thermal bath of water for 30 minutes. Then the substrate was rinsed with DI water and dried with N_2. The surface properties of the substrate were studies with UPS and XPS. UPS measurements give the workfunction of

the substrate to be 5.4±1 eV. The Cu2p XPS spectrum (see Fig 4.9a) of the sample shows high levels of Cu(II) in the forms of CuO and $Cu(OH)_2$ with more content of the former. The Auger CuLMM data also shows high content of CuO at the surface. However, as mentioned earlier, the chemical oxidation to Cu(II) follows by secondary mechanism (dissolution, oversaturation of near electrode layer, precipitation), which cause a rough surface (average roughness ~ 56 nm), as seen in the AFM image in Figure 4.9g.

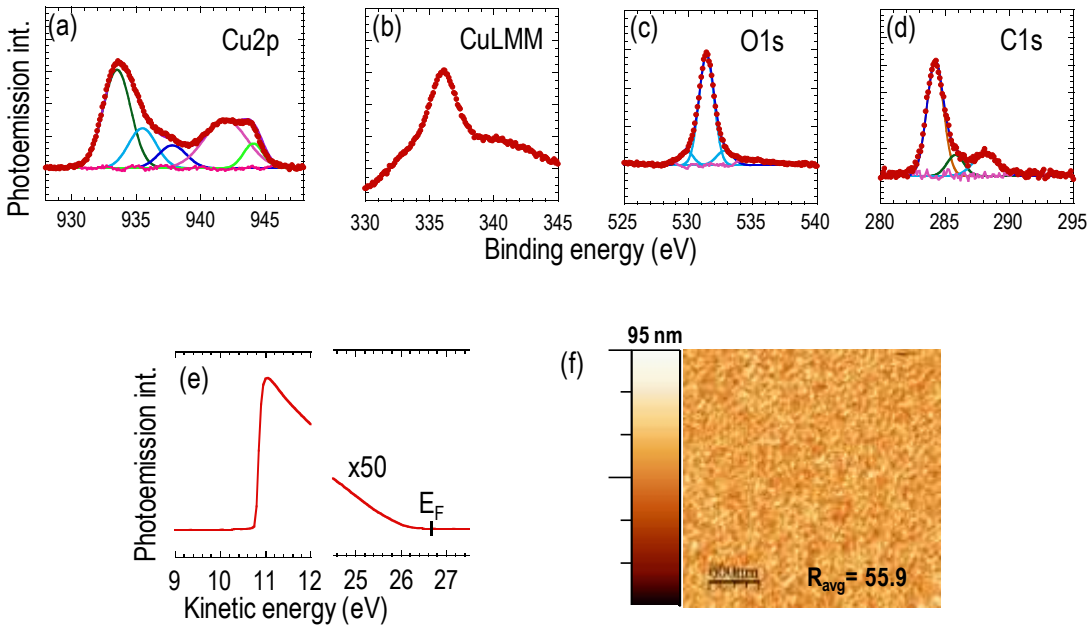

Figure 4.9. a) Cu2p, b) CuLMM, c) O1s, d) C1s XPS spectra, e)UPS spectra and f) AFM image of hydrogen peroxide treated sample.

The oxidized substrate was treated with acetic acid to see the drop in thickness of the evaporated film. The thickness of the copper oxidized to Cu(II) was determined to saturate at a thickness of 3-4 nm after extended oxidation time.

The stability of this high-workfunction electrode was studied. It was found that the electrode is stable up to several weeks both in the N_2 glovebox and ambient. Figure 4.10 shows the UPS spectra collected for samples prepared on the same batch and kept in ambient air of Class 1000 cleanroom at 24 ^{0}C and 80% room humidity. The workfunction value of the oxidized copper is always in the range 5.4±1 eV, demonstrating its stability. Hence, it is compatible for industrial use where storage and transportation time could be several weeks.

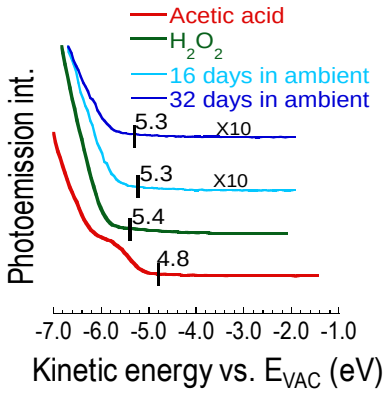

Figure 4.10. Stability of H_2O_2 treated samples kept in ambient air of Class 1000 cleanroom.

The hydrogen peroxide treatment for extended time produces a very rough surface. AFM images collected seen in Figure 4.9g have average roughness value of ~ 56 nm. This was confirmed by lateral SEM measurements done by dicing the substrates. The SEM images in Figure 4.11b indicate that there is a roughened surface on top of the initial evaporated Cu (thickness ~ 50 nm). Since the hydrogen peroxide does not etch the Cu, the mostly likely cause of the roughened surface is the back deposition of oxidized flakes. Such a roughened surface is not ideal for electronic device fabrications, as it can cause film irregularities and shorts to the opposite electrode.

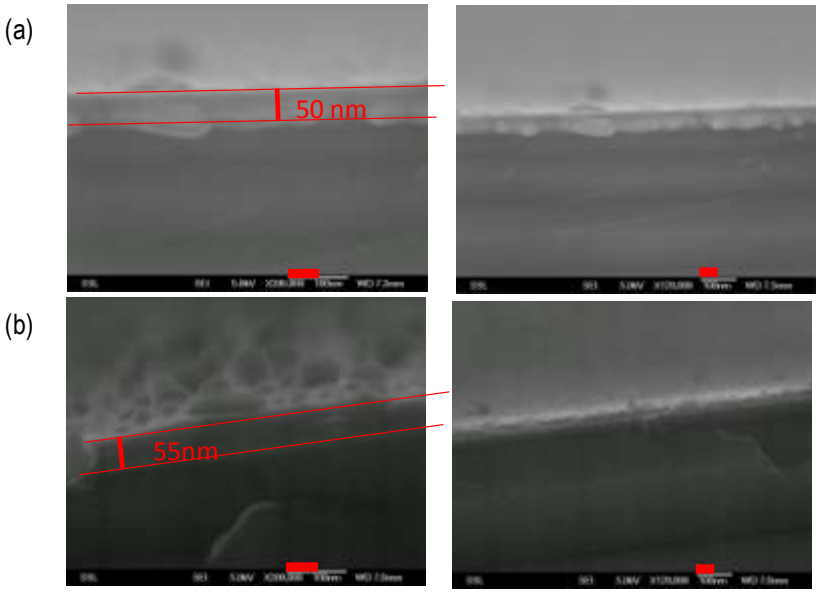

Figure 4.11. SEM images of H_2O_2 treated copper at (a) pH 7 and (b) without any buffer control. The red scale bars shown are 50 nm.

To identify the stable copper species at different pH and potential values, the Pourbiax diagram (Figure 4.12) of copper ions was studied. It can be seen that the Cu(II) species exist at higher oxidative potentials. The desired CuO species is only stable at pH values between 7 and 13. The metastable $Cu(OH)_2$ is present in the same ranges as CuO. Below pH7, copper is soluble in water as Cu(II) at higher potentials or is found as copper metal at lower oxidative potentials. We investigated the interaction of hydrogen peroxide with copper in a range of pH values. The buffer solutions were made by combining the following volume ratios of (0.1 M) citric acid and (0.2 M) sodium dihydrogen phosphate to give: pH4 (38.55:61.45), pH5 (51.50:48.50), pH6 (63.15:36.85), pH7 (82.35:17.65), and pH8 (97.25:2.75).

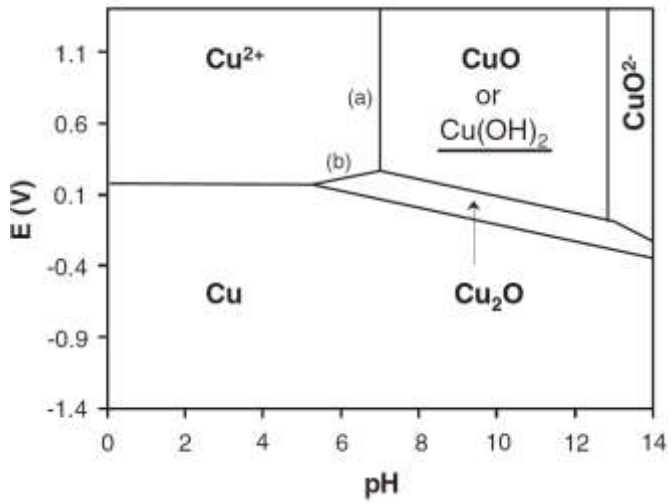

Figure 4.12. Pourbiax diagram showing the stability of copper species at 25 ^{0}C. $Cu(OH)_2$ is metastable.[62]

It was found that acidic pH solutions etch away the Cu, with the pH4 solution and pH5 solutions showing a thinning of the initial copper film after two minutes immersion. This can be explained by the Pourbiax which describes the solubility of copper at lower pH. SEM studies show that the surface roughness decreases up until pH7 (Figure 4.11). SEM images were taken on field-emission SEM (JEOL JSM 6700-F FE-SEM) operated at 20 μA and 5.0 kV. UPS measurements show that the workfunction is near 5.3 eV, independent of the pH of solution. Figure 4.13 shows XPS spectra for the pH7 treated sample which is quite similar to the pure hydrogen peroxide solution treated sample (ref. to Fig 4.9). The Cu2p XPS spectrum of the sample shows high levels of Cu(II) in the forms of CuO and $Cu(OH)_2$ with more content of the former. The Auger CuLMM data also shows high content of CuO at the surface. Hence, we have successfully attained a conductive high-workfunction treated copper surface which is morphologically suited to device fabrication. However, the presence of the copper species at a specific pH is quite sensitive to temperature and other preparation conditions which make it

difficult to have a highly controlled experiment. Hence, it is necessary to devise an experiment that is robust enough to withstand slight fluctuations in experimental conditions.

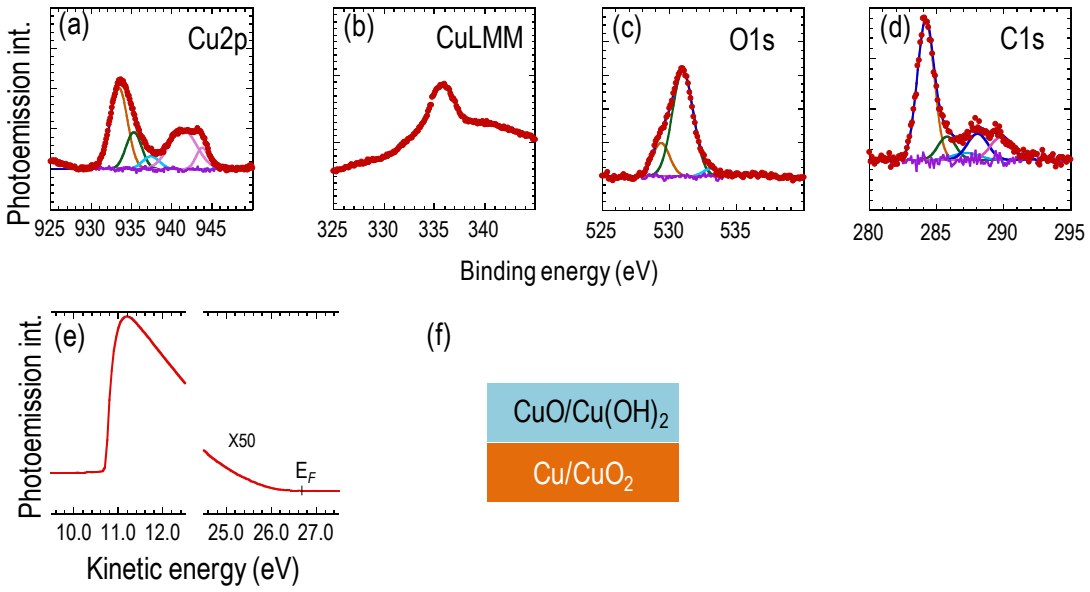

Figure 4.13. a) Cu2p, b) CuLMM, c) O1s, d) C1s XPS spectra, e)UPS spectra and f) surface model of copper surface modified with hydrogen peroxide at pH7.

As discussed previously, back deposition of precipitating hydroxide and oxide copper species is what cause the roughness on the top surface of the substrate. We devised a further control by solvent manipulation to limit the dissolution of cupric oxide and copper hydroxide molecules. The solvent control was successfully performed using diethyl carbonate as a solvent. Clean copper was reacted in 1M of H_2O_2 in diethyl carbonate at room temperature for 20 minutes. Figure 4.14 shows the XPS spectra. The Cu2p, CuLMM spectra are dominated by CuO and some amount of $Cu(OH)_2$ on the top surface with a small amount of Cu_2O and CuO also visible. The Cu(I) and Cu(0) species could be either underneath the Cu(II) or they could exist as unreacted parts on top of the surface. Further conclusions are not possible from the XPS data. For the case that the Cu(I) and Cu(0) lie underneath the $CuO/Cu(OH)_2$, the thickness can be

estimated to be ~ 3 nm from the inelastic mean free path (IMPF) of the electrons. AFM image analysis shows a roughness R_{avg} = 8 nm, which is a significant improvement over the pure hydrogen peroxide treated samples. Hence, this treatment is morphologically suited to device fabrication.

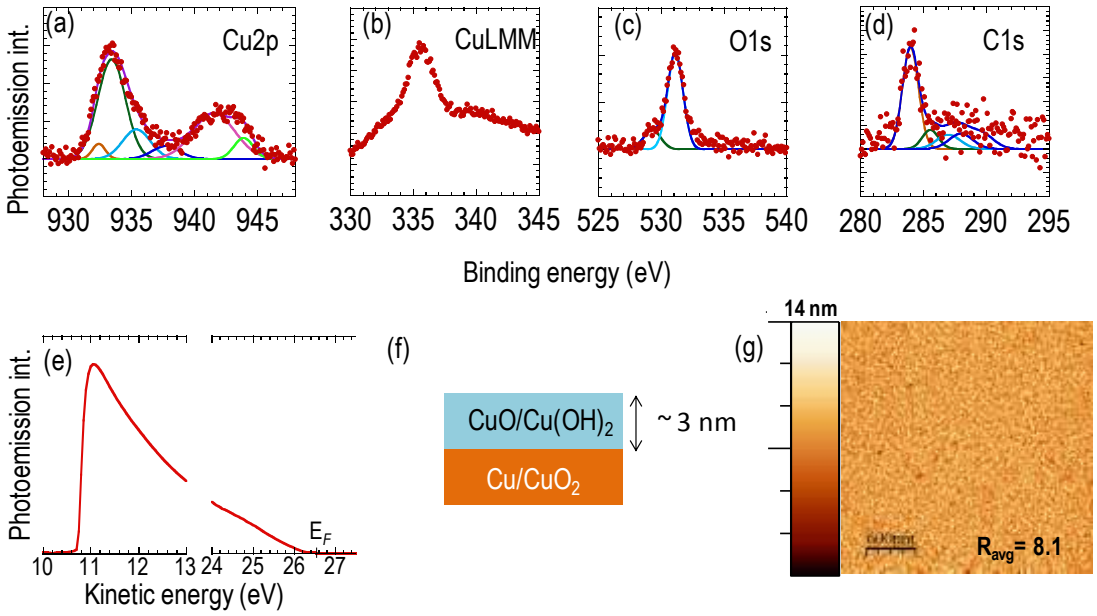

Figure 4.14. a) Cu2p, b) CuLMM, c) O1s, d) C1s XPS spectra, e)UPS spectra, f) surface model and g) AFM of copper surface modified with hydrogen peroxide in diethyl carbonate (DEC) .

4.3.6 Injection from low-workfunction and high-workfunction Cu electrodes in diodes

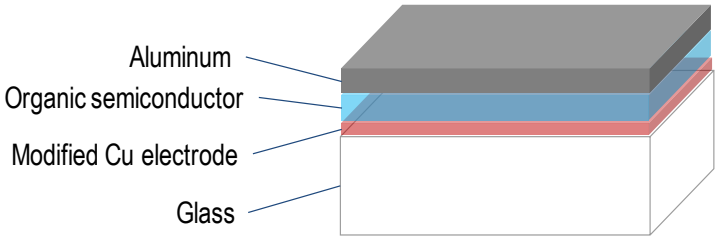

Figure 4.15. Diode structure of Cu based devices made in this chapter

The low-workfunction electrodes developed by surface modification with dimethyl dithiocarbamate are checked for their electron injection efficiency into the LUMO of poly{[N,N9-bis(2-octyldodecyl)-naphthalene-1,4,5,8-bis(dicarboximide)-2,6-diyl]-alt-5,59-(2,29-bithiophene)} (P(NDI2OD-T2), Polyera ActivInk N2200, a well know n-channel (electron transporting) semiconductor. For this experiment, 50 nm Cu (with underlying 7 nm Cr for adhesion) stripe was deposited on glass substrates. Then the substrates were dipped in 0.01 M of sodium dimethyl dithiocarbamate for 15 min. P(NDI2OD-T2) was spun in N_2 glovebox atmosphere from 20 mg/mL solution in anhydrous chlorobenzene, giving a thickness of ~ 90 nm. Following this the substrate was backed at 140 ^{0}C for 10 min. Finally, 120 nm of aluminum was shadow-deposited in a thermal evaporator. Control devices were made from pure Cu substrates and ITO/PEDT:PSSH substrates. The PEDT:PSSH was ~ 45 nm thick and baked at 140 ^{0}C in N_2 glovebox prior to P(NDI2OD-T2) deposition. Device measurement was done using Keithley 4200 scanning from 0 V to +4 V, +4 V to -4 V, and -4 V to 0 V, applied on the bottom electrode (i.e. dimethyl dithiocarbamate treated Cu or control electrodes).

As can be seen from Figure 4.16 the dimethyl dithiocarbamate treated surface shows vastly improved (up to two orders of magnitude) electron injection compared to the control Cu (with native oxide Cu2O). The control made of PEDT:PSSH, shows the least injection of electrons, as PEDT:PSSH has a high-workfunction (~5.2 eV).

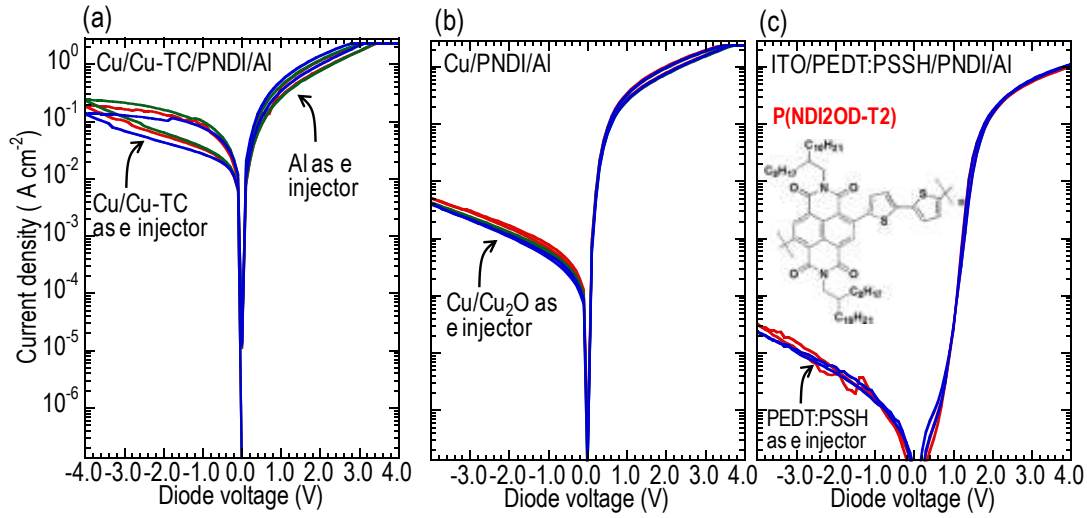

Figure 4.16. Charge injection into PNDI by a) surface modified copper with thiocarbamate (Cu-TC stands for Cu in Cu(I) state bonded to dimethyl dithiocarbamate), b) clean copper, and c) ITO/PEDT:PSSH. Inset in c) shows the chemical structure of P(NDI2OD-T2).

The high-workfunction copper oxide developed in this chapter is a viable replacement for ITO in the lighting industry. By making metal meshes of copper and oxidizing them with the robust method already described, efficient lighting systems can be realized. However, the transparency of the deposited copper limits its application for light-emitting-diode displays.

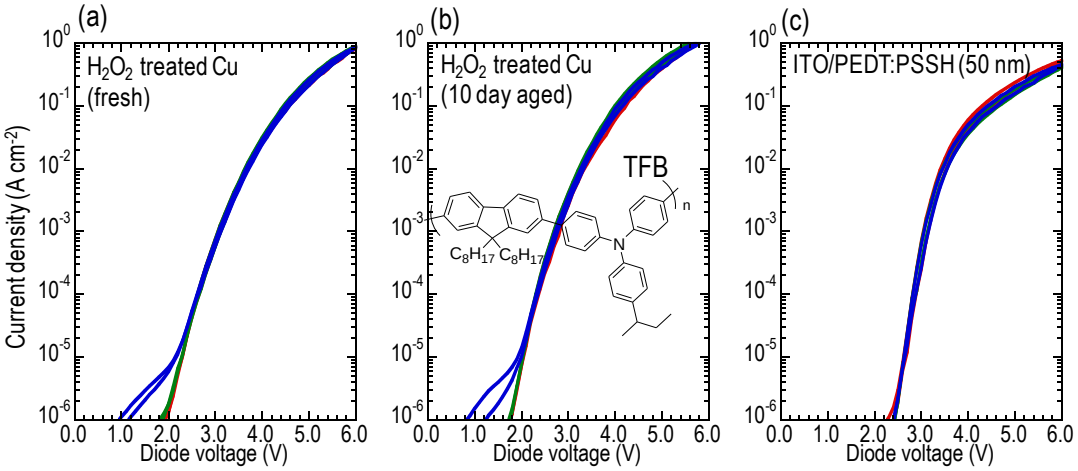

Figure 4.17. Charge injection into TFB by a) oxidized high-workfunction copper, b) aged oxidized high-workfunction copper, and c) ITO/PEDT:PSSH. Inset in b) shows the structure of TFB

To demonstrate the efficiency of charge injection from these oxidized copper surfaces, diode structures were made using poly [(9, 9'- dioctylfluorenyl -2,7- diyl) -co- (4, 4'-(N-(4- sec–butyl phenyl)) diphenylamine)] (TFB) with IP of 5.5 eV. For this experiment, 50 nm Cu stripes were deposited on glass substrates. Then the substrates were dipped typically in 30% H_2O_2 solution beaker kept in a 36 ^{0}C in water bath for 30 min. The substrates were then rinsed with DI water and dried by N_2 gas stream. TFB dissolved in anhydrous toluene was spun in N_2 glovebox giving a thickness of ~ 130 nm. Following this the substrate was backed at 120 ^{0}C for 10 min. Finally, 120 nm of aluminum was shadow-deposited in a thermal evaporator. Diodes using ITO/PEDT:PSSH as anode were used as control devices. Device measurement was done using Keithley 4200 scanning from 0 V to +6 V, +6 V to -6 V, and -6 V to 0 V, applied on the bottom electrode (i.e. oxidized Cu or control electrodes). The aged samples were kept in N_2 atmosphere during the aging period. Superior injection by oxidized Cu substrates was demonstrated, specifically at higher bias voltages, as compared to PEDT devices as shown in Figure 4.17 and summarized in Table 4.3.

Table 4.3 Driving voltage of diodes at different orders of magnitude of current density

J ($A\ cm^{-2}$)	V (V)		
	Oxidized Cu	**Oxidized Cu(aged)**	**PEDT:PSSH**
10^{-4}	2.65	2.4	2.85
10^{-3}	3.15	2.8	3.15
10^{-2}	3.8	3.35	3.55
10^{-1}	4.65	4.2	4.55
10^{0}	6.3	5.75	>7

To confirm that the workfunction of the oxidized copper substrates in device configuration is the same as that measured in vacuum (UPS) or does not undergo a transformation under

device operation, electroabsorption experiments (EA) were conducted. It has been reported that interfacial energetics play a big role in determining the effective workfunction of electrodes.[11] EA data was collected in reflective mode with the Al cathode serving as the back electrode. The measurements were performed at 30 K to avoid bulk injection and the resultant spectral complications. The copper anode was made thin so as to allow detectable intensity of monochormatized light to go through it.

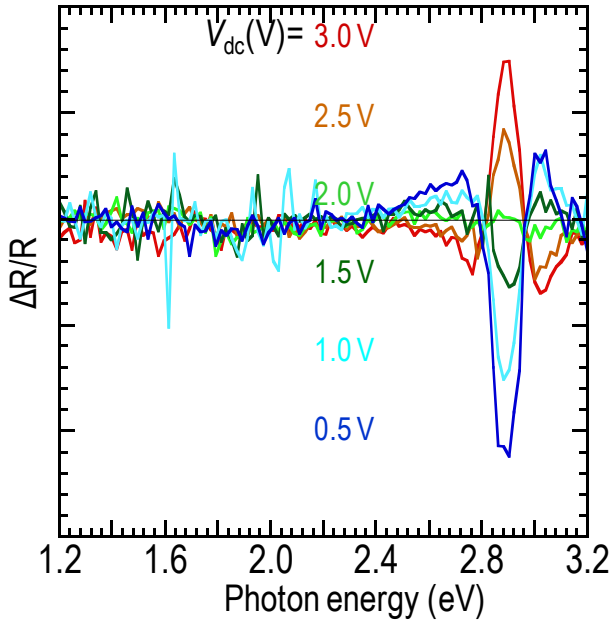

Figure 4.18. Electroabsorption spectra of 134 nm thick TFB sandwiched between high-workfunction copper and aluminum electrodes.

Figure 4.18 shows the $\Delta R/R$ EA spectra for high-workfunction-Cu/TFB/Al diodes. The Stark peak occurs at 2.9 eV, near the π–π^* absorption edge. The Stark peak shows polarity inversion at 1.95 (±0.05) V. The workfunction of Al in contact with TFB has been found to be 3.4 eV,[63] and was found to be independent of the organic polymer. This means that the

effective workfunction of the oxidized copper is $\phi_{TFB}^{Ox-Cu} = \phi_{TFB}^{Al} + eV_{bi}$ ~ 5.4 eV, which coincides well with the workfunction of the pure electrode measured in vacuum. Hence it is reasonable to conclude that the oxidized copper surface is robust and undergoes minimum changes due to interfacial interactions during device fabrication and operation.

4.3.7 Polymer field-effect-transistors

The high-workfunction of the oxidized copper is expected to facilitate charge injection into deep IP polymers. To study the viability of oxidized copper as contact electrode in transistors, top-gate-bottom-contact transistors were fabricated on PET foil. In a typical procedure, the PET foils were cleaned with acetone and IPA, dried with a stream of N_2. The source and drain electrodes were prepared by reverse-mask optical lithography. 7 nm Cr and 50 nm of Cu were deposited in a thermal evaporator. The semiconducting DPP polymer dissolved in chlorobenzene was spun in N_2 glovebox on substrate giving a thickness of 30 nm. The substrate was then baked at 100 ^{0}C for 10 min in GB. The gate dielectric used was 400 nm thick polystyrene (mw=2M) spun from a butyl acetate solution. The substrate was then baked at 80 ^{0}C for 10 min in GB after spinning the polystyrene. Finally, the top gate consisting of 7 nm Cr and 30 nm Ag was deposited by thermal evaporation. Control devices with oxygen plasma cleaned gold and untreated evaporated copper were prepared.

Device data in Figure 4.19 shows the transfer and output characteristics. The transfer curve of the as-deposited Cu electrodes (Fig 4.19a) shows that a high threshold voltages (25 V) is required to turn on the transistors. The onset of the output curve is shifted by ~ 6 V from the 0 V, signifying the existence of a large ohmic barrier to injection at low voltages. This indicates

that the contact resistance in these devices is large. In contrast both the oxidized copper and gold give lower threshold voltages (15 V). The charge injection at low drain voltages as seen in the output curves indicates that contact resistance is lower in these devices compared to the as-deposited Cu. There is also an increase in the overall current injected by the high-workfunction and Au electrodes. Hence, the high-workfunction oxidized copper can inject charges into high IP materials (DPP, IP ~ 5.3 eV) with high efficiency. The effective linear mobility of the oxidized copper devices was extracted from the transfer curve and was found to be ~ 0.1 $cm^2V^{-1}s^{-1}$, which is comparable to the mobility of the gold devices. All in all, efficient charge injection is observed in the oxidized copper electrodes which is comparable to the performance of the model Au electrode devices.

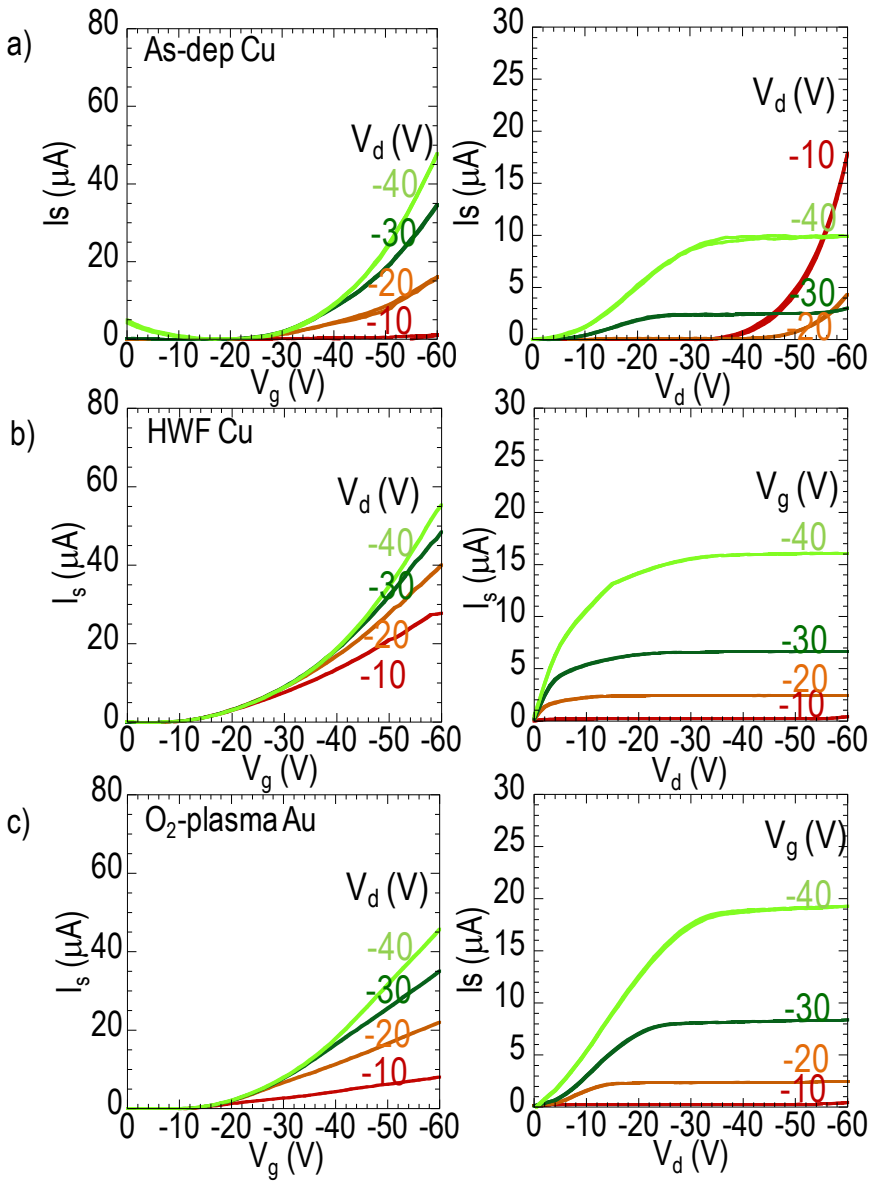

Figure 4.19. Transfer (left) and output (right) curves of transistors with electrodes of a) as-deposited Cu b) high-workfunction oxidized copper c) O_2-plama cleaned Au

4.3.8 Stability of devices

So far only the property of devices in a single run, or a few runs, has been studied. However, real commercial devices undergo much longer cycles. Hence it was important to look into the stress stability of both the diodes and the transistors built from the oxidized electrode.

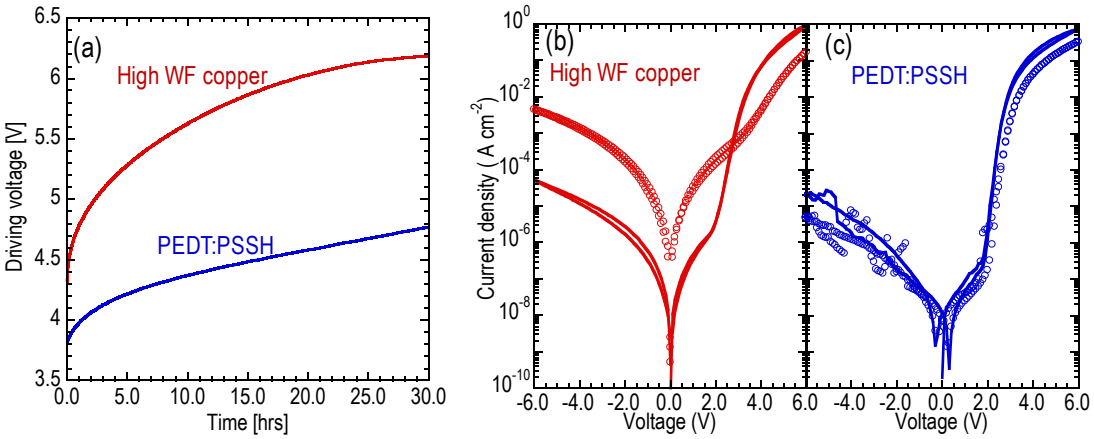

Figure 4.20. a) Voltage required to run devices at 120 mA cm^{-2} current density and the diode characteristics before (solid line) and after (symbol) 30 hours of stress for b) high-workfunction copper and c) PEDT:PSSH

Diodes made with the oxidized copper anode were stressed at 120 mA cm^{-2} for 30 hours in a N_2 glovebox. 120 mA cm^{-2} is within the range of the current density commercial LEDs are subjected to. As control, a diode made with ITO/PEDT:PSSH anode was measured in parallel. Figure 4.20a shows the voltage required to run the two diodes at the given current density. It can be seen that the Cu anode has a higher running voltage at 0 hrs due to ageing effects (stress test was done 51 days after device fabrication). Regardless of this fact, it is seen that the Cu anode undergoes a much rapid increase in its voltage throughout the stress test. In contrast, the control device has a slower increase in voltage, where the first few hours (~ 4 hrs) show accelerated increase followed by a constant increase for the rest of the stress test. The device diode characteristics were measured before and after the stress test. Figure 4.20b shows the results. It can be seen that copper devices has increased their current leakage by 2 orders of magnitude and the forward current has dropped by an order of magnitude. On the other hand, the control device does not show significant variation before and after stress, apart

from a slight drop in the forward current. This shows that the diode behavior of the copper device has become compromised during the stress test. Electromigration has been reported to be a cause of failure in electronic devices that could have led to leakage current.[64] The chemical instability of the high-workfunction layer upon stress could also be an issue.

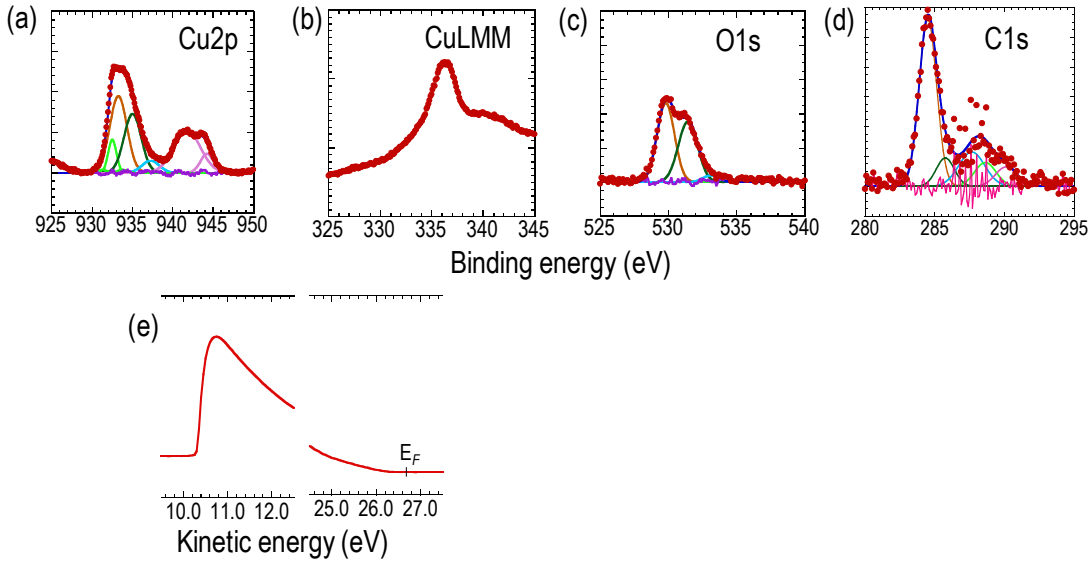

Figure 4.21. a) Cu2p, b) CuLMM, c) O1s, d) C1s XPS spectra, e)UPS spectra and f) surface model of baked oxidized copper substrate

To demonstrate the effect of heat, the high-workfunction electrode was baked at 140 ^{0}C in the glove box, and the surface studied with UPS and XPS, shown in Figure 4.21. The UPS reveals that the workfunction has dropped from 5.3 eV to 4.9 eV after baking. Hence, the drop in device performance is possibly due to a higher barrier height between the anode and the LEP. The Cu2p spectrum reveals the presence of Cu_2O in the first few nanometers, which is possibly made by the reduction of CuO during baking. The Auger CuLMM spectra also shows the presence of Cu_2O. Cu_2O is reported to have a workfunction of 4.8 eV.[65] Hence, the drop in

workfunction in the baked sample can be attributed to the non-uniformity of the oxide layer, which contains significant amounts of Cu_2O. Therefore, there is a need to stabilize the Cu(II) oxidized Cu. Stabilization mechanism by using self assembling molecules which bind tightly to the copper in its Cu(II) state are currently being investigated.

4.4 Conclusion and Future Outlook

Copper's inexpensive price, its electrical and mechanical properties make it a very attractive electrode material in organic electronics. In this chapter the nature of copper in its pure form and upon various chemical treatments was investigated. XPS has been an indispensible tool in studying the chemical properties of various copper surfaces. UPS was used to obtain the workfunction of the surfaces, while AFM and SEM were used to do morphological studies. Clean, as-deposited copper has a workfunction of ~ 4.6 eV and was seen to have a thin (~0.2 nm) thick layer of Cu_2O on top of bulk Cu. Upon air exposure for 1 day the thickness of the top layer was found to have partially oxidized into CuO and $Cu(OH)_2$. The effects of ambient air exposure can be reversed by immersing in acetic acid, which removes all Cu(II) species on the top surface without affecting the underlying Cu. A method was developed to produce low-workfunction copper by using dimethyl dithiocarbamate groups. Further on, a simple and robust way of developing high-workfunction Cu, by immersion in hydrogen peroxide was developed. This high-workfunction surface was found to be stable in the glove box and ambient air. pH control and solvent control are employed to avoid surface roughening caused by back deposition of copper oxides/hydroxides. Devices made from these high-workfunction and low-workfunction copper give high performance compared with current standard electrodes. However, deterioration of device performance upon extended operation has been observed. Appreciable stabilization have been achieved using dicyanoimidazole as a surface modifiers, which maintains the high-workfunction state of the CuO and at the same time is stable at high temperature. More experiments need to be carried out in order to optimize the processing for organic diodes and transistors.

4.5 References

1 Facchetti, A. & Marks, T. J. *Transparent electronics*. (Wiley, Chichester, UK, 2010).

2 Lee, J.-Y., Connor, S. T., Cui, Y. & Peumans, P. Solution-processed metal nanowire mesh transparent electrodes. *Nano Lett.* **8**, 689-692 (2008).

3 Kim, H. *et al.* Electrical, optical, and structural properties of indium-tin-oxide thin films for organic light-emitting devices. *J. Appl. Phys.* **86**, 6451-6461 (1999).

4 Tahar, R. B. H., Ban, T., Ohya, Y. & Takahashi, Y. Tin doped indium oxide thin films: Electrical properties. *J. Appl. Phys.* **83**, 2631-2645 (1998).

5 Minami, T. Present status of transparent conducting oxide thin-film development for Indium-Tin-Oxide (ITO) substitutes. *Thin Solid Films* **516**, 5822-5828 (2008).

6 Kumar, A. & Zhou, C. The race to replace tin-doped indium oxide: which material will win? *ACS Nano* **4**, 11-14 (2010).

7 De Jong, M., Van Ijzendoorn, L. & De Voigt, M. Stability of the interface between indium-tin-oxide and poly (3, 4-ethylenedioxythiophene)/poly (styrenesulfonate) in polymer light-emitting diodes. *Appl. Phys. Lett.* **77**, 2255-2257 (2000).

8 Groenendaal, L., Jonas, F., Freitag, D., Pielartzik, H. & Reynolds, J. R. Poly (3, 4-ethylenedioxythiophene) and its derivatives: past, present, and future. *Adv. Mater.* **12**, 481-494 (2000).

9 Venugopal, A., Colombo, L. & Vogel, E. Contact resistance in few and multilayer graphene devices. *Appl. Phys. Lett.* **96**, 013512 (2010).

10 Kang, M. G. & Guo, L. J. Nanoimprinted semitransparent metal electrodes and their application in organic light-emitting diodes. *Adv. Mater.* **19**, 1391-1396 (2007).

11 Zhou, M. *et al.* Effective work functions for the evaporated metal/organic semiconductor contacts from in-situ diode flatband potential measurements. *Appl. Phys. Lett.* **101**, 013501 (2012).

12 Zhao, L.-H. *et al.* Polarization effects on energy-level alignment at the interfaces of polymer organic semiconductor films. *Appl. Phys. Lett.* **101**, 053304 (2012).

13 Meyer, B. *et al.* Binary copper oxide semiconductors: From materials towards devices. *Phys. Status Solidi B* **249**, 1487-1509 (2012).

14 Koffyberg, F. & Benko, F. A photoelectrochemical determination of the position of the conduction and valence band edges of p ‐ type CuO. *J. Appl. Phys.* **53**, 1173-1177 (1982).

15 Taylor, S. Abundance of chemical elements in the continental crust: a new table. *Geochim. Cosmochim. Acta* **28**, 1273-1285 (1964).

16 Walker, P. & Tarn, W. H. *CRC handbook of metal etchants*. (CRC press, 1990).

17 Tu, K. Recent advances on electromigration in very-large-scale-integration of interconnects. *J. Appl. Phys.* **94**, 5451-5473 (2003).

18 Chavez, K. & Hess, D. A novel method of etching copper oxide using acetic acid. *J. Electrochem. Soc.* **148**, G640-G643 (2001).

19 Chuang, C.-L., Aoh, J.-N. & Din, R.-F. Oxidation of copper pads and its influence on the quality of Au/Cu bonds during thermosonic wire bonding process. *Microelectron. Reliab.* **46**, 449-458 (2006).

20 Platzman, I., Brener, R., Haick, H. & Tannenbaum, R. Oxidation of polycrystalline copper thin films at ambient conditions. *J. Phys. Chem. C* **112**, 1101-1108 (2008).

21 Jukes, P. C. *et al.* Controlling the surface composition of poly (3, 4-ethylene dioxythiophene)-poly (styrene sulfonate) blends by heat treatment. *Adv. Mater.* **16**, 807-811 (2004).

22 Collisi, U. & Strehblow, H.-H. A photoelectrochemical study of passive copper in alkaline solutions. *J. Electroanal. Chem. Interfac. Electrochem.* **210**, 213-227 (1986).

23 Isseroff, L. Y. & Carter, E. A. Electronic structure of pure and doped cuprous oxide with copper vacancies: suppression of trap states. *Chem. Mater.* **25**, 253-265 (2013).

24 Scanlon, D. O., Morgan, B. J., Watson, G. W. & Walsh, A. Acceptor levels in p-type Cu2O: rationalizing theory and experiment. *Phys. Rev. Lett.* **103**, 096405 (2009).

25 Olsen, L., Addis, F. & Miller, W. Experimental and theoretical studies of Cu2O solar cells. *Sol. Cells* **7**, 247-279 (1982).

26 Roos, A. & Karlsson, B. Properties of oxidized copper surfaces for solar applications II. *Solar Energy Mater.* **7**, 467-480 (1983).

27 Akimoto, K. *et al.* Thin film deposition of Cu 2 O and application for solar cells. *Sol. Energy* **80**, 715-722 (2006).

28 Fujinaka, M. & Berezin, A. A. Cuprous oxide-indium-tin oxide thin film photovoltaic cells. *J. Appl. Phys.* **54**, 3582-3588 (1983).

29 Golden, T. D. *et al.* Electrochemical deposition of copper (I) oxide films. *Chem. Mater.* **8**, 2499-2504 (1996).

30 Balamurugan, B. & Mehta, B. Optical and structural properties of nanocrystalline copper oxide thin films prepared by activated reactive evaporation. *Thin solid films* **396**, 90-96 (2001).

31 Santra, K., Sarkar, C., Mukherjee, M. & Ghosh, B. Copper oxide thin films grown by plasma evaporation method. *Thin Solid Films* **213**, 226-229 (1992).

32 Vvedenskii, A., Grushevskaya, S., Ganzha, S., Eliseev, D. & Abakumova, L. Copper oxides: kinetics of formation and semiconducting properties. Part II. Copper single crystals. *J. Solid State Electrochem.* **18**, 3437-3451 (2014).

33 Kunze, J., Maurice, V., Klein, L. H., Strehblow, H.-H. & Marcus, P. In situ STM study of the duplex passive films formed on Cu (111) and Cu (001) in 0.1 M NaOH. *Corros. Sci.* **46**, 245-264 (2004).

34 Poulston, S., Parlett, P., Stone, P. & Bowker, M. Surface oxidation and reduction of CuO and Cu2O studied using XPS and XAES. *Surf. Interface Anal.* **24**, 811-820 (1996).

35 Murdoch, G., Greiner, M., Helander, M., Wang, Z. & Lu, Z. A comparison of CuO and Cu2O hole-injection layers for low voltage organic devices. *Appl. Phys. Lett.* **93**, 083309 (2008).

36 Wang, S., Osasa, T. & Matsumura, M. CuOx films as anodes for organic light-emitting devices. *Jpn. J. Appl. Phys.* **45**, 8894 (2006).

37 Platzman, I., Saguy, C., Brener, R., Tannenbaum, R. & Haick, H. Formation of Ultrasmooth and Highly Stable Copper Surfaces through Annealing and Self-Assembly of Organic Monolayers. *Langmuir* **26**, 191-201 (2009).

38 Mekhalif, Z., Fonder, G., Laffineur, F. & Delhalle, J. Comparative assessment of n-dodecanethiol and n-dodecaneselenol monolayers on electroplated copper. *J. Electroanal. Chem.* **621**, 245-253 (2008).

39 Brusic, V. *et al.* Copper corrosion with and without inhibitors. *J. Electrochem. Soc.* **138**, 2253-2259 (1991).

40 Cohen, S. *et al.* X-ray photoelectron spectroscopy and ellipsometry studies of the electrochemically controlled adsorption of benzotriazole on copper surfaces. *J. Vac. Sci. Technol., A* **8**, 2417-2424 (1990).

41 Finšgar, M. & Milošev, I. Inhibition of copper corrosion by 1, 2, 3-benzotriazole: a review. *Corros. Sci.* **52**, 2737-2749 (2010).

42 Keller, H., Simak, P., Schrepp, W. & Dembowski, J. Surface chemistry of thiols on copper: an efficient way of producing multilayers. *Thin Solid Films* **244**, 799-805 (1994).

43 Laibinis, P. E. & Whitesides, G. M. Self-assembled monolayers of n-alkanethiolates on copper are barrier films that protect the metal against oxidation by air. *J. Am. Chem. Soc.* **114**, 9022-9028 (1992).

44 Satta, A. *et al.* The removal of copper oxides by ethyl alcohol monitored in situ by spectroscopic ellipsometry. *J. Electrochem. Soc.* **150**, G300-G306 (2003).

45 Hu, W., Manabe, K., Furukawa, T. & Matsumura, M. Lowering of operational voltage of organic electroluminescent devices by coating indium-tin-oxide electrodes with a thin CuOx layer. *Appl. Phys. Lett.* **80**, 2640-2641 (2002).

46 Rai, B. Cu2O solar cells: a review. *Sol. Cells* **25**, 265-272 (1988).

47 Mittiga, A., Salza, E., Sarto, F., Tucci, M. & Vasanthi, R. Heterojunction solar cell with 2% efficiency based on a Cu2O substrate. *Appl. Phys. Lett.* **88**, 163502-163502-163502 (2006).

48 Yoshida, Y., Tanaka, S., Fujita, Y. & Hiromitsu, I. Organic thin-film solar cells with a Cu anode: Improvement of the photovoltaic properties on aging in air. *J. Appl. Phys.* **106**, 064510 (2009).

49 Khan, M. A., Septina, W., Ikeda, S. & Matsumura, M. An inorganic/organic hybrid solar cell consisting of Cu2O and a fullerene derivative. *Thin Solid Films* **526**, 191-194 (2012).

50 Lin, M.-Y. *et al.* Sol-gel processed CuOx thin film as an anode interlayer for inverted polymer solar cells. *Org. Electron.* **11**, 1828-1834 (2010).

51 Park, J.-W. *et al.* Effects of copper oxide/gold electrode as the source-drain electrodes in organic thin-film transistors. *Electrochem. Solid-State Lett.* **10**, H340-H343 (2007).

52 Di, C. a. *et al.* High-performance organic field-effect transistors with low‐cost copper electrodes. *Adv. Mater.* **20**, 1286-1290 (2008).

53 Anderson, P. A. The work function of copper. *Phys. Rev.* **76**, 388 (1949).

54 Gartland, P., Berge, S. & Slagsvold, B. Photoelectric work function of a copper single crystal for the (100),(110),(111), and (112) faces. *Phys. Rev. Lett.* **28**, 738 (1972).

55 Powell, C. & Jablonski, A. The NIST electron effective-attenuation-length database. *J. Surf. Anal.* **9**, 322-325 (2002).

56 Kim, S., Hong, K., Kim, K., Lee, I. & Lee, J.-L. Phase-controllable copper oxides for an efficient anode interfacial layer in organic light-emitting diodes. *J. Mater. Chem.* **22**, 2039-2044 (2012).

57 Zhou, Y. *et al.* A universal method to produce low-work function electrodes for organic electronics. *Science* **336**, 327-332 (2012).

58 Schulz, P. *et al.* Comparison of the energy-level alignment of thiolate-and carbodithiolate-bound self-assembled monolayers on gold. *J. Phys. Chem. C* **114**, 20843-20851 (2010).

59 Alloway, D. M. *et al.* Interface dipoles arising from self-assembled monolayers on gold: UV-photoemission studies of alkanethiols and partially fluorinated alkanethiols. *J. Phys. Chem. B* **107**, 11690-11699 (2003).

60 Alloway, D. M. *et al.* Tuning the effective work function of gold and silver using ω-functionalized alkanethiols: Varying surface composition through dilution and choice of terminal groups. *J. Phys. Chem. C* **113**, 20328-20334 (2009).

61 Von Wrochem, F. *et al.* Uses of dithiocarbamate compounds. (2010).

62 DeNardis, D., Rosales-Yeomans, D., Borucki, L. & Philipossian, A. Characterization of copper-hydrogen peroxide film growth kinetics. *Thin Solid Films* **513**, 311-318 (2006).

63 Chia, P.-J. *et al.* Direct evidence for the role of the Madelung potential in determining the work function of doped organic semiconductors. *Phys. Rev. Lett.* **102**, 096602 (2009).

64 Black, J. R. Electromigration - A brief survey and some recent results. *IEEE Trans. Electron Dev.* **16**, 338-347 (1969).

65 Yang, W.-Y. & Rhee, S.-W. Effect of electrode material on the resistance switching of Cu2O film. *Appl. Phys. Lett.* **91**, 232907 (2007).

Chapter 5. Summary and Outlook

Organic electronics is a field that has grown tremendously over the last four decades. In essence, it is the use of pi-conjugated organic materials in the production of electronic devices. Prototypes of organic polymer displays, and lighting panels have already been demonstrated and are predicted to reach market quite soon. The most attractive aspects of organic electronics are their light weight, flexibility and low-cost of production. With the rise in performance of newly synthesized organic semiconductors, the need for efficient charge injection into these materials becomes more and more critical to the overall performance of the organic devices. We have addressed this issue from various perspectives, utilizing a range of analytical techniques.

In this thesis we have studied charge injection contacts that make up one of the most important device components of organic devices. Contacts are used as charge injectors or acceptors into or from organic semiconductors. These contacts have to be stable and provide ohmic contact to the adjacent organic semiconductors. In addition, it is important to have fast, cheap and robust processing procedures. There are three main types of contacts: 1. Transparent metallic oxides such as indium-tin-oxide (ITO), 2. doped conducting polymers such as the commonly used poly(3,4-ethlyenedioxythiophene) doped with polystyrene sulfonic acid (PEDT:PSSH) and lastly 3. metallic electrodes. The first two have limitations on their conductivity and, specifically, ITO is becoming increasingly expensive due to diminishing source materials. On the other hand, the metallic electrodes have high conductivity. However, they have a fixed workfunction and do not generally allow easy modifications to make them compatible with a range of organic

semiconductors. The contacts in the most common organic devices are a combination of the three different types of contacts. In organic light-emitting diodes we have injection of holes from, for example, metallic oxides, into hole injecting layers on one side and injection of electrons from a metallic cathode at the opposite electrode. Field effect transistors have commonly metallic electrodes which inject either holes or electrons into the respective molecular orbital of the organic semiconductor. Similarly in solar cells, metallic oxides, hole extraction layers and a metallic cathode are used for charge extraction.

In this thesis, we focused on polymeric and modified metallic charge injection contacts. In Chapter 2 we discussed about the stability of polymeric charge injection contacts. Here, specifically, we discussed about a p-doped conducting polymer with superior electrical stability. A universal polymer instability phenomenon followed by a description of the unique polymer poly(3-methoxyethoxyethoxythiophene): poly(4-hydroxystyrene) (S-P3MEET:PHOST) which shows superior electrically stability. The new material, S-P3MEET:PSSH, is self doped and offers several advantages such as low acidity, and multi-solvent processibility. From this study it is evident that the suppression of the ionic conductivity through various mechanisms, here, specifically, by the use of a non-acidic host and depletion of protonic groups by serendipitious esterification leads to high electrical stability. Suppression of ionic conductivity is a new universal strategy to stabilize charge injecting polymers! In the future, it is important to put this strategy into use while synthesizing new conducting polymers. In addition, the role of stabilization played by PHOST should be further utilized by testing its compatibility and stabilization efficiency with other existing conducting polymers.

In Chapter 3, we demonstrated the importance of maintaining ohmic contact between adjacent multilayers to achieve efficient charge transport. I used a model system which was made by modifying PEDT:PSSH with a perfluorinated ionomer (PFI). We showed that this blend of PEDT:PSSH and the perfluorinated ionomer has high workfunction but that its device efficiency is limited by the presence of a non-ohmic layer. In summary, the ultrahigh workfunction of PEDT: PSSH: PFI blends, which persists in device structure, is due to the development of a dipolar surface layer due to surface segregation of PFI chains. The blended film PEDT:PSSH:PFI is determined to have energy level matching with deep IP polymers but doesn't improve charge injection due to a non-ohmic contact, as demonstrated by the absence of δ-hole charge carrier at the OSC interface as measured by electroabsorption spectroscopy (EA). Hence, workfunction matching alone is not sufficient to ensure ohmic injection into the adjacent OSC. Despite their higher tunneling barrier, double-carrier injection diodes show higher efficiency when using PFI blended HILs. Hence PFI blends still have a niche of application. However, to broaden their applicability, more work should be done in the future. A fundamental study of the role of surface energy and solubility can shade light into the reasons for PFI surface segregation and give clues as to how a high workfunction layer can be maintained without a substantial formation of a PFI surface layer. On the other hand, other insulating polymers which show a more limited surface segregation could be blended with PEDT:PSSH to investigate their applicability in producing high workfunction ohmic injectors.

In Chapter 4, we presented low and high work function copper surfaces as alternatives to currently popular electrodes. Copper attached to dimethyldithiocarbamate has low workfunction ~ 3.7 eV which is stable upon baking to 140 ^{0}C. High workfunction copper ~

5.4eV was prepared by a robust solution processed oxidation in hydrogen peroxide. To limit surface roughness caused by redeposition of Cu (II) oxide and hydroxide, pH control or solvent control with diethyl carbonate were introduced with successful results. The high workfunction copper demonstrated more efficient charge injection in diode configuration into the deep polymer poly(9,9'-dioctylfluorene-2,7-diyl-1,4-phenylene-N-(*p*-sec-butylphenyl)amino-1,4-phenylene) (TFB) compared to the control ITO/PEDT:PSSH. Organic field effect transistors were also built with the high-workfunction copper as source and drain electrodes demonstrating device properties comparable to the standard gold. On the other hand, the low-workfunction copper was used to build efficient electron injecting diodes into a DPP polymer. The results shown for both low-workfunction and high-workfunction modified copper are highly promising. In the future, it seems important to work further on the stability of the modified copper electrodes as stability of devices is the main current challenge. Stabilization through formation of self assembled monolayers via molecules which bind tightly with the copper underlayer should be investigated. Maintaining a thin layer of molecules is crucial to hinder the creation of a tunnelling barrier by these molecules.

The field of organic electronics has shown a rapid progress in the last decades. It is expected that the continued interest in this area will lead to the development of a new generation of materials and smart devices. All in all, with the ongoing development of robust materials and device architectures, the long sought dream for smart, cheap, flexible, easily processible organic devices seems to be on the horizon.

Appendix

A. Publications related to work done in this thesis

1. D. Belaineh, R. Q. Png, C. L. McGuiness, M. Mathai, V. Seshadri, P. K. H. Ho, "A High-Performance p-Doped Conducting Polymer With Remarkable Electrical Stability", Chemistry of Materials, 26, 4724–4730 (2014).
2. D. Belaineh, R. Q. Png, P. F. Dee, Y. M. Lee, B. N. N. Thi, N.S. Ridzuan, P. K.H. Ho," On the Nature and Injection Characteristics of Perfluorinated Ionomer-Modified Hole-Injection Layers", Advanced Functional Materials (2015).
3. D. Belaineh, R. Q. Png, P. K. H. Ho, "Robust high and low workfunction surface modified copper electrodes for superior charge injection in organic devices", manuscript under preparation.

B. Publications from work not described in this thesis

1. S. Pud, A. Kisner, M. Heggen, D. Belaineh, R. Temirov, U. Simon, A. Offenhäusser, Y. Mourzina, S. Vitusevich. "Features of Transport in Ultrathin Gold Nanowire Structures." Small, 9, no. 6 (2013): 846-852.
2. M. Marinkovich, D. Belaineh, V. Wagner, D. Knipp, "On the origin of contact resistances of organic thin film transistors." Advanced Materials, 24, no. 29 (2012): 4005-4009.

C. Conference presentations (presenting author underlined)

1. D. Belaineh, R. Q. Png, C. L. McGuiness, M. Mathai, V. Seshadri, P. K. H. Ho, "A High-Performance p-Doped Conducting Polymer With Superior Electrical Stability", ISOME 2014, Tokyo (Japan). Talk.
2. D. Belaineh, R. Q. Png, V. Seshadri, M. Mathai, P. K. H. Ho, "Suppression of Redox Instability in p-Doped Hole-Injection Layers", MRS Spring 2014, San Francisco (USA). Poster.
3. D. Belaineh, B. Gburek, V. Wagner, "Contact degradation of pentacene field-effect transistors", DPG, March 2009, Dresden (Germany). Poster.

4. D. Belaineh, B. Gburek, V. Zöllmer, V. Ruttkowski, M. Busse, V. Wagner, "Contact resistance effects of P3HT field-effect transistors produced by Maskless Mesoscale Material Deposition (M3D)", DPG, February 2008, Berlin (Germany). Poster.